

The
University
Of
Sheffield.

**Design, growth, fabrication and characterization of
white LEDs by monolithic on-chip epitaxial
integration on (11-22) semi-polar GaN**

Nicolas Poyiatzis

The University of Sheffield

Department of Electronic and Electrical Engineering

Supervisor: Professor Tao Wang

A Thesis Submitted for the Degree of Doctor of
Philosophy

(April) 2020

Abstract

Ultimate lighting sources for general illumination are monolithic on-chip white light emitting diodes (LEDs) containing multiple colour emissions, either red-green-blue or blue-yellow, but without involving any yellow phosphors. It is highly likely that current white LEDs fabricated by using a “blue LED+ yellow phosphors” approach will be eventually replaced by monolithic on-chip white LEDs. One of the direct routes for the fabrication of monolithic white LEDs is to utilize InGaN quantum wells (QWs) with different emission wavelengths as an active region, which will involve a number of fundamental issues, such as the design of an active region, carrier transport, etc. So far, these fundamental issues have not been understood. In this work, a systematic simulation study on these challenging issues has been carried out, achieving a full understanding of these issues and thus leading to the design of optimized white LED structures on (11-22) semi-polar substrates by taking the major advantages of semi-polar LEDs in comparison with their c-plane counterparts. Finally, the monolithic on-chip white LED epiwafer based on these designs have been successfully grown on our well-established (11-22) GaN templates with a step-change in crystal quality. Detailed device characterization has been performed on these LEDs, validating these approaches and designs.

The design of dual-colour (11-22) semi-polar LEDs aiming at white LEDs and their carrier transport issues have been systemically studied by using one-dimensional drift-diffusion simulations. Due to the much heavier effective mass of holes than that

of electrons and also the much larger activation energy of p-GaN than n-GaN, the distribution of injected carrier (mainly holes) is extremely uneven during LED operation. Furthermore, the residual polarization of semi-polar LEDs makes the case even more complicated. Based on a systematic study, carrier transport issues for (11-22) semi-polar white LEDs and their c-plane counterparts have been fully understood, demonstrating their major differences. In addition a novel structure utilizing an extra thin GaN spacer prior to the growth of blue InGaN quantum well, has been design to effectively improve hole transportation and a dual-colour emission LED has been achieved. A tri-chromatic emission has been subsequently designed by further optimizing two key factors, indium content in InGaN quantum wells and barrier thicknesses.

In order to validate our simulation results dual-color emission LEDs have been grown on our high quality (11-22) semi-polar GaN templates. Simulations have agreed very well with experimental results demonstrating that both the growth order of the yellow and blue InGaN quantum wells and the growth of a thin GaN spacer are of vital importance.

A different approach has been developed, leading to the growth and then the fabrication of monolithically integrated white light LEDs on (11-22) semi-polar GaN template. In this approach, an electrically injected semi-polar blue LED is firstly grown, followed by a yellow multiple quantum well structure as a down conversion layer. This forms a white LED.

For the first time, a systematic and comprehensive study on optical polarization properties has been conducted on (11-22) semi-polar LEDs with a wide spectral

region from blue to yellow as a function of indium concentration and injection current. Fundamental understanding of the polarization properties and the emission mechanisms of (11-22) semi-polar LEDs has been achieved. Detailed polarization dependent electroluminescence measurements have demonstrated that both indium content and current injection play crucial roles in the optical polarization properties of (11-22) semi-polar LEDs.

Acknowledgements

I would to express my gratitude to many people who have helped me during my journey of perusing a Ph.D degree. First, of all I would like to thank Prof. Tao Wang, who gave me the opportunity to pursue a Ph.D in the area of III-nitrides optoelectronics. Without his guidance, support and encouragement through all of these years, nothing would be possible. I am also very grateful to my second supervisor Dr. Rick Smith with whom I spent many hours discussing my projects. I would like to thank Dr. Jie Bai for training me in all the required equipment for LED fabrication and for her useful advices and extensive support throughout my projects.

Additionally I would like to thank a former member of our group and a really good friend, Dr. Modestos Athanasiou for his valuable advices and his enormous support through all of the years of my Ph.D journey. Furthermore, I would like to thank the members of our group and also former colleagues: Mr. Xuanming Zhao, Mr. Shuoheng Shen, Mr. Peter Fletcher, Mr. Peng Feng, Mr Ye Tian, Mr Jack Hagggar, Mr. Volkan Esendag, Mr. Guillem Martinez de Arriba, Dr. Zohaib Ahmed, Dr. Suneal Ghataora, Dr. Ling Jiu, Dr Yuefei Cai, Dr. Yun Zhang, Dr. Xiang Yu and Dr. Yipin Gong for their help and valuable discussions. I am also grateful to the technical staff Mr. Paul Haines, Mr, Jonathan Milner and Mr. Stephen Atkin for their extensive technical support and for maintaining the equipment in the cleanroom.

I would like to give the greatest gratitude to my family, my father Christos, my mother Ofelia and my sister Loukia. Without their unconditional love and support nothing would be possible.

I want to dedicate the next paragraph to my grandparents Nicos and Loukia to whom I owe everything. 'Pappou' (grandfather) you are my hero, the person who I admire the most in the world. You taught me how to love, respect and the real meaning of the word family. I am very proud that you are my grandfather. 'Giagia' (grandmother) you are my superhero. I have not yet figured it out how you manage to do so many activities and tasks without getting tired. You also cook the greatest food in the world despite the fact that you are not professional cook. Moreover, i still remember the entrance day at my primary school where you were holding my hand and I would kindly ask you to hold my hand again at my graduation.

Last but not least, I would like to thank my girlfriend Ioanna for her love, support and her enormous patience throughout my Ph.D journey.

List of Publications

Journal Publications

1. **N. Poyiatzis**, J Bai, R. M. Smith, M. Athanasiou, S Ghataora and T. Wang, “*Optical polarization properties of (11-22) semi-polar InGaN LEDs with a wide spectral range*” *Sci. Rep. Sci. Rep.* 10, 7191 (2020).
2. **N. Poyiatzis**, M. Athanasiou, J Bai, Y. Gong and T. Wang, “*Monolithically integrated white light LEDs on (11-22) semi-polar GaN templates*”, *Sci. Rep.* 9, 1383 (2019).
3. J. Bai, L. Jiu, **N. Poyiatzis**, P. Fletcher, Y. Gong and T. Wang, “*Optical and polarization properties of nonpolar InGaN-based light-emitting diodes grown on micro-rod templates*”, *Sci. Rep.* 9, 9770 (2019).
4. M. Athanasiou, P. Papagiorgis, A. Manoli, C. Bernasconi, **N. Poyiatzis**, P. M. Coulon, P. Shields, M. I. Bodnarchuk, M. V. Kovalenko, T. Wang and G. Itskos, “*InGaN Nanohole Arrays Coated by Lead Halide Perovskite Nanocrystals for Solid-State Lighting*”, *ACS Appl. Nano Mater.* 3, 2167–2175 (2020).
5. S. Ghataora, R. M. Smith, **N. Poyiatzis**, M. Athanasiou, and T. Wang, “*Sub-Micron Direct-Write Photolithography using Confocal Photoluminescence Microscopy System in Fabrication of III-Nitride Micro-Pillar Light-Emitting Diode Device*”, (In preparation).

Conference Contributions

1. M. Athanasiou, P. Papagiorgis, A. Manoli, C. Bernasconi, **N.Poyiatzis**, P. M. Coulon, P. Shields, M. I. Bodnarchuk, M. V. Kovalenko, T. Wang and G. Itskos, *"III-Nitride/Perovskite Nanocrystal Structures for Efficient Light Down-conversion via Förster Resonant Energy Transfer"*, NanoGe Conference, Berlin, Germany, November 2019.
2. L. Jiu, J. Bai, **N. Poyiatzis**, P. Fletcher, and T. Wang, *"Nonpolar (11-20) InGaN/GaN light-emitting diodes overgrown on a micro-rod Template"*, Semiconductor and Integrated Opto-Electronics, Cardiff, UK, April 2019.
3. L. Jiu, J. Bai, **N. Poyiatzis**, P. Fletcher, Y. Gong, and T. Wang, *"Nonpolar a-plane (11-20) InGaN-based light-emitting diodes grown on micro-rod templates"*, UK Nitrides Consortium Winter, Glasgow, UK, January 2019.
4. **N.Poyiatzis**, J. Bai, M. Athanasiou, L. Jiu, Y. Gong and T. Wang, *"Phosphor-free InGaN white light emitting diodes overgrown on semi-polar GaN templates"*, 12th International Conference on Nitride semiconductors (ICNS-12), Strasburg, France, July 2017.
5. **N. Poyiatzis**, J Bai, M. Athanasiou, L. Jiu, Y. Gong and T. Wang, *'Monolithically integrated white light LEDs on (11-22) semi-polar GaN'*, UK Semiconductors, Sheffield, July 2017.

Table of Contents

Abstract	i
Acknowledgements	iv
List of Publications	vi
Journal Publications	vi
Conference Contributions	vii
List of Figures	xii
List of Tables	xvii
CHAPTER 1	1
Introduction	1
1.1 The Energy Crisis	1
1.2 Light Sources	3
1.3 History and Development of III-nitrides LEDs.....	4
1.4 Challenges in III-nitrides	8
1.4.1 Substrates	8
1.4.2 Quantum Confined Stark Effect (QCSE)	9
1.4.3 Green/Yellow Gap	11
1.4.4 Efficiency Droop.....	12
1.5 White light LEDs.....	13
1.6 Semi-polar and non-polar planes.....	13
1.7 Thesis outline	14
References	17
CHAPTER 2	23
Background	23
2.1 Semiconductors	23
2.2 Band Structure.....	25
2.2.1 Absorption	26

2.2.2 Luminescence	26
2.3 Recombination Mechanisms	27
2.4 p-n Junction	30
2.5 Light Emitting Diode	31
2.5.1 Low dimensional structures	32
2.6 III-nitride Semiconductors	33
2.6.1 Crystal Structure of III-nitride	34
2.6.2 Chemical and Electrical Properties of III-nitrides.....	35
2.6.3 Spontaneous and Piezoelectric Polarizations.....	37
2.7 Semi-polar and non-polar III nitrides	38
2.7.1 Reduced polarization piezoelectric fields	39
2.7.2 Indium incorporation	40
2.7.3 Growth of (11-22) semipolar GaN.....	41
References.....	44
CHAPTER 3.....	47
Experimental techniques	47
3.1 Introduction	47
3.2 Fabrication Technique	47
3.2.1 Photolithography.....	47
3.2.2 Dry etching techniques.....	49
3.2.3 Thin Film Deposition	52
3.2.4 Rapid thermal annealing (RTA)	54
3.4 LED fabrication procedure	55
3.5 Optical and Electrical characterization	59
3.5.1 Photoluminescence	59
3.5.2 Electroluminescence	60
References.....	62
Chapter 4.....	64
Carrier transport in multi-colour (11-22) semi-polar LEDs.....	64
4.1 Introduction	65
4.2 Methods	67

4.3 Dual color LED on (11-22) semipolar and c-plane orientation	71
4.4 GaN spacer and design of new structure.....	74
4.5 Growth order of dual-color (11-22) semipolar LEDs.....	76
4.6 Design of tri-chromatic (11-22) semipolar LED.....	78
4.7 Summary.....	85
References.....	87
Chapter 5.....	89
Fabrication of monolithically integrated white light LEDs on (11-22) semi-polar GaN templates.....	89
5.1 Introduction	90
5.2 Monolithically integrated white light LED on (11-22) semipolar GaN template for white light emission by band engineering	94
5.3 Methods	96
5.4 Results and discussion	97
5.4.1 Photoluminescence measurements.....	97
5.4.2 Electroluminescence measurements.....	98
5.5 Monolithically integrated white light LED on (11-22) semipolar GaN template for white light emission using down-converter approach	102
5.6 Methods.....	103
5.7 Results and discussion:	105
5.7.1 P-type activation.....	105
5.7.2 Photoluminescence measurements	106
5.7.3 Electroluminescence measurements.....	106
5.8 Summary.....	108
References.....	110
Chapter 6.....	113
Optical polarization properties of (11-22) semi-polar InGaN LEDs with a wide spectral range	113
6.1 Introduction	114
6.2 Methods	116
6.2.1 Epitaxial growth.....	116

6.2.2 Device Fabrication.....	118
6.3 Results and Discussion.....	119
6.4 Summary.....	127
References.....	129
Chapter 7.....	132
Conclusions and future work.....	132
7.1 Summary of results.....	132
7.1.1 Carrier transport in multi-colour (11-22) semi-polar LEDs.....	132
7.1.2 Fabrication of monolithically integrated white light LEDs on (11-22) semi-polar GaN templates.....	133
7.1.3 Optical polarization properties of (11-22) semi-polar InGaN LEDs with a wide spectral range.....	133
7.2 Future work.....	134
References.....	136

List of Figures

Figure 1.1 Global surface Temperature variations over the years ⁶	2
Figure 1.2 Bandgap of semiconductors as a function of lattice constant ¹⁸	5
Figure 1.3 Band diagram of an InGaN/GaN quantum well grown on (a) without induced polarization fields and (b) with the presence of induced polarization fields.	10
Figure 1.4 External quantum efficiency of LEDS at room temperature. $V(\lambda)$ refers to human eye response ⁴¹	11
Figure 1.5 External quantum efficiency of blue and green InGaN based LEDS ⁴³	12
Figure 2.1 Schematic illustration of band-structure of conductor, semiconductor and insulator	23
Figure 2.2 Schematics of a) direct and b) indirect band-structure	25
Figure 2.3 Schematic illustration of recombination mechanisms	27
Figure 2.4 p-n junction band-structure under 0V bias	30
Figure 2.5 Schematic of LED structure	31
Figure 2.6 Schematic of quantum structures as a function of dimension	33
Figure 2.7 Schematic of atom configuration in GaN wurtzite structure	35
Figure 2.8 Schematic of commonly used hexagonal planes	39

Figure 2.9 Piezoelectric polarization and electron – hole wavefunction overlap as a function of crystal angle with respect to c-plane orientation in a 3 nm $\text{In}_{0.25}\text{Ga}_{0.75}\text{N}$ quantum well ¹⁵	40
Figure 2.10 Schematic of patterned r-plane sapphire for growing semi-polar (11-22) GaN^{20}	42
Figure 2.11 Schematic of the fabrication processes of micro-rods template	43
Figure 3.1 Karl Suss MJB3 mask aligner	49
Figure 3.2 a) RIE system used in this work, b) Schematic of RIE system and c) Optimized conditions for material etching	50
Figure 3.3 a) ICP system used in this work, b) schematic of ICP system and c) recipe for GaN etching.....	51
Figure 3.4 a) Edwards E306A Thermal evaporator and b) schematic illustration.....	52
Figure 3.5 a) Plasma-Therm 790 PECVD system and b) schematic illustration	54
Figure 3.6 Jipelec thermal annealing system	55
Figure 3.7 Schematic illustration of LED fabrication	56
Figure 3.8 Schematic illustration of current path a) without current spreading layer and b) with current spreading layer.	58
Figure 3.9 Schematic diagram of photoluminescence system	60
Figure 3.11: Schematic diagram of electroluminescence system.....	61
Figure 4.1 Flow chart diagram of the simulation procedures.....	69

Figure 4.2 Schematics of LED structure in a) c-plane and b) (11-22) orientation.....	71
Figure 4.3 Simulated band diagrams of (a) c-plane LED and (b) (11-22) LED; and their corresponding carrier concentration in the InGaN quantum well region of (c) c-plane LED at 180 A/cm^2 , 9.6 V and (d) (11-22) LED at 180 A/cm^2 9.3V, (e) IQE of c-plane LED and (11-22) LED f) simulated EL intensity of c-plane and (11-22) LEDs.....	73
Figure 4.4 Calculated distribution of hole concentration across the InGaN quantum well region as a function of GaN spacer thickness; (b) Simulated electro-luminescence (EL) spectra as a function of GaN spacer thickness	75
Figure 4.5 Schematics of Sample A and Sample B	76
Figure 4.6 Simulated band diagrams for (a) Sample A and (b) Sample B, (c) simulated hole concentration in the InGaN quantum well region of Sample A and Sample B (d) Simulated EL intensities of Sample A and Sample B at 180 A/cm^2 , 9.1 V and 180 A/cm^2 9.5 V respectively	77
Figure 4.7 Simulated band diagrams for (a) Sample B and (b) Sample C, (c) simulated hole concentration in the InGaN quantum well region of Sample B and Sample C (d) Simulated EL intensities of Sample B and Sample C at 180 A/cm^2 , 9.5 V and 180 A/cm^2 9.4 V respectively	80
Figure 4.8 Simulated band diagrams for (a) Sample C and (b) Sample D, (c) simulated hole concentration in the InGaN quantum well region of Sample C and Sample D (d) Simulated EL intensities of Sample C and Sample D at 180 A/cm^2 , 9.4V and 180 A/cm^2 , 9.8V respectively.....	81
Figure 4.9 Band diagram as a function of the barrier thicknesses	82

Figure 4.10 Calculated distribution of hole concentration across the InGaN quantum well region as a function of barrier thickness located between the long wavelength QWs and (b) magnified image of hole concentration of the 1 st grown QW	83
Figure 4.11 Simulated band diagrams for (a) Sample E and (b) Sample F, (c) simulated hole concentration in the InGaN quantum well region of Sample E and Sample F, (d) Simulated EL intensities of Sample E and Sample F at 180 A/cm ² ,9.3V and 180 A/cm ² 9.7V respectively.....	84
Figure 4.12 (a) CIE chromaticity coordinates for Sample E and Sample F and (b) schematic illustration of Sample F	85
Figure 5.1 Schematics of Sample A and Sample B	95
Figure 5.2 Photoluminescence spectra of the as grown Sample A and Sample B	97
Figure 5.3 EL spectra measured at different injection currents for (a) Sample A and (b) Sample B. The insets show the IV plots of Sample A and Sample B	98
Figure 5.4 Simulated and experimental EL for (a) Sample A and (b) Sample B at 200mA.....	99
Figure 5.5 EL images at injection currents from 5mA to 200mA of (a) Sample A and (b) Sample B and (c) CIE x,y coordinates for Sample B as a function of current	101
Figure 5.6 Schematic illustration of fabricating monolithically integrated LED with micro-rods array	104
Figure 5. 7 I-V characteristics of the monolithically white light LED	105
Figure 5.8 PL spectra of the as grown sample	106

Figure 5.9 EL spectra under low and high injection currents the inset shows the spectra in log-plot..... 107

Figure 6.1 Typical cross-sectional TEM image of our (11-22) LED overgrown on a micro-rod arrayed template (a) and Typical plane-view TEM image of our (11-22) LED structure, showing that the dislocation density is $2.0 \times 10^8 / \text{cm}^2$ ^{6,7,8} 117

Figure 6.2 Schematic of semi-polar (11-22) InGaN LEDs..... 118

Figure 6.3 Schematics of (a) semi-polar (11-22) GaN crystal plane and (b) band diagram before and after polarization switching. 119

Figure 6.4 Polarized EL spectra measured at 20 mA injection current for the semi-polar (11-22) LEDs with increasing indium content and peak emission wavelength. In each case, the EL spectrum labeled in red was measured at a polarizer angle of 0° corresponding to the electric field aligned along [1-100], while the EL spectrum in blue was measured at a polarizer angle of 90° corresponding to the electric field aligned along [-1-123]. 122

Figure 6.5 (a) Polarization degree as a function of peak emission wavelength; and (b) Energy separation ΔE of the two polarized emissions as a function of peak emission wavelength. Solid lines are a guide to the eye..... 123

Figure 6.6 (a) Polarization degree as a function of injection current; and (b) Energy separation ΔE as a function of injection current of each of the semi-polar LEDs..... 125

Figure 6.7 Change of polarization as a function of emission wavelength 126

List of Tables

Table 2.1 Lattice constants of GaN, AlN and InN ⁸	35
Table 2.2 Materials parameters of InN, GaN and AlN ^{9,10,11}	36
Table 2.3 Electrical and thermal properties of InP, GaAs and GaN ^{12,13,14,15}	36
Table 4.1 Basic GaN materials parameters in c-plane ¹¹	70
Table 4.2 Effective electron and hole masses in binary nitrides at 300K with m_{\perp} and m_{\parallel} are the in-plane and normal to the growth direction effective masses ¹¹	70

CHAPTER 1

Introduction

This chapter presents the motivation and objectives of the project and a brief introduction on the history of the development of III-nitride semiconductors. The current challenges have been highlighted along with the major advantages, benefits and potential of III-nitride based optoelectronic devices.

1.1 The Energy Crisis

Climate change has prompted governments, scientists and many organizations such as UNESCO to raise global awareness for mitigating or even preventing any potential risk of an upcoming natural calamity¹. The greenhouse effect, has inevitably led to many environmental changes such as an increase in global mean surface temperature, reduced sea ice and the rise of the sea levels. A report from Intergovernmental Panel on Climate Change (IPCC) stated that anthropogenic carbon emissions have caused an approximate 1°C increase in global temperature since the pre-industrial era, while it has been predicted that the global temperature would potentially rise by as high as 1.5 °C to 2°C between the years 2030 and 2052 if substantial actions would not be taken to reduce the current rate in global temperature increase². Such facts require collective global action in order to restrict the global temperature rise by 1.5°C, as agreed under the Paris agreement of 2018³.

Therefore, multiple-national efforts need to significantly reduce carbon emission.

Figure 1.1 illustrates the global temperature variation over the years.

One of the largest sources of greenhouse emissions responsible for 42.5% of the global carbon emission comes from electricity generation⁴. In 2018 the global electricity consumption was more than 23000 TWh whilst the total global energy-related CO₂ emissions have reached an astonishing value of 33.1Gt⁵. It is therefore of paramount importance to reduce electricity consumption and correspondingly reduce carbon emission by means of developing new technologies which will lead to more efficient energy consumption and sustainable energy sources.

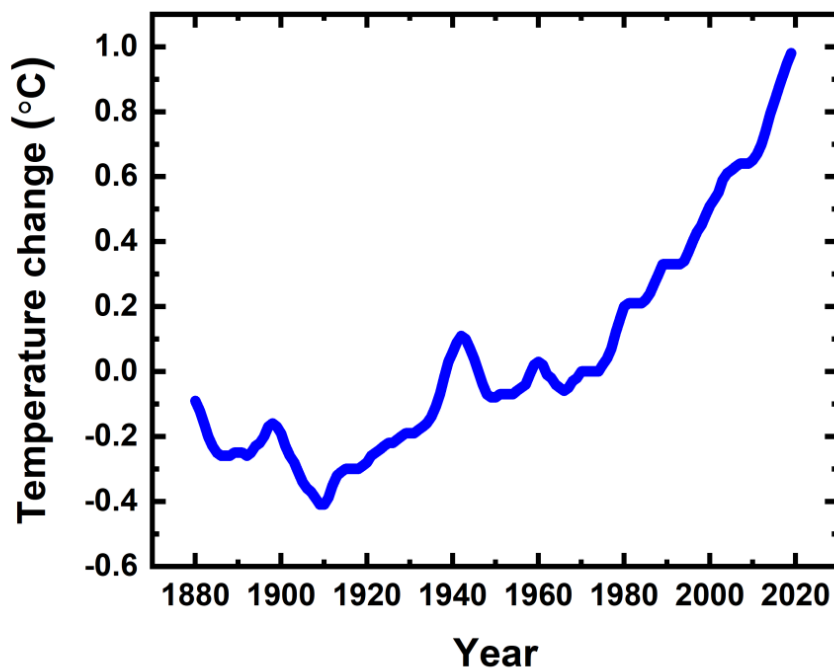


Figure 1.1 Global surface Temperature variations over the years⁶

1.2 Light Sources

Since the invention of the incandescent lamp by Thomas Edison in 1879, artificial light sources are of vital importance for many applications in our daily life. Lighting consumes around 20% of the global electrical energy consumption, with a very important contribution in electricity consumption^{7,8}. Inefficient lighting sources, such as incandescent lamps with a typical efficiency of 16 lm/W waste a huge amount of electricity⁹. The development of fluorescent tubes in the late 19th and early 20th centuries led to enhanced efficacies, which is in the range of ~70lm/W. However, fluorescent tubes contain mercury which is toxic and non-environmental friendly, as mercury vapor is required for discharge. Consequently, fluorescent lamps along with incandescent lamps face a gradual phase out under legislations in a large number of countries¹⁰.

The last two decades have seen great achievements in developing solid state lighting for general illumination which is primarily based on III-nitride semiconductor light-emitting diodes (LEDs). Unlike fluorescent lamps, semiconductors LEDs are environmental friendly since they do not contain any toxic elements. The main approach to the fabrication of white light LED is to combine a blue LED with down conversion yellow phosphors. So far the highest efficacy white light LEDs commercially available exhibit more than 200 lm/W luminous efficacy¹¹. However, it has been predicted that the theoretical limit of the maximum possible luminous efficacy is 370 lm/W¹² depending on spectral distributions of components needed to synthesize white light emission and color rendering index (CRI). For such high luminous efficacies, white light LEDs have to exhibit high quantum efficiencies

including Internal Quantum Efficiency (IQE), External Quantum Efficiency (EQE) and wall plug efficiency. Therefore, there exists a plenty of scopes for further improvement in efficiency.

In addition to energy savings and high efficiencies, LEDs can be utilized in a wide range of areas such as traffic lights, automotive lighting, backlighting for liquid crystal displays (LCDs). LEDs also exhibit high modulation bandwidth in comparison with incandescent or fluorescent lamps which make them suitable for visible light communication (VLC)¹¹.

1.3 History and Development of III-nitrides LEDs

The very first LED emitting in the visible region was demonstrated in 1962, where a heterostructured p-n diode based on GaAsP emitting in the red region was used by N. Holonyak and S.F. Bevacqua¹³. Since then considerable efforts have been devoted to the development of devices emitting in the short wavelength and visible spectrum. One method employed to achieve shorter wavelengths was to increase the mole fraction of phosphorous in a GaAs_{1-x}P_x system which exhibited poor efficiency and could not cover a wide range of visible spectral region. The fundamental issue is due to the indirect band structure of GaAs_{1-x}P_x if $x=0.49$ ¹⁴.

Green and yellow emissions were realized in 1968 and 1971^{15,16}, respectively by utilizing nitrogen dopants in GaP: N and GaAsP: N which act as radiative recombination centers, although GaP exhibits an indirect band structure.

SiC with an indirect bandgap structure was first used for the fabrication of blue LEDs, showing a very low external quantum efficiency of 0.03% at 470nm center wavelength¹⁷.

III-nitrides materials and optoelectronics have achieved major developments over the last two decades. Due to the tunable and wide bandgap of III-nitrides all with direct band structures which cover a wide spectral range from deep ultraviolet through the whole visible spectrum to the infrared, III-nitrides have found a wide range of applications and especially are ideal candidates for the fabrication of high efficiency white light LED. Figure 1.2 shows that the band-gaps of III-nitrides cover a wide range from 0.7 eV for InN through 3.4 eV for GaN to 6.2 eV for AlN.

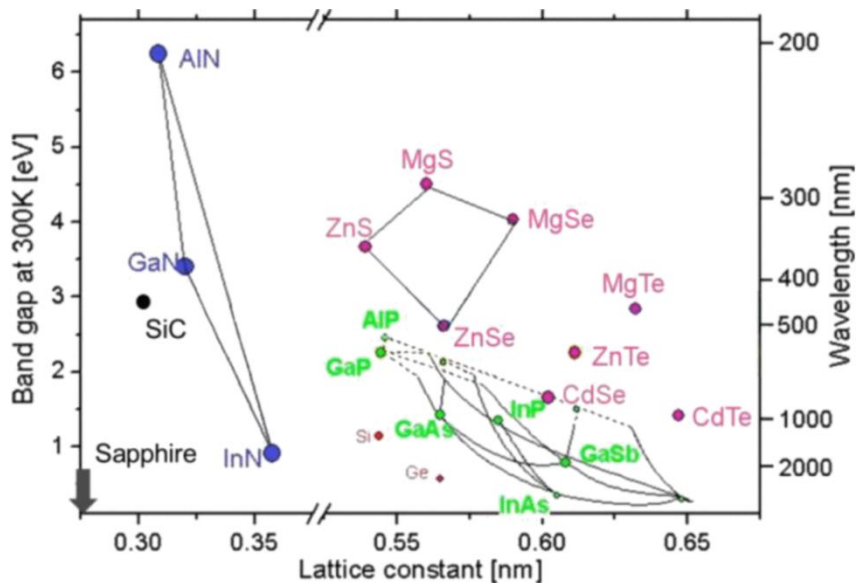


Figure 1.2 Bandgap of semiconductors as a function of lattice constant¹⁸

Single crystalline GaN films grown on sapphire was reported by Maruska et al. in 1969 using a hydride vapour phase epitaxy (HVPE) technique. The direct band-gap of GaN

which is ~ 3.4 eV was then determined by optical absorption measurements¹⁹. The realization of III-nitrides as a direct band-gap material has prompted attempts to develop optoelectronics devices by utilizing these materials. In 1971 Pankove et al demonstrated the first electroluminescence (EL) measurement on a metal/insulator/semiconductor (MIS) LED structure grown by HVPE. The LED exhibited very low performance due to the lack of p-doped material²⁰. Subsequently, a MIS LED with an Mg-doped insulating layer exhibiting a violet emission (425nm) was reported by H. Maruska et al in 1972²¹.

The utilization of metal organic chemical vapour deposition (MOCVD) for growing single-crystal GaN films was first reported in 1971 by H. M Manasevit, which was a crucial step for growing multi-layer device structures as a result of its major advantages in controlling epitaxial layer deposition on an atomic level²². However, the crystal quality of GaN films was far from satisfactory for a long time, until the major breakthrough was achieved in 1986 when a so-called two-step growth method which has been widely used was introduced into MOCVD growth by Amano and Akasaki. This two-step growth means a thin film of AlN nucleation layer grown on sapphire at a low temperature, such as 450-600°C, followed by growing a thick GaN layer at a high temperature (typically above 1000°C) prior to the growth of any further device structures^{23,24}. The AlN nucleation is used to mitigate the large strain between sapphire and GaN caused by their large lattice mismatch of 16%. By using the two-step method, the crystal quality of GaN on sapphire is significantly improved.

P-type GaN film was still unresolved by that time, making it impossible to realise p-n junction LEDs. Magnesium (Mg) was considered to be a good candidate for p-type dopant of GaN films. Nevertheless, the high resistivity and the insurmountable

passivation of Mg-dopants were major obstacles. During MOVPE p-GaN growth the inevitable incorporation of hydrogen leads to the formation of Mg-H complexes. This was the fundamental reason preventing the as-grown magnesium-doped GaN to act as a p-type GaN. Therefore, an activation procedure is necessary to dissociate the hydrogen from the material and break the Mg-H bonds in order to allow the magnesium to act as a p-type dopant.

P-GaN was obtained by Amano and Akasaki in 1989 by introducing a low-energy electron beam irradiation (LEEBI) activation process on Mg-doped GaN, where a remarkable reduction in resistivity from $10^8 \Omega\text{cm}$ to $35 \Omega\text{cm}$ and a hole concentration on the order of $10^{16}/\text{cm}^3$ were obtained²⁵. Consequently, the very first GaN p-n junction LED in the UV region was achieved. Shuji Nakamura invented a different p-type activation approach in 1992 by introducing a post-growth annealing of Mg doped GaN films at a high temperature under nitrogen ambient, significantly simplifying the activation process and thus opening an effective approach for mass production. Furthermore, the post annealing approach also led to the further reduction of resistivity down to a $2 \Omega \text{ cm}$ level and to further increase of free holes carrier concentration by an order of magnitude to a $10^{17}/\text{cm}^3$ level²⁶. In 1994, Shuji Nakamura et al. reported the first double heterostructure electrically injected LEDs based on InGaN/AlGaN QWs emitting in the blue region with a luminous intensity of 1.2cd^{27} . The outstanding contributions from Isamu Akasaki, Hiroshi Amano and Shiji Nakamura in developing GaN-Based LEDs have been recognised by awarding them the Nobel Prize in Physics in 2014²⁸.

1.4 Challenges in III-nitrides

III-nitride semiconductors have seen major advancements in the last two decades. Nevertheless, the success of III-nitrides optoelectronic devices is still limited to GaN grown on c-plane substrates, i.e., the polar orientation which poses a number of fundamental issues which need to be overcome in order to further improve optical performance of III-nitride based optoelectronic devices.

1.4.1 Substrates

One of the greatest challenges in epitaxial growth of GaN is due to the lack of native and affordable substrates. Free standing GaN are typically obtained by means of a hydride vapour phase epitaxy technique and then a substrate lift-off process, where GaN with a typical thickness of up to 300 μ m can be grown on sapphire by using gallium chloride (GaCl) and ammonia (NH₃)²⁹. Then the sapphire substrate can be removed by using a laser-lift off technique or other techniques^{30,31,32}. Clearly, such a method is not cost-effective and thus free-standing GaN substrates are normally used for special purpose.

Owing to the lack of native substrates, III-nitrides are mainly grown on foreign substrates, typically on sapphire, silicon and sometimes on silicon carbide, which is very expensive. The utilization of foreign substrates poses a number of major challenges due to their lattice mismatch and different thermal expansion coefficient, inevitably leading to not only a high density of defects but also other issues such as wafer bowing and cracking.

SiC/GaN exhibits much less lattice mismatch than either Sapphire/GaN or Silicon/GaN³³. However, SiC substrates are very expensive, making them less favourable for mass production.

Silicon substrates which have a low cost and a large size (up to 18 inch) availability are also commonly used in integrated circuits. However, the large lattice mismatch between GaN and Si (17%) and the large difference of 54% in thermal expansion coefficient lead to a high density of defects and severe bowing and cracking issues. Hence, despite of the large lattice mismatch of 16% between sapphire and GaN, sapphire is widely used as a foreign substrate for GaN growth due to its thermal stability and less thermal expansion coefficient mismatch compared with other substrates.

1.4.2 Quantum Confined Stark Effect (QCSE)

GaN in wurtzite structure intrinsically exhibits spontaneous polarizations along the c-axis due to its low symmetry³⁴. As a result, any III-nitride heterostructure suffer from strain due to the different lattice constants of GaN, InN and AlN which lead to the formation of piezoelectric fields. Generally speaking, for the emitters in the visible spectrum, where InGaN/GaN quantum well structures are used as an emitting region, the induced piezoelectric fields result from compressive strain across the active region consisting of InGaN quantum wells and GaN barriers. The presence of an electric field causes the inevitable spatial separation of electron and hole wavefunctions leading to a reduction in optical-transition probability and an increase in radiative recombination lifetimes. This results in a decrease in quantum efficiencies. This is termed as Quantum Confined Stark Effect (QCSE). For longer wavelengths,

where higher indium content is required, the strain generates even stronger piezoelectric fields, further enhancing QCSE and a further reduction in the overlap of electron-hole wavefunctions and longer radiative recombination lifetimes are observed. Furthermore, the band-bending caused by polarization fields lowers the effective band-gap, leading to a red shift in emission wavelength. Figure 1.3 illustrates the band diagram of an InGaN/GaN quantum well without any induced polarization fields and an InGaN/GaN quantum well and with the effect of polarization-fields. In the latter case, under forward bias, a blue shift in peak wavelength will occur as a result from the injected carriers which screen part of the polarization field and flattens the bands.^{35,36} One of the most promising solutions to overcoming or minimizing QCSE is the growth of III-nitrides along either a semi-polar or non-polar orientation where piezoelectric field can be suppressed or eliminated completely^{37,38,39,40}. Figure 1.3 depicts a schematic illustration of the band diagram of an InGaN/GaN quantum well structure under the influence of QCSE.

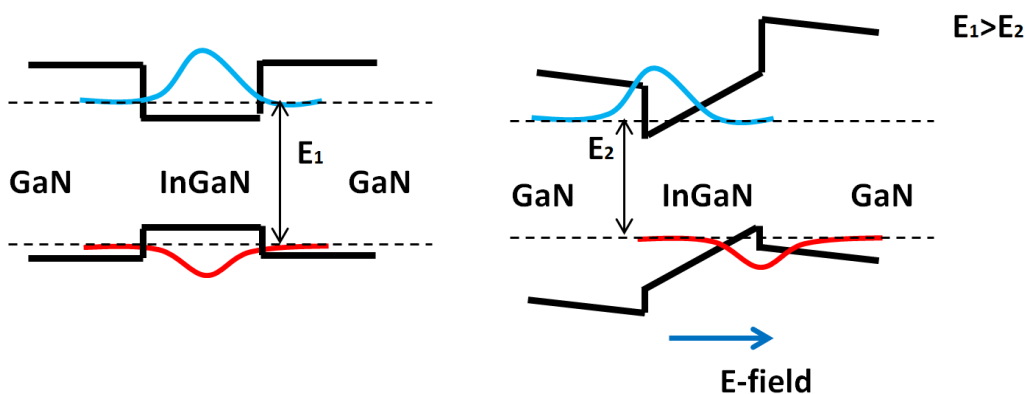


Figure 1.3 Band diagram of an InGaN/GaN quantum well grown on (a) without induced polarization fields and (b) with the presence of induced polarization fields

1.4.3 Green/Yellow Gap

QCSE also leads to a great challenge in obtaining efficient emitters in the green-yellow spectrum. As mentioned above, the increment of indium mole fraction in InGaN is crucial for obtaining long emission wavelength such as green and yellow, significantly enhancing QCSE and thus posing a great challenge on obtaining high efficiencies. On the other hand, traditionally yellow emission can be achieved by incorporating nitrogen into GaP. However, the main issue for this system is due to the fact the GaP exhibits indirect band-gap leading to low efficiencies. Therefore, the challenges lead to the formation of the so-called green/yellow gap, which is illustrated in Figure 1.4, demonstrating the lowest efficiency in the green-yellow region across the whole UV-visible spectrum.

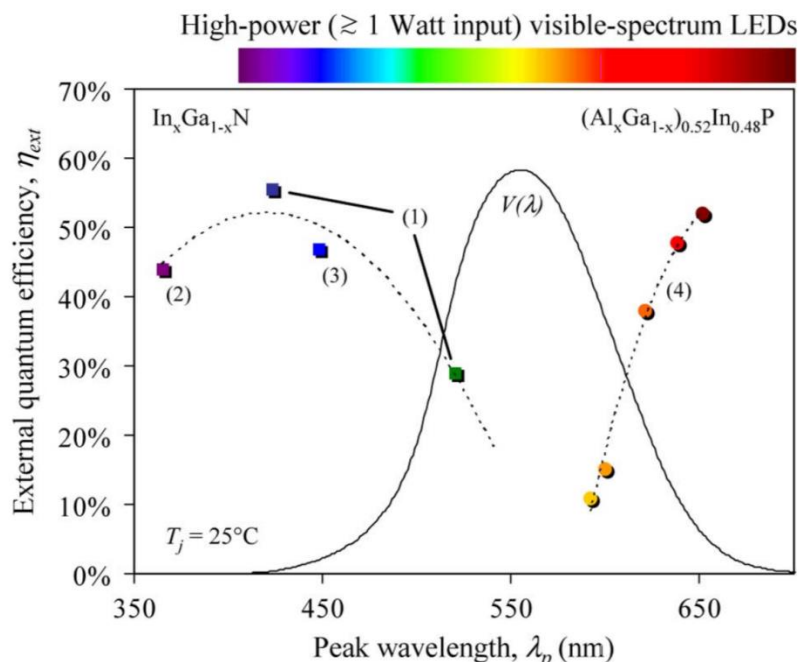


Figure 1.4 External quantum efficiency of LEDs at room temperature. $V(\lambda)$ refers to human eye response⁴¹

1.4.4 Efficiency Droop

Efficiency droop is another major issue for utilizing III-nitride LEDs for solid state lighting, meaning that the efficiency of an LED is firstly increasing with low current density, and then start decreasing with higher current density^{42,43}. Figure 1.5 illustrates the efficiency droop of commercial blue and green LEDs, showing the 'droop' starts at a low injection current. A number of models have been suggested, such as Auger recombination, defects, leakage current, polarization, etc. Auger recombination is the process in which the released energy from carrier recombination is absorbed by a third carrier which then is excited to a higher energy level instead of being released as a photon⁴². This results in non-radiative recombination of carriers at higher carrier densities (i.e., at high injection current densities) which inevitably leads to a decrease in quantum efficiency. However, so far the formation mechanisms of efficiency droop are still debatable.

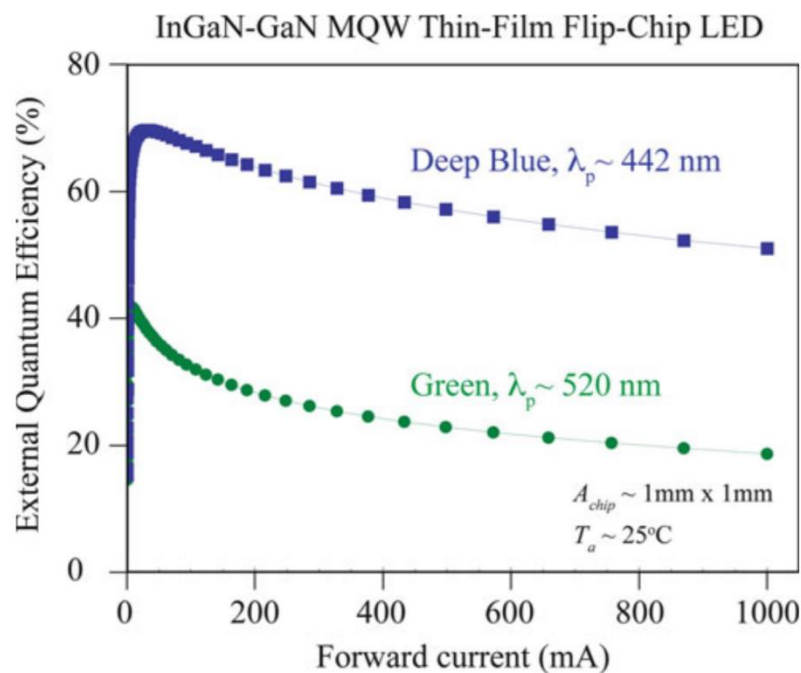


Figure 1.5 External quantum efficiency of blue and green InGaN based LEDs⁴³

1.5 White light LEDs

White light LEDs are the ideal candidates to replace incandescent lamps and fluorescent tubes due to low power consumption and long lifetime as mentioned above. Current white LEDs are fabricated by mainly using a down-conversion method where part of a blue GaN based LED is utilized to optically pumped yellow phosphors. However, phosphor-converted white LEDs have distinct disadvantages, such as non-radiative internal losses, optical loss due to light backscattering, heating-related effects and long-term reliability of phosphors⁴⁴.

The distinct drawbacks of efficiency and lifetime of phosphor based LEDs have prompted many groups to devote considerable effort to developing alternative approaches to the fabrication of white light LEDs, such as red-green-blue white LEDs or blue-yellow LEDs in a single chip. Phosphor based white light LED with 200lm/W are commercially available but still far from the theoretical limit of 370lm/W. However, the optical efficiency of InGaN LEDs on c-plane substrates decreases with increasing indium as a result of QCSE. This becomes more severe when the emission moves toward longer wavelengths such as green or yellow spectral region. Consequently, it is very difficult to obtain white light LEDs with high efficiency and high colour rendering index.

1.6 Semi-polar and non-polar planes

In order to overcome the polarization induced QCSE, the growth of III-nitrides along either a semipolar or a nonpolar direction, where the electric field is partially or totally reduced, is one of the most promising approaches. Among all the semi-polar orientations, the (11-22) semi-polar surface significantly favors indium incorporation

into GaN⁴⁵, which is essential for growing of longer wavelength InGaN/GaN quantum wells. Very recently, long wavelength emitters have gained increasing focus due to not only solid-state lighting but also optogenetic applications. In the latter, III-nitride visible emitters with a longer emission wavelength play an important role in manipulating neurons, which will assist in the understanding of neural circuit behaviors and responses under light stimulating conditions. This important work will help in finding a solution to curing Parkinson's disease, mood disorders and many more^{46,47}.

1.7 Thesis outline

The research presented in this PhD thesis initially demonstrates a systematic simulation study in order to design multiple emissions in a single chip on semi-polar (11-22) GaN. Based on the simulations, two different kinds of approach to achieving monolithically integrated white light LEDs have been developed. Detailed device characterization has been conducted, demonstrating that the objectives have been achieved. Furthermore, the long-term outstanding issues on polarization properties of semi-polar LEDs have been systematically studied by performing detailed optical measurements on our high performance semi-polar LEDs with a wide spectral region from blue to yellow, and finally a solid conclusion which has resolved the long standing debate has been drawn.

One of the simplest routes for the fabrication of a white LED is to comprise multiple InGaN quantum wells each with different emission wavelengths in an active region. The emission wavelength can be tuned by either the quantum well thickness or the indium composition. Nevertheless, such an approach exhibits complicated carrier

transport issues. This can be primarily attributed to the lower mobility of holes which lead to uneven hole distribution across the active region. In Chapter 4, by means of performing one-dimensional drift-diffusion simulations, carrier transport has been examined in (11-22) semi-polar LEDs with multi-colour emissions, which is also compared with its c-plane counterparts.

Chapter 5 presents two different kinds of approaches to the growth of monolithically integrated white light LEDs. The first approach is to grow multiple InGaN quantum well structures as an active region on semi-polar GaN surface based on simulation outcomes from Chapter 4, and the second approach is to grow yellow InGaN multiple quantum wells (MQWs) on a semi-polar blue LED, where part of the emission from the blue LED optically pumps the yellow MQWs in order to form white light.

Chapter 6 describes a systematic study of the optical polarization properties of (11-22) semipolar LEDs with a wide spectra region from blue to yellow. Semipolar LEDs exhibit intrinsic optical polarization which their c-plane counterparts lack. Therefore, semipolar LEDs are the ideal candidates for obtaining polarized light which is required for backlighting for liquid crystal displays.

I would like express my acknowledgements to members of the Centre of GaN materials and Device at the University of Sheffield who contributed in my Ph.D projects. The growth of all sample used in this thesis was done by Dr. Yiping Gong.

Dr. Zhang Yun, Dr. Jie Bai and Dr. Yipin Gong contributed to the wafer characterization of the overgrown semipolar (11-22) GaN on micro-rods templates. Additionally the LEDs which are used in Chapter 6 were fabricated by Dr. Jie Bai.

I did the simulations in Chapter 4 and I have also fabricated the LEDs samples used in Chapter 5. Dr. Jie Bai has contributed to the fabrication as well. Finally, the devices' characterization in Chapter 5, the optical polarization measurements and characterization in Chapter 6 were performed by me.

References

1. Addressing Climate Change. Available at: <https://en.unesco.org/themes/addressing-climate-change>. (Accessed: 2nd February 2020)
2. IPCC, Summary for Policymakers. In: *Global Warming of 1.5°C An IPCC Special Report on the impacts of global warming of 1.5°C above pre-industrial levels and related global greenhouse gas emission pathways, in the context of strengthening the global response to the threat of climate change, sustainable development, and efforts to eradicate poverty*. (In Press 2018)
3. The Paris Agreement | UNFCCC. Available at: <https://unfccc.int/process-and-meetings/the-paris-agreement/the-paris-agreement>. (Accessed: 14th February 2020)
4. Electricity Generation and Related CO2 Emissions | Planète Énergies. Available at: <https://www.planete-energies.com/en/medias/close/electricity-generation-and-related-co2-emissions>. (Accessed: 20th February 2020)
5. Emissions – Global Energy & CO2 Status Report 2019 – Analysis - IEA. Available at: <https://www.iea.org/reports/global-energy-and-co2-status-report-2019/emissions>. (Accessed: 3rd February 2020)
6. Global Temperature | Vital Signs – Climate Change: Vital Signs of the Planet. Available at: <https://climate.nasa.gov/vital-signs/global-temperature/>. (Accessed: 15th February 2020)
7. Zissis G., Energy Consumption and Environmental and Economic Impact of Lighting: The Current Situation. In *Handbook of Advanced Lighting Technology*

- (eds. Karlicek R., Sun CC., Zissis G., Ma R.) 1-13 (Springer, Cham, Switzerland 2016)
8. De Almeida, A., Santos, B., Bertoldi, P. & Quicheron, M., Solid state lighting review - Potential and challenges in Europe. *Renewable and Sustainable Energy Reviews* **34**, 30–48 (2014).
 9. Narukawa, Y., Ichikawa, M., Sanga, D., Sano, M. & Mukai, T., White light emitting diodes with super-high luminous efficacy. *J. Phys. D. Appl. Phys.* **43**, 6 (2010).
 10. Lighting | European Commission. Available at: https://ec.europa.eu/info/energy-climate-change-environment/standards-tools-and-labels/products-labelling-rules-and-requirements/energy-label-and-ecodesign/energy-efficient-products/lighting_en. (Accessed: 14th February 2020)
 11. Cho, J., Park, J. H., Kim, J. K. & Schubert, E. F., White light-emitting diodes: History, progress, and future. *Laser Photon. Rev.* **11**, 1600147 (2017).
 12. Murphy, T. W.. Maximum spectral luminous efficacy of white light. in *Journal of Applied Physics* **111**, 104909 (American Institute of Physics, 2012).
 13. Holonyak, N. & Bevacqua, S. F., COHERENT (VISIBLE) LIGHT EMISSION FROM Ga(As_{1-x}P_x) JUNCTIONS. *aip.scitation.org* **1**, 82–83 (1962).
 14. Holonyak, N., Bevacqua, S. F., Bielan, C. V & Lubowski, S. J., THE "DIRECT-INDIRECT" TRANSITION IN Ga(As_{1-x}P_x) p-n JUNCTIONS. *Appl. Phys. Lett* **3**, 47 (1963).
 15. Logan, R. A., White, H. G. & Wiegmann, W., Efficient green electroluminescence in nitrogen-doped gap p-n junctions. *Appl. Phys. Lett.* **13**, 139–141 (1968).

16. Groves, W. O., Herzog, A. H. & Craford, M. G., The effect of nitrogen doping on GaAs_{1-x}P_x electroluminescent diodes. *Appl. Phys. Lett.* **19**, 184–186 (1971).
17. Edmond, J. A., Kong, H. S. & Carter, C. H., Blue LEDs, UV photodiodes and high-temperature rectifiers in 6H-SiC. *Phys. B Phys. Condens. Matter* **185**, 453–460 (1993).
18. Willner, A. E. *et al.*, Optics and photonics: Key enabling technologies. in *Proceedings of the IEEE* **100**, 1604–1643 (Institute of Electrical and Electronics Engineers Inc., 2012).
19. Maruska, H. P. & Tietjen, J. J., The preparation and properties of vapor-deposited single-crystal-line GaN. *Appl. Phys. Lett.* **15**, 327–329 (1969).
20. Pankove, J. I., Miller, E. A., Richman, D. & Berkeyheiser, J. E., Electroluminescence in GaN. *Journal of Luminescence* **4**, 63–66 (1971).
21. Maruska, H. P., Rhines, W. C. & Stevenson, D. A., Preparation of Mg-doped GaN diodes exhibiting violet electroluminescence. *Mater. Res. Bull.* **7**, 777–781 (1972).
22. Manasevit, H. M., Erdmann, F. M. & Simpson, W. I., The Use of Metalorganics in the Preparation of Semiconductor Materials. *J. Electrochem. Soc.* **118**, 1864 (1971).
23. Hiramatsu, K. *et al.*, Growth mechanism of GaN grown on sapphire with AlN buffer layer by MOVPE. *J. Cryst. Growth* **115**, 628–633 (1991).
24. Amano, H., Sawaki, N., Akasaki, I. & Toyoda, Y., Metalorganic vapor phase epitaxial growth of a high quality GaN film using an AlN buffer layer. *Appl. Phys. Lett.* **48**, 353–355 (1986).
25. Amano, H., Kito, M., Hiramatsu, K. & Akasaki, I., P-type conduction in Mg-doped

- GaN treated with low-energy electron beam irradiation (LEEBI). *Jpn. J. Appl. Phys.* **28**, L2112–L2114 (1989).
26. Nakamura, S., Mukai, T., Senoh, M. & Iwasa, N., Thermal annealing effects on P-type Mg-doped GaN films. *Jpn. J. Appl. Phys.* **31**, 139–142 (1992).
27. Nakamura, S., Mukai, T. & Senoh, M., Candela-class high-brightness InGaN/AlGaIn double-heterostructure blue-light-emitting diodes. *Appl. Phys. Lett.* **64**, 1687–1689 (1994).
28. The Nobel Prize in Physics 2014. Available at: <https://www.nobelprize.org/prizes/physics/2014/summary/>. (Accessed: 15th February 2020)
29. Zhi zhen, Y., Jiawei, L. & Ya bou, X., GaN Heteroepitaxial Growth Techniques. *J. Microwaves Optoelectron.* **2**, (2001).
30. Park, S. S., Park, I. W. & Choh, S. H., Free-standing GaN substrates by hydride vapor phase epitaxy. *Jpn. J. Appl. Phys.* **39**, L1141 (2000).
31. Motoki, K. *et al.*, Preparation of Large Freestanding GaN Substrates by Hydride Vapor Phase Epitaxy Using GaAs as a Starting Substrate. *Jpn. J. Appl. Phys.* **40**, L140–L143 (2001).
32. Yoshida, T. *et al.*, Fabrication of 3-in GaN substrates by hydride vapor phase epitaxy using void-assisted separation method. *J. Cryst. Growth* **310**, 5–7 (2008).
33. Powell, A. *et al.* Growth of SiC substrates. *Int. J. High Speed Electron. Syst.* **16**, 751–777 (2006).
34. Takahashi, K., Yoshikawa, A., Sandhu, A., Ishitani, Y. & Kawakami, Y. *Wide, bandgap semiconductors: Fundamental properties and modern photonic and*

- electronic devices*. (Springer Berlin Heidelberg, 2007).
35. Takeuchi, T. et al., Determination of piezoelectric fields in strained GaInN quantum wells using the quantum-confined Stark effect. *Appl. Phys. Lett.* **73**, 1691–1693 (1998).
 36. Huang, C. F., Chen, C. Y., Lu, C. F. & Yang, C. C., Reduced injection current induced blueshift in an InGaNGaN quantum-well light-emitting diode of prestrained growth. *Appl. Phys. Lett.* **91**, 051121 (2007).
 37. Waltereit, P. et al., Nitride semiconductors free of electrostatic fields for efficient white light-emitting diodes. *Nature* **406**, 865–868 (2000).
 38. Funato, M. et al., Blue, green, and amber InGaN/GaN light-emitting diodes on semipolar {1122} GaN bulk substrates. *Japanese J. Appl. Physics, Part 2 Lett.* **45**, L659 (2006).
 39. Zhao, Y. et al., High-power blue-violet semipolar (2021) InGaN/GaN light-emitting diodes with low efficiency droop at 200 A/cm². *Appl. Phys. Express* **4**, 082104 (2011).
 40. Bai, J. et al., (11-22) semipolar InGaN emitters from green to amber on overgrown GaN on micro-rod templates. *Appl. Phys. Lett.* **107**, (2015).
 41. Krames, M. R. et al., Status and future of high-power light-emitting diodes for solid-state lighting. *IEEE/OSA J. Disp. Technol.* **3**, 160–175 (2007).
 42. Piprek, J., Efficiency droop in nitride-based light-emitting diodes. *Phys. status solidi* **207**, 2217–2225 (2010).
 43. Zhu, D. & Humphreys, C. J., Solid-state lighting based on light emitting diode technology. in *Optics in Our Time* 87–118 (Springer International Publishing, 2016).

44. Ooi, Y. K. & Zhang, J.. Design analysis of phosphor-free monolithic white light-emitting-diodes with InGaN/ InGaN multiple quantum wells on ternary InGaN substrates. *AIP Adv.* **5**, 057168 (2015).
45. Wernicke, T. *et al.*, Indium incorporation and emission wavelength of polar, nonpolar and semipolar InGaN quantum wells. *Semicond. Sci. Technol.* **27**, 024014 (2012).
46. Yizhar, O. *et al.*, Optogenetics in Neural Systems, *Neuron* **71**, 9–34 (2011).
47. Lammel, S., Tye, K. M. & Warden, M. R., Progress in understanding mood disorders: Optogenetic dissection of neural circuits, *Genes, Brain Behav.* **13**, 38–51 (2014).

CHAPTER 2

Background

2.1 Semiconductors

The classification of solids, according to their electrical properties depends upon their bandgap E_g , the energy separation between valence band (VB) and conduction band (CB). On this basis crystalline solids are categorized into conductors, semiconductors and insulators, as depicted in Figure 2.1.

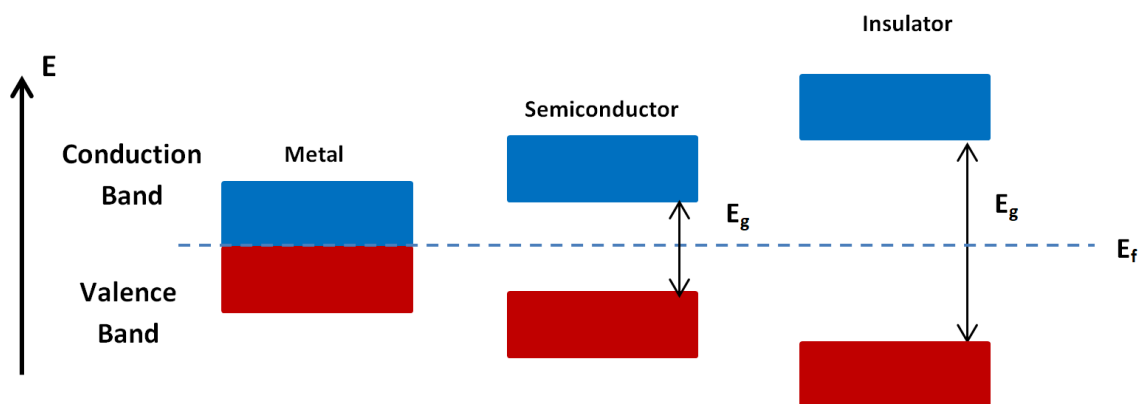


Figure 2.1 Schematic illustration of band-structure of conductor, semiconductor and insulator

Metals are conductive materials and are distinguished by the property that almost all carriers are in the CB and move freely in that band. The overlap of the valence band and conduction band in metals allows the presence of electrons in the conduction band even at room temperature without needing to any energy. In semiconductors

electrons can be excited from VB to CB when they gain energy which is equal to or larger than the bandgap of the material.

Conductivity is a measure which defines the ability of a material to conduct electrical charge, as oppose to its resistivity. The conductivity is defined as:

$$\sigma = ne\mu_n + pe\mu_p \quad (2.1)$$

Where, e is the electronic charge ($1.6 \times 10^{-19}\text{C}$) and μ_n and μ_p are the electron and the hole mobility, respectively; n and p are the electrons and holes concentrations, respectively. Conductors have large number of free electrons and exhibit conductivity in the order of $10^7 (\Omega \cdot \text{m})^{-1}$ whereas insulators exhibit very low conductivity in the order of $10^{-10} - 10^{-20} (\Omega \cdot \text{m})^{-1}$. Semiconductors conductivities lies between metals and insulators¹.

The conductivity of semiconductors can be controlled by introducing impurities in order to generate extra free electrons or holes. Dopants are categorized as n-type and p-type. For example, when magnesium Mg (group II element), is introduced into GaN, a portion of Ga atoms are replaced by Mg atoms leading to vacancies in valence band. Consequently, Mg-doped GaN becomes a p-type semiconductor with holes as majority carriers. On the other hand, when silicon Si, the group IV element, is doped into GaN, a portion of Ga atoms are replaced by Si atoms giving additional free electrons thus forming an n-type semiconductor. An extra energy level is formed in the forbidden region between CB and VB when impurities are introduced. The extra electron energy level generated in an n-type semiconductor lies just below the conduction band whereas for p-type lies just above the valence band.

2.2 Band Structure

The band structure in a semiconductor can be categorized in two types: direct bandgap structure or indirect bandgap structure. In a direct bandgap material the conduction band minimum and valence band maximum share the same point in k -space ($k=0$) and thus the occurrence of optical transitions does not involve any extra third party in order to maintain momentum conservation. However, in an indirect bandgap the CB minima and VB maxima have different k and thus an extra particle is required to be involved in the optical transition of electron-hole recombination in order to maintain momentum conservation. Therefore, extra phonons are introduced to the recombination processes of electrons and holes, as schematically illustrated in Figure 2.2.

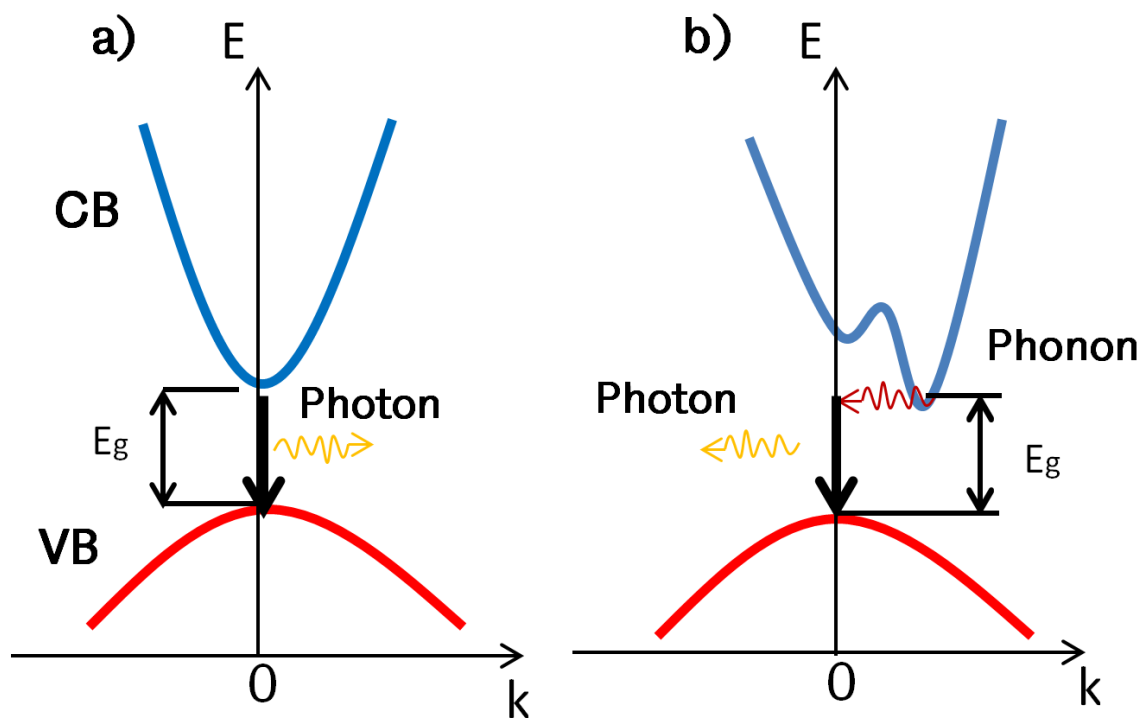


Figure 2.2 Schematics of a) direct and b) indirect band-structure

2.2.1 Absorption

Absorption occurs when an incident photon has greater energy than the bandgap of the material in order to excite an electron from a valence band to a conduction band. Furthermore, following Pauli's exclusion principle, the conduction band must have empty energy states to accept the upward transited electrons. Generally speaking, the minimum energy required for an electron to be excited to a conduction band from a valence band must maintain energy conservation as given below:

$$E_f = E_i + \hbar\omega \quad (2.2)$$

Where E_f is the energy in the conduction band minima, E_i is the energy state of electron at the valence band maximum and $\hbar\omega$ is the incident (absorbed) photon energy (where $\hbar = \frac{h}{2\pi}$). From the above equation it can be deduced that a photon must have at least energy equal to $E_f - E_i$ which is the bandgap E_g of the material. An absorption process leads to the creation of holes (absence of electrons) in a valence band and electrons in a conduction band, forming electron-hole pairs.

2.2.2 Luminescence

A luminescence process takes place via emitting photons when excited electrons in a conduction band return to a valence band by releasing energy in a form of photons. This process results in the emission of photons whose energy is equal to the bandgap of the material, assuming there is not any impurity or defect involved processes. However, a luminescence process depends on the recombination mechanisms of electron-holes and the crystal quality of the involved materials, and thus it can be

radiative or non-radiative. Luminescence is due to the consequence of radiative recombination processes.

2.3 Recombination Mechanisms

Figure 2.3 schematically illustrates a number of major electron-hole recombination mechanisms possibly existing in III-nitride semiconductors. Radiative recombination is a process by which the released energy is converted into photons, while in a non-radiative recombination process, the energy is eventually released in a form of thermal energy through different channels.

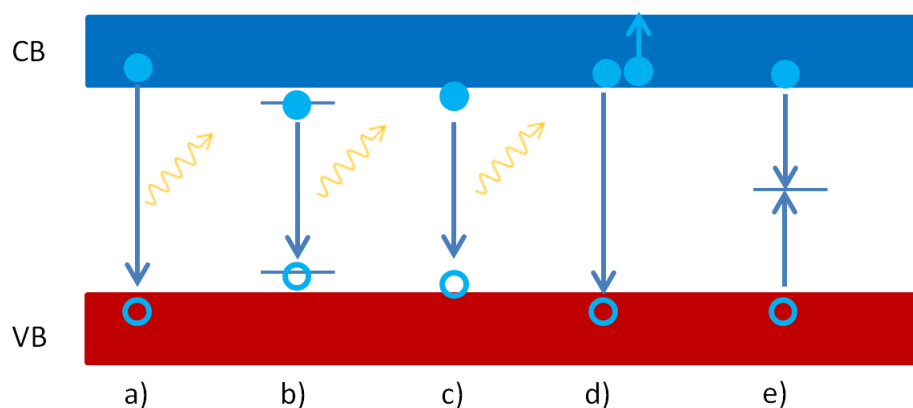


Figure 2.3 Schematic illustration of recombination mechanisms

Radiative recombination

a) Band edge emission

The first mechanism involves the radiative recombination procedure by which an electron in the CB loses its energy and recombines with a hole in the VB. This energy loss results in an emitted photon at the bandgap energy E_g of the semiconductor.

Donor-Acceptor Recombination

The second recombination mechanism relates to the case when impurities such as donors and acceptors are introduced. A doped semiconductor exhibits energy states just below the CB or just above the VB corresponding to the presence of n-type or p-type impurities respectively. The recombination via donor-acceptor energy states (levels) will result in an emitted photon with less energy than the band-gap of the material, depending on the activation energy of the corresponding dopants.

b) Excitonic recombination

Excitonic recombination is the process related to the formation of excitons which are created by the coulomb interactions between the oppositely charged carriers of electrons and holes. In particular, the Coulomb attraction between the carriers enhances the probability of the creation of electron-holes pairs and thus increases the probability of radiative transition.

Excitons can be characterized as neutrally charged particles and they are divided in two main categories. Wannier-Mott excitons are more likely to be found in semiconductors and they are considered as delocalized states with the ability to have free movement within the crystal. This type of excitons has a large radius which makes them weakly bound in the crystal. On the other hand, Frenkel excitons are mostly present in insulators. This kind of excitons have much smaller radius and they are tightly bound to atoms, thus prohibiting their movement within the crystal³.

The exciton binding energy can be calculated by taking into account the Bohr model for which:

$$E_n = -\frac{\mu}{m_o} \frac{1}{\epsilon_r^2} \frac{R_H}{n^2} \quad (2.3)$$

Where ϵ_r the dielectric constant of the material and R_H is the Rydberg energy of the hydrogen atom which is 13.6eV. The case of a stable exciton requires that the attraction potential must be high enough to withstand at room temperature $T=293K$ and satisfying the condition $E_n > K_B T^2$. The excitonic binding energy of GaN is 26meV, and thus stable excitons can be formed at room temperature⁴. The result of a radiative excitonic recombination is the emission of a photon with slightly smaller energy ($E_g - E_n$) than the energy band gap of the material.

Non-radiative recombination:

c) Auger recombination

Auger recombination takes place under a high excitation density, either optically or electrically. It is a process by which the released energy as a result of electron-hole recombination is used to excite to a higher energy level instead of being released as a photon⁵.

d) Shockley-Read-Hall

This is a type of non-radiative recombination mechanism which occurs when excited electrons release energy in a form of producing thermal energy heat (phonon) by falling to an intermediate energy level formed by crystal defects⁶.

The recombination lifetime take into account radiative process and non-radiative process, given by Equation 2.4, i.e., the sum of radiative recombination life time and non-radiative recombination lifetime:

$$\tau^{-1} = \tau_{rad}^{-1} + \tau_{non-rad}^{-1} \quad (2.4)$$

2.4 p-n Junction

A p-n junction diode is a device structure consisting of an n-doped layer and a p-doped layer, between which a depletion region is formed. The total diode current consists of two parts due to carrier drift and diffusion mechanisms. Under equilibrium conditions (no bias) a potential barrier which is termed as built-in potential is formed across the depletion region to prevent carriers further diffusing. The depletion region is formed by the ionized donor and acceptor created at the interfaces of n region and p region respectively. Therefore, under equilibrium state no net current flows through the device due to the built-in potential. Under forward bias across the p-n junction, the Fermi levels in the p and n region are shifted so that the potential barrier is reduced. Consequently, carrier diffusion is significantly enhanced, leading to a net diode current. Under reversed bias, the potential barrier is increased, leading to an enhancement in depletion region width.

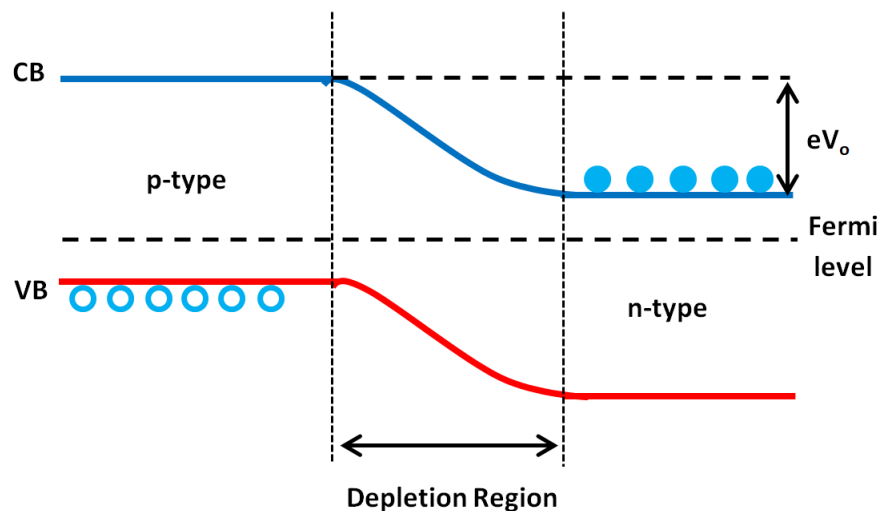


Figure 2.4 p-n junction band-structure under 0V bias

2.5 Light Emitting Diode

A standard LED consists of an active region sandwiched between a p-type layer and an n-type layer. Under forward bias, carrier recombination takes place, resulting in photon emission whose energy is mainly determined by the band gap of the material used in the active region. For a standard GaN based LED, an active region typically consists of an InGaN single quantum well (SQW) or InGaN multiple quantum wells (MQWs) sandwiched by GaN barriers. Due to significant difference between electron concentration in n-GaN and hole concentration in p-GaN, a thin p-type AlGaIn is used as an electron blocking layer which aims to reduce electron overflowing issues, followed by a final p-GaN layer. Figure 2.5 provides a schematic of a standard GaN based LED.

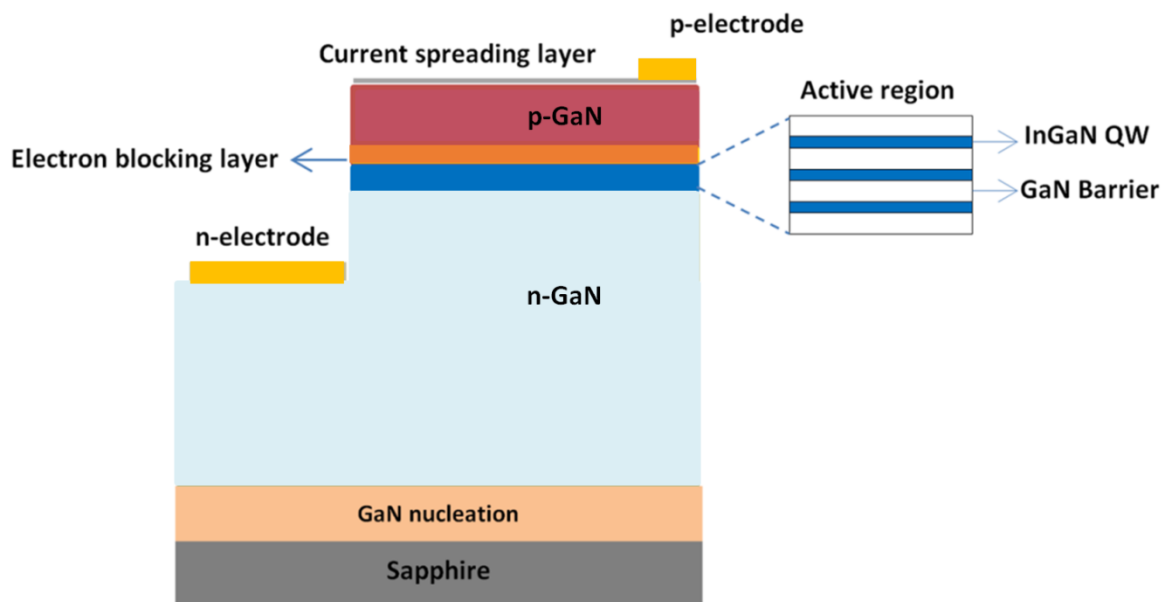


Figure 2.5 Schematic of LED structure

2.5.1 Low dimensional structures

A low-dimensional structure offers quantum confinement along at least one direction among X,Y,Z directions and can be classified according to their dimensionality as shown in Figure 2.6. Quantum confinement can be obtained if carriers can be confined in an area in at least one dimension whose dimension is comparable or smaller than the de Broglie wavelength of carriers. In this case, an extra quantization energy is generated along this particular direction. For example, if carriers such as either electrons or holes are confined along one direction, where the confined dimension in this particular direction is comparable or smaller than the de Broglie wavelength of carriers, car

riers cannot move freely along this particular direction but can still move freely in the other two directions. Such a structure is termed as a quantum well. This means a quantum well structure provides one dimensional confinement.

The de Broglie wavelength is defined as:

$$\lambda_d \approx \frac{h}{\sqrt{m_e^* k_B T}} \quad (2.5)$$

Where m_e^* is the electron's effective mass, k_B is Boltzmann constant and h is Planck's constant. In a bulk semiconductor, carriers can move freely in any direction.

A quantum wire structure allows carriers to move freely only along one direction, and thus is termed as two dimensional confinement. A quantum dot structure prohibits carriers to move freely in all dimensions and it is termed as three dimensional confinement.

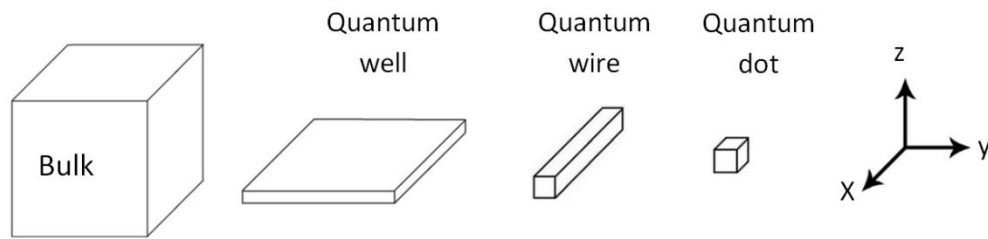


Figure 2.6 Schematic of quantum structures as a function of dimension

A quantum well structure has been widely used as an active region in III-nitrides optoelectronic devices. It can be formed by epitaxially growing a double heterostructure, where a smaller bandgap layer is sandwiched between two other semiconductor materials with larger band-gap which act as barriers. In the case of III-nitride based LEDs emitting in the visible region, GaN typically acts as a barrier while an InGaN quantum well acts as an emitting region. By varying the indium composition in InGaN, the bandgap energy can be tuned depending on the emission wavelength required. Light is emitted when the LED is applied under forward bias, where electron-hole recombination processes take place within the InGaN quantum well regions either radiatively or non-radiatively.

2.6 III-nitride Semiconductors

As mentioned above, the bandgaps of III-nitride semiconductors all with direct bandgap structures cover a wide spectral region across the entire alloys from deep UV through the whole visible spectrum to infrared. Furthermore, III-nitrides exhibit excellent high temperature stability and chemical inertness. Therefore, III-nitrides

semiconductors have been accepted as the ideal candidates for optoelectronics devices, in particular in the UV and visible spectral region.

2.6.1 Crystal Structure of III-nitride

Depending on atomic configuration, GaN exhibits three different kinds of crystal structure, namely, wurtzite, zinc-blende and rock-salt. GaN with a rock-salt structure is normally formed under high pressure in the order of ($>37\text{GPa}$), making it less attractive for applications under ambient conditions⁷. GaN with a zinc-blended cubic structure can be grown on cubic substrates, but tends to convert into a more thermodynamically stable wurtzite structure. GaN with a hexagonal wurtzite structure is the most widely used structure since it is the most thermodynamically stable structure. The wurtzite crystal structure exhibits a hexagonal closed packed configuration (HCP) of atoms along (0001) direction. Basic parameters to describe a wurtzite hexagonal unit cell are the in-plane lattice constant labeled as 'a' and the out of plane lattice constant labeled as 'c', which can be seen more clearly in Figure 2.7. The lattice constant 'a' represents the spacing between two adjacent atoms on a basal plane while 'c' represents the length of the unit cell which is the spacing between two adjacent basal planes. Table 2.1 provides the detailed lattice constants of GaN, AlN and InN all with a wurtzite structure.

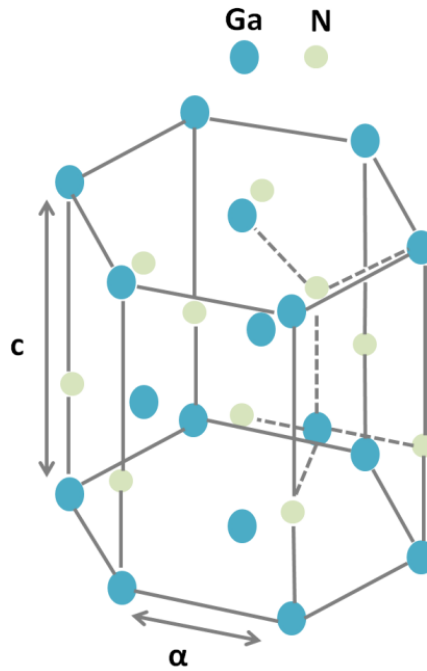


Figure 2.7 Schematic of atom configuration in GaN wurtzite structure

Material	Lattice Constant a (Å)	Lattice Constant c (Å)
GaN	3.189	5.185
AlN	3.112	4.982
InN	3.533	5.693

Table 2.1 Lattice constants of GaN, AlN and InN⁸

2.6.2 Chemical and Electrical Properties of III-nitrides

III-nitride semiconductors exhibit excellent chemical and thermal stability. Thus they can be suitable in a vast of applications in optoelectronics and power electronics. In particular, III-nitrides have the ability to withstand in extreme conditions due to their high melting point and high resistance to chemical solution. Nevertheless, under certain conditions GaN can be etched by wet etching by using chemical solutions of

KOH or NaOH at high temperatures. The materials properties of III-nitrides are depicted in table 2.2.

Material	Bandgap (eV)	Permittivity (F/m)	Refractive Index (n_x)	Melting Point °C
GaN	3.4	8.9	2.49	2500
AlN	6.2	8.5	2.18	3300
InN	0.65	15.3	2.9	1370

Table 2.2 Materials parameters of InN, GaN and AlN^{9,10,11}

Table 2.3 depicts a comparison of the electrical properties of GaN with other III-V semiconductor. The highest electron mobility of $1245\text{cm}^2\text{V}^{-1}\text{s}^{-1}$ was obtained on GaN on a freestanding GaN substrate¹². The wide bandgap along with other superior electrical properties in comparison with other III-V semiconductors, such as high thermal conductivity and high breakdown voltage, makes GaN an ideal candidate for the fabrication of high power, high frequency, high temperature electronic devices.

Material	Bandgap (eV)	Electron mobility (cm^2/Vs)	Breakdown Field (MV/cm)	Thermal Conductivity ($\text{Wcm}^{-1}\text{K}^{-1}$)
InP	1.34	5400	0.5	0.68
GaAs	1.4	8500	0.4	0.5
GaN	3.4	1245	5	2.1

Table 2.3 Electrical and thermal properties of InP, GaAs and GaN^{12,13,14,15}

2.6.3 Spontaneous and Piezoelectric Polarizations

Owing to the inversion symmetry of III-nitride semiconductors with a wurtzite structure, spontaneous polarization is generated along the c-direction. In the case of an InGaN/GaN heterostructure, the strain induced by the lattice-mismatch between GaN and InGaN moves the atoms from equilibrium resulting in piezoelectric polarization. The magnitude of piezoelectric polarization can be calculated by the following equation:

$$\mathbf{P}_z = e_{31}(\varepsilon_{xx} + \varepsilon_{yy}) + e_{33}\varepsilon_{zz} \quad (2.6)$$

Where ε_{xx} and ε_{yy} are the isotropic in plane strain and ε_{zz} is the out of plane strain along the c axis, considering a c-plane III-nitride semiconductor with a wurtzite structure and e_{31} and e_{32} represent the piezoelectric constants. Therefore,

$$\varepsilon_{xx} = \varepsilon_{yy} = \frac{(a-a_0)}{a_0} \quad (2.7)$$

$$\varepsilon_{zz} = \frac{(c-c_0)}{c_0} \quad (2.8)$$

Where a and a_0 are the in-plane strain lattice constant and the strain-free lattice constant, respectively. c and c_0 are the out of plane lattice constants under strain and strain-free, respectively. The total polarization can be expressed as the sum of the spontaneous and piezoelectric polarizations:

$$\mathbf{P} = \mathbf{P}_{sp} + \mathbf{P}_{pz} \quad (2.9)$$

The electric field generated by the polarization field will substantially affect quantum well structures grown on c-plane substrates. The electron-hole wavefunctions will be

pulled apart by the electric field. As a result, radiative recombination lifetime increases leading to a reduced efficiency of optical devices.

2.7 Semi-polar and non-polar III nitrides

The great achievements of III-nitrides materials and optoelectronics are mainly limited to InGaN based blue emitters grown on c-plane orientation. The polar orientation poses a number of fundamental issues which suppress the great potential of III-nitrides optoelectronics as mentioned above. Longer wavelengths with high indium content are generating strong piezoelectric fields. This will result to an increase in QCSE and therefore to lower efficiencies as we move towards green and yellow emissions. Furthermore, a limited indium incorporation rate in InGaN on c-plane GaN restrict the growth of high performance green and yellow LEDs, the key elements for achieving monolithic white LEDs. A number of approaches have been proposed in order to suppress the QCSE and also enhance indium incorporation. Growth of III-nitrides along semi-polar and non-polar orientation is one of the most promising approaches to circumvent the fundamental issues.

Figure 2.8 illustrates a number of typical orientations for semipolar and non-polar GaN. Non-polar GaN, such as (1-100) m-plane GaN or (11-20) a-plane GaN, is perpendicular to the basal c-plane, while semi-polar GaN, such as (11-22) and (10-11) GaN, is in an inclination angle with respect to the c-axis, which is between the non-polar and the polar c-plane. (11-22) semipolar GaN has an inclined angle of 58.4° related to the c-axis, whereas (10-11) GaN has an inclined angle of 62° .

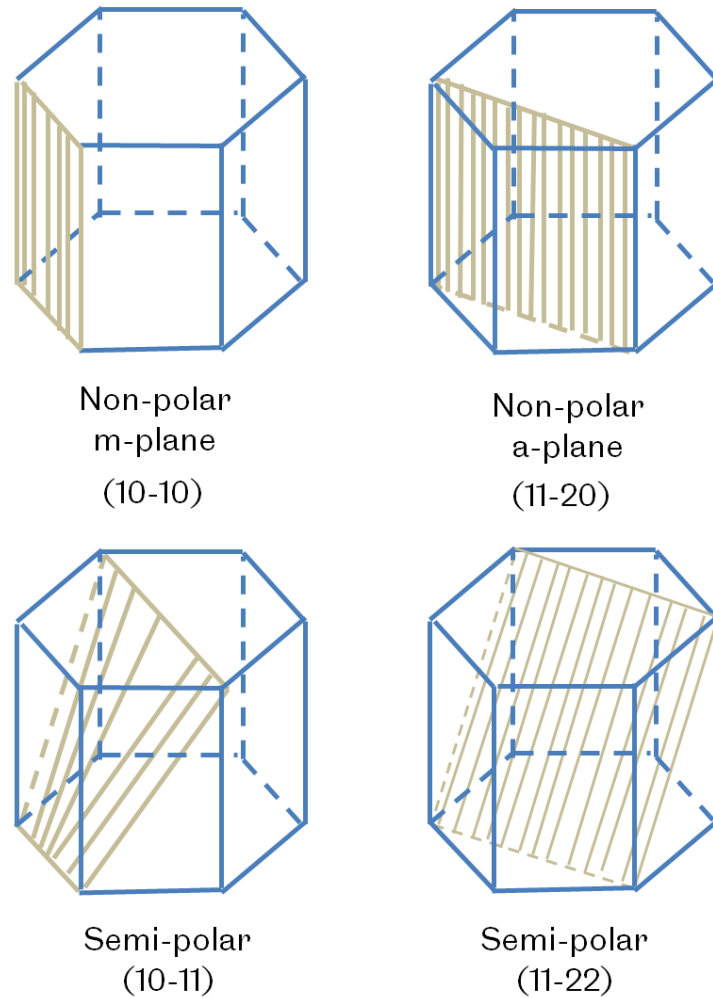


Figure 2.8 Schematic of commonly used hexagonal planes

2.7.1 Reduced polarization piezoelectric fields

Figure 2.9 depicts the dependence of piezoelectric polarization and electron-hole wavefunction overlap of a 3 nm $\text{In}_{0.25}\text{Ga}_{0.75}\text{N}$ quantum well as a function of the angle between the substrate normal and the c -axis. It is apparent that the piezoelectric polarization reduces as the inclined angle increases and approaches zero at an inclined angle of 45° . Above 45° , piezoelectric polarization exhibits opposite polarity and starts to increase in a reverse direction until it becomes zero at 90° . The zero piezoelectric polarization corresponds to the non-polar planes.

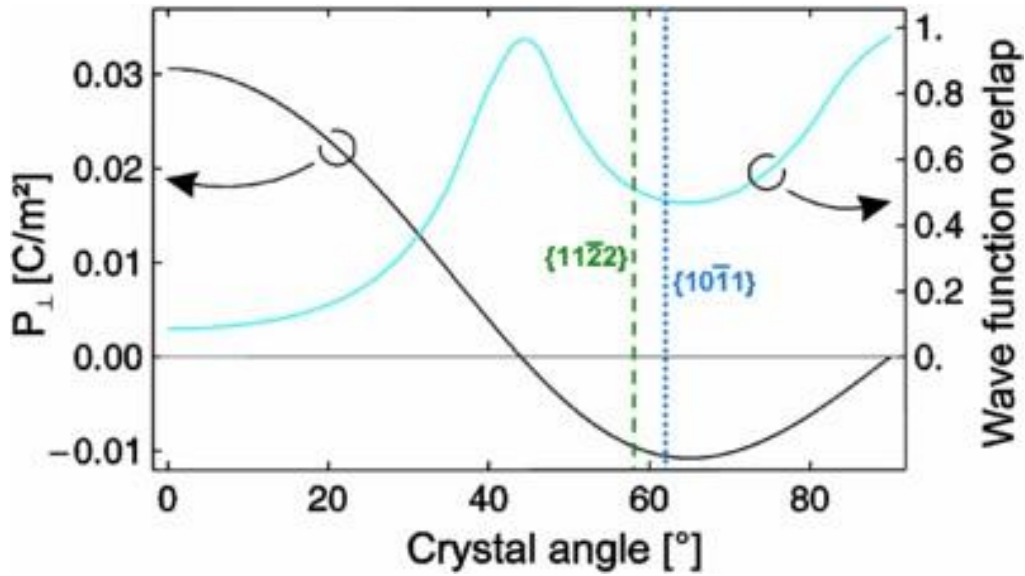


Figure 2.9 Piezoelectric polarization and electron – hole wavefunction overlap as a function of crystal angle with respect to c-plane orientation in a 3 nm $\text{In}_{0.25}\text{Ga}_{0.75}\text{N}$ quantum well¹⁵

2.7.2 Indium incorporation

Among all the semi-polar orientations, the (11-22) GaN has gained much attention for growing long wavelength emitters. This is attributed to the fact that (11-22) GaN exhibits enhanced indium incorporation efficiency^{16,17}. A systematic study about indium incorporation dependence for several orientations such as (0001), (10-12), (11-22), (20-21) and (10-11) orientations has been conducted by Wernicke et al.¹⁶. Their findings have shown that InGaN grown on the (10-11) and (11-22) GaN exhibits an enhanced indium incorporation rate in comparison that on c-plane counterpart, while InGaN grown on either the (20-21) or (10-12) GaN exhibits a similar indium incorporation with that on the c-plane GaN. According to their results the order of indium incorporation can be expressed as:

$$(10 - 11) > (11 - 22) > (0001) = (20 - 21) = (10 - 12) \quad (2.10)$$

Although (10-11) GaN favors the growth of InGaN with high indium content, the growth of GaN on (10-11) GaN suffers from severe surfaces issues, where hillocks are naturally formed during its epitaxial growth, whereas (11-22) does not exhibit such a growth issue. Therefore, (11-22) GaN would be the best choice for the growth of long wavelength such as green or yellow III-nitride LEDs, namely, InGaN LEDs with high indium content.

2.7.3 Growth of (11-22) semipolar GaN

Although semipolar (11-22) GaN can be grown directly on m-plane sapphire by using the two step growth approach as used for c-plane GaN growth on sapphire, crystal quality is very far from satisfactory. Unlike c-plane GaN, where basal stacking faults (BSFs) are not an issue, semi-polar GaN BSFs are observed along a direction with an inclination angle to the c-axis. As a result BSFs extend to the surface, while for c-plane GaN BSFs are suppressed at the interface between GaN and sapphire substrate. Consequently, it is difficult to grow semi-polar GaN with high crystal quality on sapphire.

Of course, it is ideal to have homo-epitaxial growth of semipolar GaN optoelectronics. However, it is impossible to obtain free-standing semi-polar GaN substrates with a reasonably large size, such as 2" substrates at the moment. Typically semi-polar GaN substrates are obtained by means of growing thick c-plane GaN on sapphire by HVPE and then cleaving along a semipolar orientation^{18,19}. This significantly limits the size of free-standing substrates in addition to extremely expensive price. Different growth techniques are employed for improving the crystal quality of semipolar (11-22). Selective growth on patterned r-plane sapphire for growing (11-22) semi-polar GaN

have been proposed by Okada et al²⁰. For *r*-plane sapphire, the angle between the *c*-axis and the *r*-axis is 57.6° which is similar to 58.4 the inclination angle between of (11-22) GaN and *c*-plane GaN. If *r*-plane sapphire is patterned as shown in Figure 2.10, (11-22) semi-polar GaN can be obtained by selectively growing GaN on the *c*-axis on such a patterned *r*-plane sapphire. Nevertheless, the key issue is due to the great challenge in patterning such *r*-plane sapphire with an accurate inclination angle of ~58° in a reasonably good quality, as sapphire is extremely chemically inert and thus it is extremely difficult to make such patterning by either dry-etching or chemical etching.

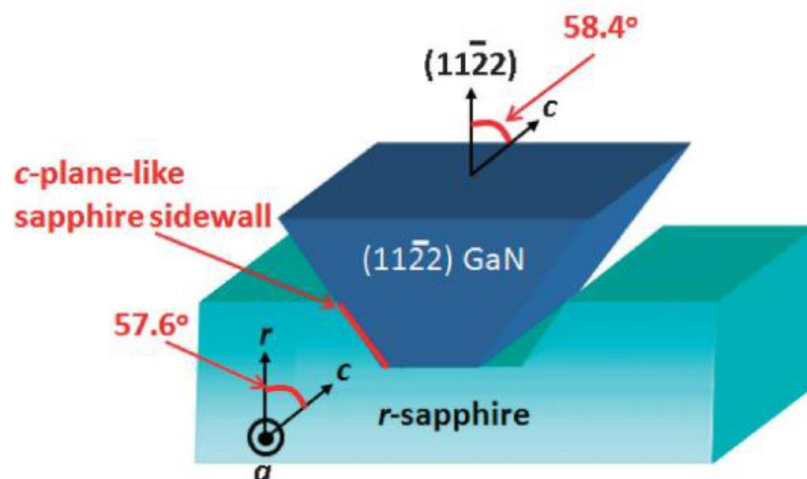


Figure 2.10 Schematic of patterned *r*-plane sapphire for growing semi-polar (11-22) GaN²⁰

Overgrowth on patterned templates has also been employed for improving the crystal quality of semipolar (11-22) GaN on sapphire²¹. Recently our group has established a cost-effective overgrowth technique by using regularly micro-rod templates demonstrating very high crystal quality²². For the realization of this approach standard semi-polar (11-22) GaN (generally, low quality) is initially grown on

an m-plane sapphire to act as a template. A SiO₂ layer is then deposited on the GaN template by plasma enhance chemical vapor deposition (PECVD). Standard photolithography process and dry etching are subsequently conducted in order to form regularly arrayed SiO₂ micro-rods. The SiO₂ micro-rods act as a secondary mask for further etching the GaN underneath the SiO₂. Regularly arrayed GaN micro-rod arrays are formed while the SiO₂ remains on the top. The overgrowth takes place from the sidewalls of the micro rods and finally a total coalescence will be achieved, exhibiting a high crystal quality with a typical dislocation density of $2 \times 10^8 \text{ cm}^{-2}$ and a typical basal stacking fault density of $4 \times 10^4 \text{ cm}^{-2}$ ²². The significant reduced defects are attributed to the SiO₂ which effectively blocks the penetration of defects and coalescence process during the overgrowth. Based on this overgrowth approach, semi-polar InGaN LEDs with high performance in a wide spectral region of up to amber has been recently demonstrated²³. Figure 2.11 illustrates the schematic of the micro-rods template process.

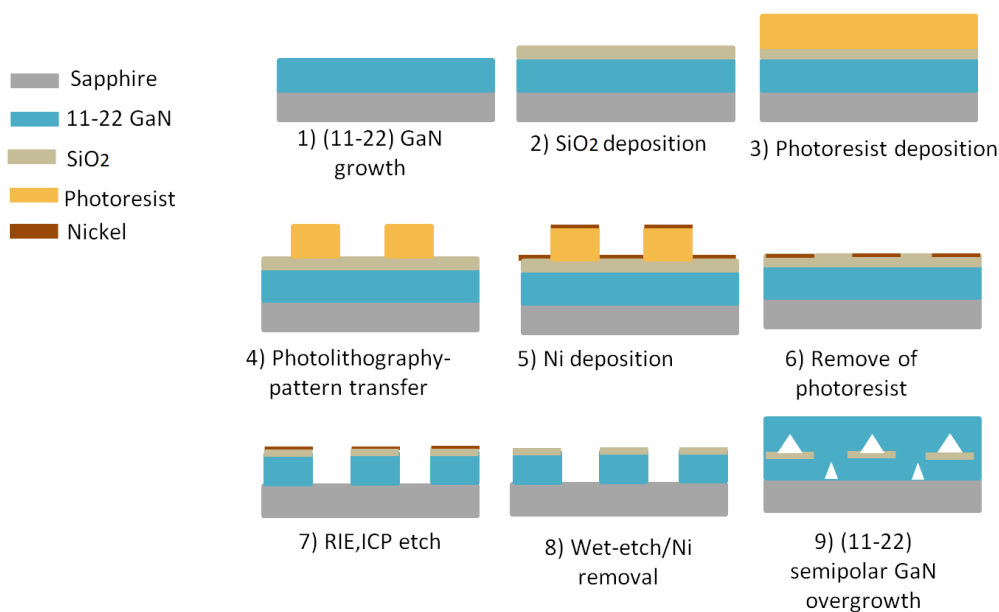


Figure 2.11 Schematic of the fabrication processes of micro-rods template

References

1. Callister, W. D & Rethwisch, D. G., *Materials Science and Engineering: An Introduction. Eighth Edition* (John Wiley & Sons, Inc., 2010).
2. Fox, M. *Optical Properties of Solids. Second Edition* (Oxford University Press, 2010)
3. Wannier, G. H., The structure of electronic excitation levels in insulating crystals. *Phys. Rev.* **52**, 191–197 (1937).
4. Reshchikov, M. A. & Morko, H., Luminescence properties of defects in GaN. *J. Appl. Phys.* **97**, 061301 (2005).
5. Römer, F. & Witzigmann, B.. Effect of Auger recombination and leakage on the droop in InGaN/GaN quantum well LEDs. *Opt. Express* **22**, A1440 (2014).
6. Shockley, W. & Read, W. T., Statistics of the recombinations of holes and electrons. *Phys. Rev.* **87**, 835–842 (1952).
7. Xia, H., Xia, Q. & Ruoff, A. L., High-pressure structure of gallium nitride: Wurtzite-to-rocksalt phase transition. *Phys. Rev. B* **47**, 12925–12928 (1993).
8. Morkoç, H. *Handbook of Nitride Semiconductors and Devices Vol. 1: Materials Properties, Physics and Growth*. (Wiley-VCH Verlag GmbH & Co. KGaA, 2008).
9. Van Vechten, J. A., Quantum dielectric theory of electronegativity in covalent systems. III. Pressure-temperature phase diagrams, heats of mixing, and distribution coefficients. *Phys. Rev. B* **7**, 1479–1507 (1973).
10. Karpiński, J., Jun, J. & Porowski, S., Equilibrium pressure of N₂ over GaN and high pressure solution growth of GaN. *J. Cryst. Growth* **66**, 1–10 (1984).
11. Davydov, S. Y., Estimates of the spontaneous polarization and permittivities of AlN, GaN, InN, and SiC crystals. *Phys. Solid State* **51**, 1231–1235 (2009).

12. Look, D. C. & Szelove, J. R., Predicted maximum mobility in bulk GaN. *Appl. Phys. Lett.* **79**, 1133–1135 (2001).
13. Levinshtein, M., Rumyantsev, S. & Shur, M., *Properties of Advanced Semiconductor Materials: GaN, AlN, InN, BN, SiC, SiGe*. (John Wiley & Sons, Inc., 2001).
14. Takahashi, K., Yoshikawa, A., Sandhu, A., Ishitani, Y. & Kawakami, Y., *Wide bandgap semiconductors: Fundamental properties and modern photonic and electronic devices*. (Springer Berlin Heidelberg, 2007)
15. Scholz, F., Semipolar GaN grown on foreign substrates: a review. *Semicond. Sci. Technol.* **27**, 024002 (2012).
16. Wernicke, T. *et al.*, Indium incorporation and emission wavelength of polar, nonpolar and semipolar InGaN quantum wells. *Semicond. Sci. Technol.* **27**, 024014 (2012).
17. Zhao, Y. *et al.*, Indium incorporation and emission properties of nonpolar and semipolar InGaN quantum wells. *Appl. Phys. Lett.* **100**, 201108 (2012).
18. Fujito, K., Kubo, S. & Fujimura, I., Development of Bulk GaN Crystals and Nonpolar/Semipolar Substrates by HVPE. *cambridge.org* **34**, (2009).
19. Fujito, K. *et al.*, Bulk GaN crystals grown by HVPE. *J. Cryst. Growth* **311**, 3011–3014 (2009).
20. Okada, N., Kurisu, A., Murakami, K. & Tadatomo, K., Growth of semipolar (1122) GaN layer by controlling anisotropic growth rates in r-plane patterned sapphire substrate. *Appl. Phys. Express* **2**, 091001 (2009).
21. Wang, T., Topical Review: Development of overgrown semi-polar GaN for high efficiency green/yellow emission. *Semicond. Sci. Technol.* **31**, 093003 (2016).

22. Zhang, Y. et al., Defect reduction in overgrown semi-polar (11-22) GaN on a regularly arrayed micro-rod array template, *AIP Advances* **6**, 025201 (2016).
23. Bai, J. *et al.* (11-22) semipolar InGaN emitters from green to amber on overgrown GaN on micro-rod templates. *Appl. Phys. Lett.* **107**, (2015).

CHAPTER 3

Experimental techniques

3.1 Introduction

This chapter presents various experimental techniques utilized in this project for LED fabrication and material and device characterization including photoluminescence (PL) and electroluminescence (EL).

3.2 Fabrication Technique

3.2.1 Photolithography

Photolithography is a standard technique by which a pattern from a pre-designed mask can be transferred onto an epiwafer by using a UV sensitive photoresist. Photolithography needs to be carried out in a yellow room in order to prevent any ambient illumination which will unintentionally react with the photoresist. Photoresists can be classified as positive and negative photoresists depending on the chemical reaction when exposed to UV radiation. For a positive photoresist, the exposed area becomes more soluble and can be easily removed with its counterpart developer solution. For a negative photoresist the exposed area becomes insoluble and cannot be removed during subsequent developing processes.

A typical photolithography procedure follows an initial soft-baking process on an epiwafer at 100°C for 1 minute in order to remove any moisture and allow a good adhesion with the photoresist. A spin-coating process is used for spin coating the photoresist on the sample. A spin coating technique utilizes the centripetal acceleration of the spinning stage to achieve a uniform spread of the photoresist. EMS model 400 spin coater is used in this work. The speed of the spinner controls the thickness of photoresist and is set at 4000rpm and the dwell time is 30 seconds. Once the sample is spin-coated it is placed on a hot plate at 100°C for 1 minute. Depending on fabrication steps required and photoresist with a desired thickness, two kinds of positive photoresists, namely BPRS-200 and SPR-350, are used for transferring the desired patterned mask. BPRS-200 is used for the mesa-etch step which requires ICP etching, since it provides a thick layer of around 2µm at 4000rpm spin speed and can withstand longer etching process. For metallization schemes the SPR-350 is used which has a thinner layer of around 1µm at 4000rpm spin speed and provides an easier lift off. The desired mask is transferred to the surface of the sample by using a KARL SUSS MJB3 Mask Aligner, where UV radiation (365nm) exposes the photoresist. A diluted solution of MF26A is used to remove the exposed area, with a developing time optimized at 60 seconds. Figure 3.1 illustrates our mask aligner system used in this work.

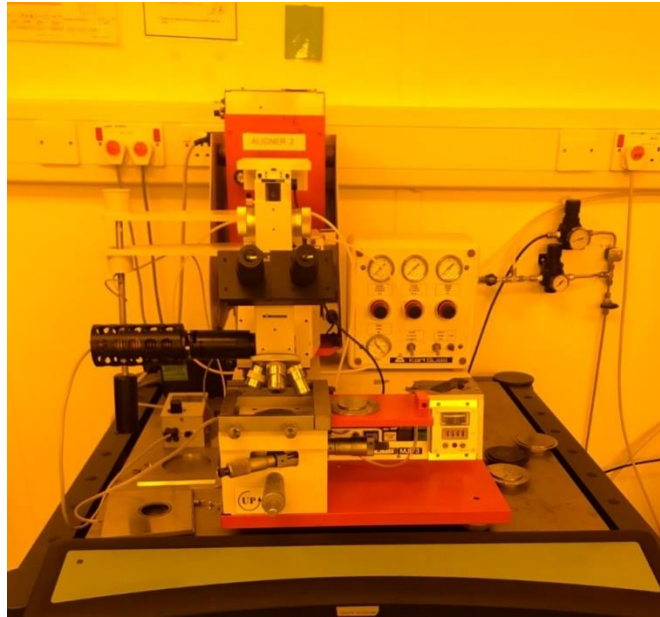


Figure 3.1 Karl Suss MJB3 mask aligner

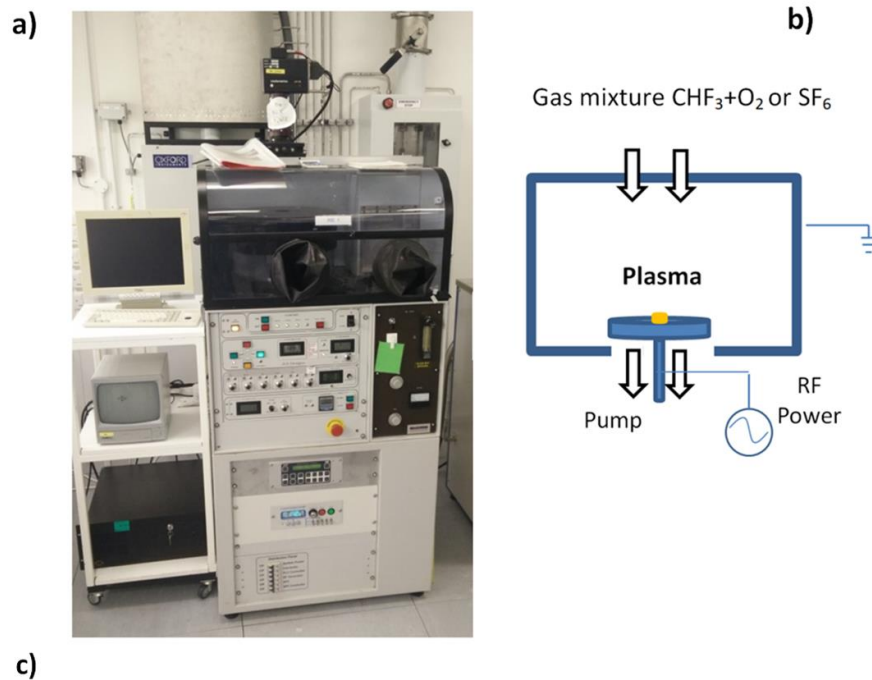
3.2.2 Dry etching techniques

The etching techniques aim is to selectively remove desired regions from an epiwafer. The unwanted material can be removed by dry etching techniques, where the semiconductor is placed in a vacuum chamber and bombarded by reactive ions. Dry etch technique has been commonly used in the fabrication of semiconductor devices. Depending on purpose, dry-etching techniques provide a high etching rate with a good material selectivity and high anisotropy¹.

Reactive-Ion Etching (RIE)

Reactive-ion etching (RIE) utilizes etchant gases in the presences of a radio frequency (RF) electric field that generates plasma. The selective area is removed by ion bombardment which is created by reactive ions within the plasma. RIE is usually used to etch dielectric materials, such as SiO_2 and SiN . Depending on the material which needs to be etched, a table listed below provides detailed etching conditions.

Normally, RF power determines an etching rate. Figure 3.2a shows the image of our Plasma-Therm RIE system used in this work, while Figure 3.2b schematically illustrates the configuration within the chamber.



Etching material	Gasses	Gas flow (sccm)	RF power	Etch rate nm/min
SiO ₂	CHF ₃ +SF ₆	30/10	80	20
SiN	CHF ₃ + O ₂	35/5	80	20

Figure 3.2 a) RIE system used in this work, b) Schematic of RIE system and c) Optimized conditions for material etching

Inductively Coupled plasma (ICP)

Inductively Coupled plasma (ICP) generates higher plasma density than a RIE system in order to etch III-nitrides. Powerful and directional plasma can be generated by electromagnetic fields. Figure 3.3a shows an Oxford Instruments Plasmalab System 100 used in this work and Figure 3.3b shows the schematic configuration.

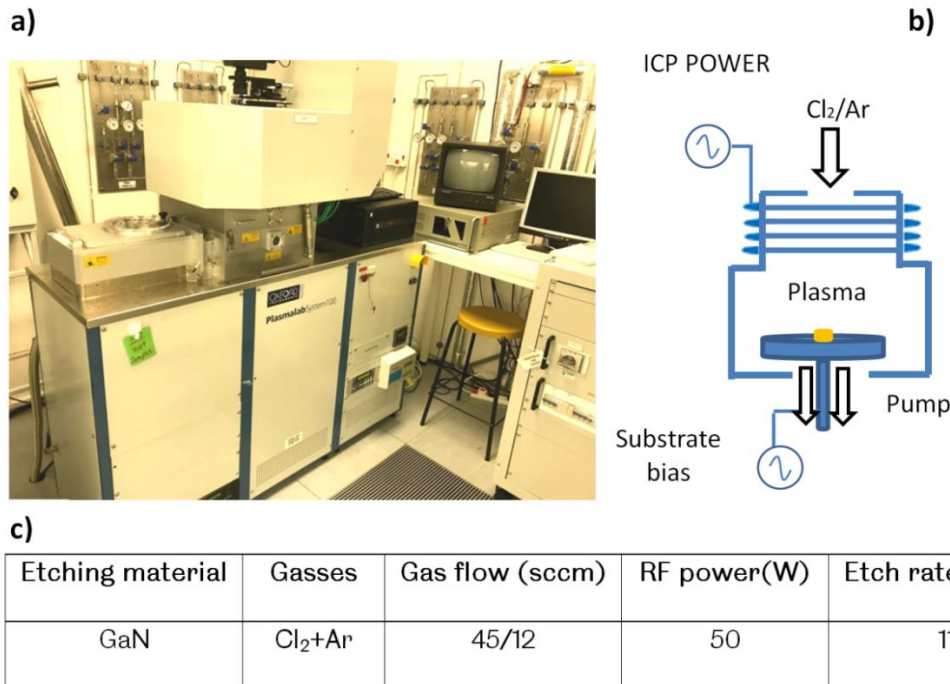


Figure 3.3 a) ICP system used in this work, b) schematic of ICP system and c) recipe for GaN etching

Reactive gases are introduced to an ICP chamber and ions formed in the plasma are used to etch through GaN layers. For GaN etching, a mixture of Cl₂/Ar gases is used and high anisotropy and a fast etching rate can be obtained². RF power and gas flow can be monitored and controlled via software. For etching GaN the ICP power is set at 450W, whereas the etching power is kept as low as 50W. Cl₂/Ar gases flow rates are 45/12 sccm respectively. This particular recipe delivers an etching rate of approximately 110nm/min (Figure 3.3c). The etching recipes conditions have been determined by members of our group. The RF power normally determines an etching rate and is usually kept at low levels to minimize damages to samples during ICP dry-etching processes³. These particular damages may result in significant degradation in LED performance, generating extra non-radiative recombination centres⁴. An in-situ

monitoring system is used to monitor an etch depth, where a laser system is used to measure the reflectivity of the etched sample.

3.2.3 Thin Film Deposition

Thermal Evaporator

Metal Thin film Deposition

A variety of metals such as Al, Au, Ti, and Ni can be deposited by using thermal evaporation under high vacuum conditions. In this work an Edwards E306A thermal evaporator is used (Figure 3.4) for the deposition of metals for n and p-contacts, p-type current spreading layer and bond pads of LEDs. Thermal evaporator is used because it provides better lift-off than sputter. In sputter deposition the target is placed in an angle in relation to the sample and thus enhancing sidewall deposition. For a better lift off process a vertical configuration such as in thermal evaporator is preferred in order to minimize sidewall deposition.

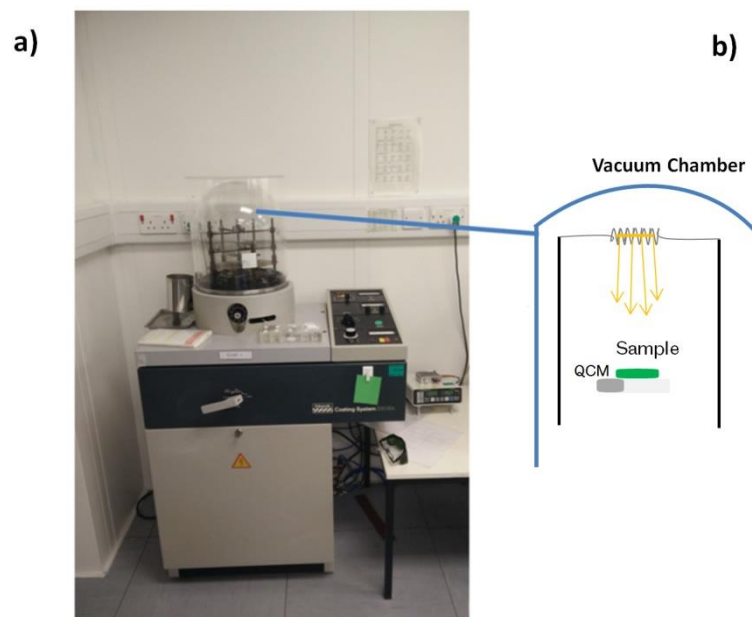


Figure 3.4 a) Edwards E306A Thermal evaporator and b) schematic illustration

The metals are placed into a tungsten coil. The coil is then placed in a distance of approximately 12 cm above the sample to prevent any potential detrimental effects on the sample caused by exposure to a high temperature. A metal deposition rate can be monitored by using a quartz crystal monitor (QCM). The sample is placed next to QCM. Once the chamber vacuum is pumped down up to $\sim 10^{-6}$ Torr, metals are melted and then evaporated by passing a large amount of current through the tungsten coil (in order of 10s of Amps).

Plasma Enhanced Chemical Vapour Deposition (PECVD)

Dielectric materials such as SiN and SiO₂ can be deposited by using plasma enhanced chemical vapour deposition (PECVD). During the deposition process chemical reactions take place from the reactant gases in a vacuum chamber. For the deposition of SiO₂ the combination of reactant gases is SiH₄, N₂ and N₂O. Plasma is generated by a radio frequency wave between two parallel metal plates. The sample is placed on a substrate which is typically heated to 300°C. Due to the presence of plasma in PECVD dielectric films can be deposited in lower temperature than in conventional CVD process and thus higher quality dielectric films can be achieved⁵

The Figure 3.5 illustrates a Plasma-Therm 790 PECVD system.

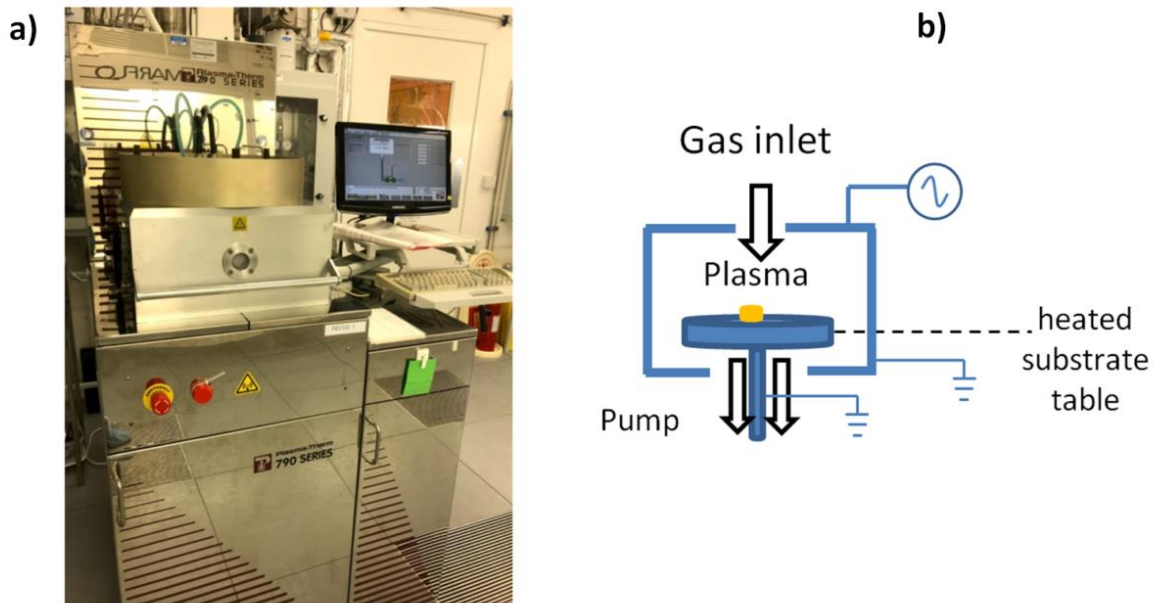


Figure 3.5 a) Plasma-Therm 790 PECVD system and b) schematic illustration

3.2.4 Rapid thermal annealing (RTA)

Rapid thermal annealing (RTA) is used for p-type activation and post-annealing treatment for p-contacts. In this work a Jipelec rapid thermal annealing system is used. High temperature can be reached by the use of halogen lamps and can be monitored by a pyrometer and a thermocouple. Thermocouple and pyrometer control are operated at low and high temperature ranges respectively.

P-type activation was performed under N_2 ambient at $675^{\circ}C$ for 20 minutes. For the annealing-treatment of p-contact, the sample is annealed at $550^{\circ}C$ in air for 1 minute. Once annealing processes are completed, a cooling process is followed by flowing a high flow-rate of nitrogen. Figure 3.6 illustrates the RTA used in this work.



Figure 3.6 Jipelec thermal annealing system

3.4 LED fabrication procedure

The fabrication of LED requires the utilization of the above techniques. Depending on LED structures additional steps may be required and will be described in detail in Chapter 5.

Sample cleaning

Before any fabrication procedure it is of vital importance to conduct a standard cleaning process in order to remove any contaminations on a sample surface. Samples are initially immersed in n-butyl acetate and baked at 150°C, followed by a rigorous wash in an ultrasonic bath with acetone and isopropyl alcohol in order to remove any unwanted residues from the sample surface.

Activation of p-type material

The inevitable incorporation of hydrogen during MOVPE p-GaN growth leads to the formation of Mg-H complexes, the fundamental reason to stop as-grown magnesium-doped GaN being p-type GaN. Therefore, an activation procedure is required to break the Mg-H bonds in order to allow the magnesium to act as a p-type dopant. A post-annealing process at temperatures above 600°C is necessary to dissociate the Mg-H complexes⁶. Our p-type activation procedure is to perform a post-annealing process in a rapid thermal annealing chamber under N₂ ambient at 675°C for 20 minutes.

The fabrication steps of a standard LED are depicted in Figure 3.7

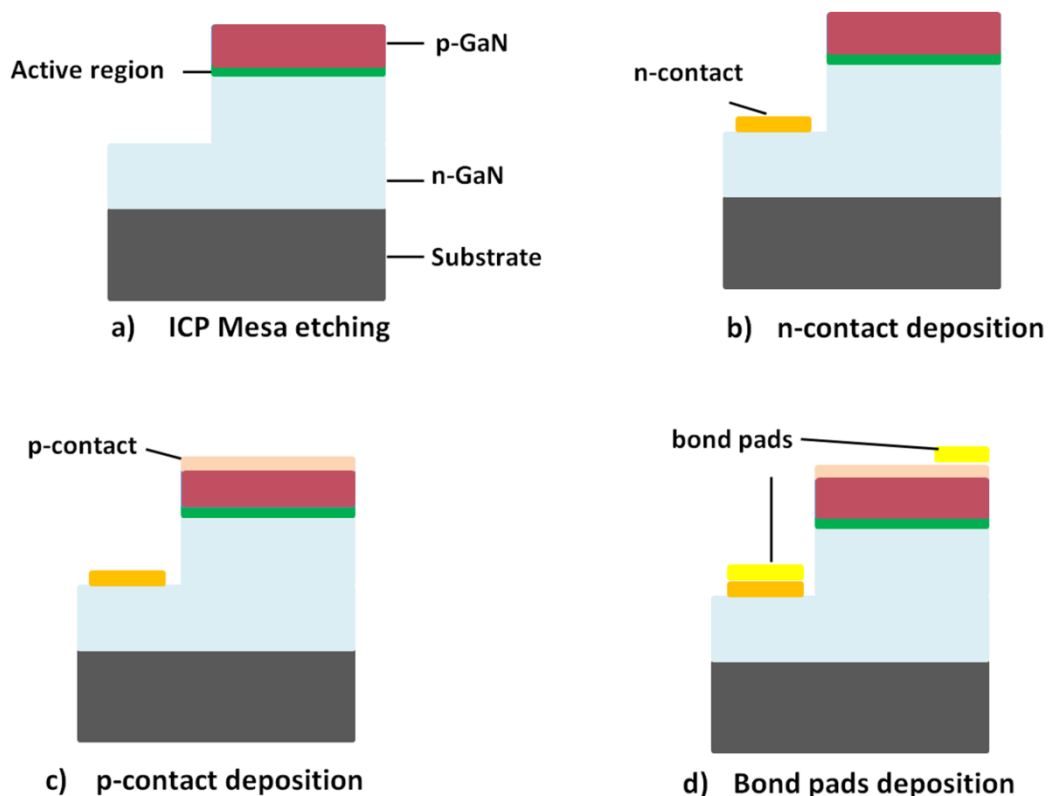


Figure 3.7 Schematic illustration of LED fabrication

a) Mesa - etching

The initial step for LED fabrication involves mesa etching. This is conducted by initially using a photolithography technique to define an LED mesa (typically $330 \times 330 \mu\text{m}^2$ in our case). The sample is subsequently subjected to dry etching technique to expose the n-GaN region. Mesa etch is accomplished by using inductively couple plasma reactive ion etching (ICP) and by using the recipe for GaN etching. The etching time was 4 minutes, achieving an etching depth of around 400nm.

b) n-type Contact photolithography and metal deposition

The objective of this step is to define the n-contact region and deposit metal alloy to form ohmic contact on n-GaN. The photolithography technique for defining the n-contact follows the same procedure as mentioned above. The patterned mask of n-contact has to be aligned with the pre-defined mask used for the mesa-etch in order to avoid any short circuit situation between the p-type and n-type layers. Among several metallization schemes a standard Ti/Al/Ti/Au alloy as n-contact is typically deposited on n-GaN⁷ because it exhibits a low resistivity on the order of $\rho_s = 6 \times 10^{-7} \Omega\text{cm}^2$, where Ti/Al/Ti/Au are deposited with their thicknesses of 20/100/20/60 nm, respectively.

c) P-Type contact

Indium Tin Oxide (ITO) or thin Ni/Au are typical metal used for the fabrication p-contact on p-GaN. ITO enables high optical transparency but exhibits lower electrical characteristics than Ni/Au⁸.

A standard Ni/Au (7nm/7nm) metallization scheme is used for the fabrication of p-contact. The semi-transparent layer exhibits a transmittance of $\sim 80\%$ ⁹. A surface treatment is performed prior to the deposition of Ni/Au alloy by removing/reducing any possible oxide layer on the p-GaN. For this purpose, the sample is typically immersed in HCl: H₂O (1:1) for 1 minute¹⁰. Subsequently the Ni/Au alloy is deposited by using a thermal evaporator. The sample is then annealed at 550⁰C for 1 minute for metallization and also forms an oxidized semitransparent p-contact. Upon oxidization a contact resistance of the p-contact layer is 11.3 Ω /sq.

ITO is deposited by sputter deposition under high vacuum where plasma is generated in the presence of an electric field and chemically inert gas such as argon. A vapor of atoms is sputtered from the ITO target by ion bombardment. The sample is place on a rotatable stage to achieve uniform deposition.



Figure 3.8 Schematic illustration of current path a) without current spreading layer and b) with current spreading layer.

d) Bond-pads

The last step of fabrication requires the deposition of a thick bi-layer of Ti/Au (20nm/200nm) for p and n bond pads. The bond-pads are used as the areas where the electrical probes are attached for performing device characterization or device bonding.

3.5 Optical and Electrical characterization

3.5.1 Photoluminescence

A photoluminescence (PL) measurement is a powerful optical characterization technique, by which optical properties can be investigated¹². A laser is typically used as an excitation source. Depending on LED structures, an appropriate excitation light source is used. For a LED which has an active region of InGaN/GaN quantum wells, a 375nm diode laser is used to investigate the optical properties of the LED. The 375 nm photons will be transparent to the GaN layer which has an approximate a band-gap of 365nm. PL measurement is a quick way of extracting useful information from a sample without requiring any fabrication unlike electroluminescence measurements. Fig 3.9 illustrates the PL system used in this study. A 375nm continuous wave (CW) laser diode is used as an excitation light source which is reflected by an aluminum mirror with reflectivity >99%. The laser beam is then focused through a lens to a beam spot with approximately 200 μm in diameter on a sample. The sample is mounted in a helium closed loop cryostat with a temperature range from room temperature down to 10K. A 0.5 m monochromator with spectral resolution of 0.02nm is used to disperse the emission from the sample, which is then detected by thermoelectrically (TE) cooled CCD detector which can reach -70°C.

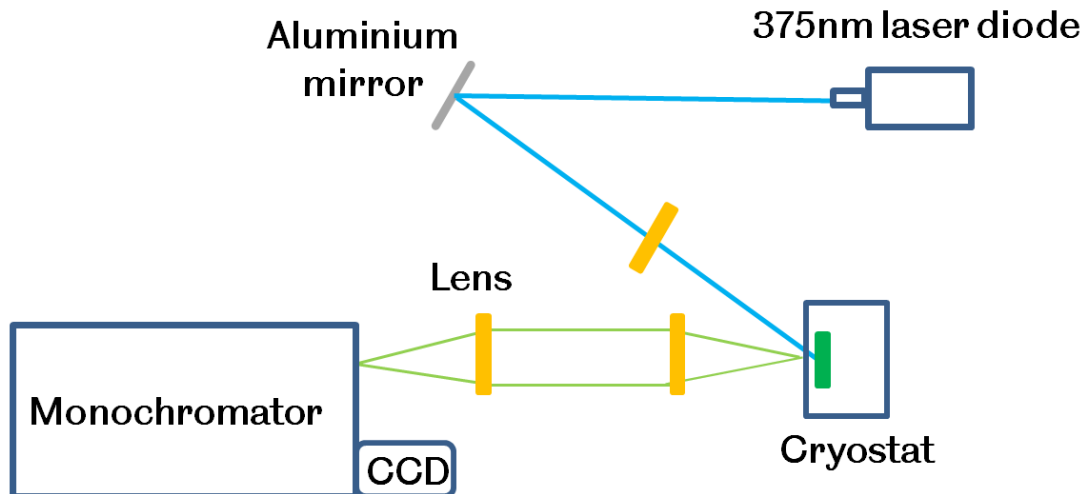


Figure 3.9 Schematic diagram of photoluminescence system

3.5.2 Electroluminescence

Electroluminescence (EL) measurements are conducted on a LED operated under a forward bias. Figure 3.11 shows the schematic of the EL system used in this study. The probe station consists of a Standa motorized XY station which has a movement range of 75 x 75 mm. In order to locate n- or p- contact to probe LEDs, an optical microscope is mounted to a separated combined motorized Standa stage providing 100mm Z movement and the ability of 360⁰ rotation, for angular depended measurements. A Keithley 2400 Source Meter is utilized as an electrical excitation source. An infinity corrected high magnification objective 50x with 0.42 NA is used to collect EL emission, which is directed through a 50:50 beam splitter with a CMOS camera used to observe the surface of the sample. The emission is then introduced into a monochromator via a fiber collimator and finally detected by an Andor Newton

CCD. A rotatable polarizer is placed between the beam splitter and the fiber collimator allowing for polarized EL measurements presented in Chapter 6.

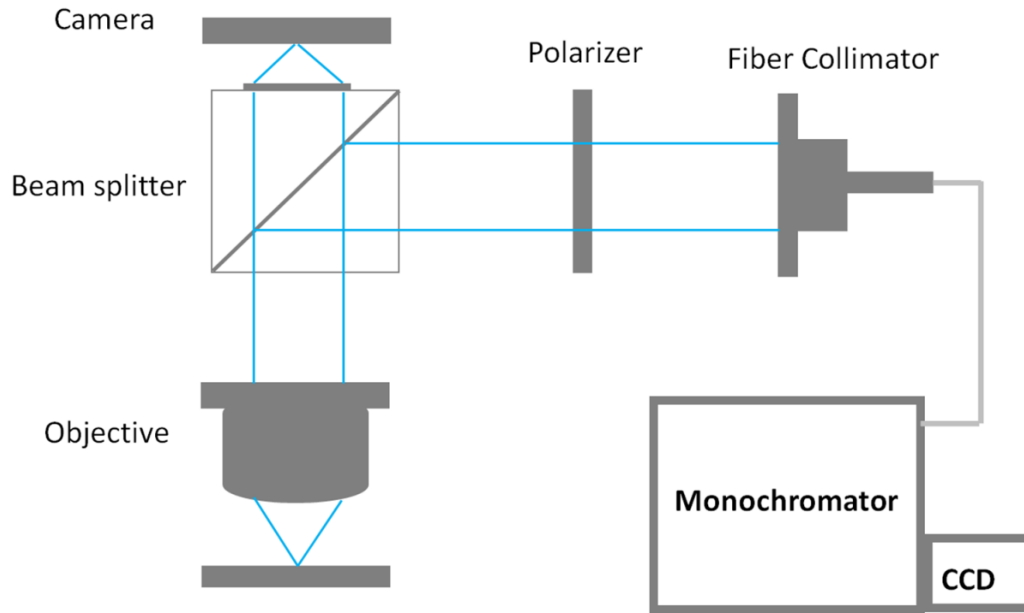


Figure 3.10: Schematic diagram of electroluminescence system

References

1. Smith, S. A. *et al.*, High rate and selective etching of GaN, AlGa_N, and AlN using an inductively coupled plasma. *Appl. Phys. Lett.* **71**, 3631–3633 (1997).
2. Sheu, J. K. *et al.*, Inductively coupled plasma etching of GaN using Cl₂/Ar and Cl₂/N₂ gases. *J. Appl. Phys.* **85**, 1970–1974 (1999).
3. Morkoç, H., *Handbook of Nitride Semiconductors and Devices Vol. 1: Materials Properties, Physics and Growth*. (WILEY-VCH Verlag GmbH & Co. KGaA, 2008).
4. Lee, J. M., Huh, C., Kim, D. J. & Park, S. J., Dry-etch damage and its recovery in InGa_N/Ga_N multi-quantum-well light-emitting diodes. *Semicond. Sci. Technol.* **18**, 530–534 (2003).
5. Hamedani, Y., Macha, P., Bunning, T. J., Naik, R. R. & Vasudev, M. C., Plasma-Enhanced Chemical Vapor Deposition: Where we are and the Outlook for the Future. in *Chemical Vapor Deposition - Recent Advances and Applications in Optical, Solar Cells and Solid State Devices* (InTech, 2016).
6. Götz, W., Johnson, N. M., Walker, J., Bour, D. P. & Street, R. A., Activation of acceptors in Mg-doped Ga_N grown by metalorganic chemical vapor deposition. *Appl. Phys. Lett.* **68**, 667 (1995).
7. Wang, D. F. *et al.*, Low-resistance Ti/Al/Ti/Au multilayer ohmic contact to n-Ga_N. *J. Appl. Phys.* **89**, 6214–6217 (2001).
8. Margalith, T. *et al.*, Indium tin oxide contacts to gallium nitride optoelectronic devices. *Appl. Phys. Lett.* **74**, 3930 (1999).

9. Oh, M. et al., Silver Nanowire Transparent Conductive Electrodes for High-Efficiency III-Nitride Light-Emitting Diodes. *Sci. Rep.* 5, 13483 (2015).
10. Chary, I. et al., Influence of surface treatment and annealing temperature on the formation of low-resistance Au/Ni ohmic contacts to p-GaN. in *Journal of Electronic Materials* 38, 545–550 (2009).
11. Ho, J.-K. *et al.*, Low-resistance ohmic contacts to p-type GaN. *Appl. Phys. Lett.* 74, 1275 (1999).
12. Perkowitz, S., *Optical characterization of semiconductors: infrared, Raman, and photoluminescence spectroscopy.* (Elsevier, 2012).

Chapter 4

Carrier transport in multi-colour (11-22) semi-polar LEDs

Chapter 4 presents a detailed simulation study of investigating carrier transport issues in a monolithic on-chip (11-22) semi-polar GaN based white LED with different designs. The 1st section will be focused on a single chip white LED consisting of yellow and blue emissions, demonstrating that the growth order of yellow and blue InGaN quantum wells plays a critically important role in achieving white emission. The growth order needs to be yellow InGaN quantum wells first and then a blue InGaN quantum well after the growth of n-type GaN. The fundamental reason is due to the poor hole concentration distribution across the whole InGaN quantum well region. In order to effectively capture holes in both the yellow InGaN quantum wells and the blue InGaN quantum well, a thin GaN spacer has been introduced prior to the blue InGaN quantum well. Detailed simulations of the band diagram and the hole concentration distribution across the yellow and the blue quantum wells have been conducted, showing that the thin GaN spacer can effectively balance the hole concentration between the yellow and the blue InGaN quantum wells, eventually determining their relative intensity between the yellow and the blue emissions. The 2nd section will be on a simulation study of a tri-chromatic white LED by rebalancing

hole distribution across the active region, demonstrating that three color emission can be achieved by utilizing semi-polar InGaN emitters in the active region.

4.1 Introduction

One of the most direct routes for the fabrication of monolithic white LEDs is to utilize InGaN quantum wells with different emission wavelengths, where these emissions with different wavelengths can be obtained by controlling either InGaN quantum well (QW) thickness or indium content in InGaN^{1,2,3,4,5}. In this approach, a combination of either blue/green/red (RGB) emissions or blue/yellow emissions is required. However, two major challenges need to be addressed before the potential of this approach can be possibly achieved. The first challenge is to obtain long wavelengths such as green and yellow emission with high performance. Current III-nitride LEDs are grown on c-plane substrates. The polar orientation poses strain-induced piezoelectric fields due to the lattice-mismatch between InGaN and GaN, which is the so-called quantum-confined Stark effect (QCSE). As a result, internal quantum efficiency is reduced, and drops significantly further when InGaN quantum wells move towards longer wavelengths such as the green or yellow spectral region (where higher indium content is required, leading to an enhancement in QCSE), thus forming the well-known “Green-Yellow gap” phenomenon. Furthermore, the c-plane GaN also leads to fundamental limitations in incorporating indium into GaN^{6,7}. The second issue is due to the complicated carrier transport in InGaN QWs with different indium composition as a result of much lower hole mobility and hole concentration than those of electrons, potentially leading to severe non-uniform carrier distribution across all the InGaN QWs involved. This issue becomes even more complicated with

increasing indium content as a result of an enhancement in piezo-electrical fields induced polarization. So far, there is no systematic study addressing this issue.

Growth of III-nitrides along a semi-polar direction, in particular the (11-22) orientation, would be a promising solution to achieve long wavelength emissions, as this orientation is expected to lead to not only significantly reduced piezoelectric polarization fields but also enhanced indium incorporation efficiency in InGaN^{8,9}. Recently, Sizov et al¹⁰ observed severe non-uniform carrier distribution among the InGaN multiple quantum wells (MQWs) of a laser diode (LD) grown on a c-plane substrate, leading to an increase in threshold current when the number of InGaN MQWs is above 2, while they did not observe this phenomenon on the LDs grown on semi-polar substrates. This fact also indicates that semi-polar orientation facilitates the distribution of injection current across InGaN QWs along the vertical direction. All the above facts demonstrate that (11-22) semi-polar GaN is potentially an ideal candidate which can meet all the requirements for the fabrication of monolithic white LEDs with multiple-color emissions.

In this chapter, by means of performing detailed simulations, carrier transport issues in (11-22) semi-polar white LEDs with two different InGaN quantum wells (blue and yellow) have been initially studied. This study has been further compared with its c-plane counterpart, demonstrating the major advantages of employing semi-polar (11-22) GaN for the growth of monolithic white LEDs. Moreover, a further simulation study has been conducted, and the design of a trichromatic LED structure is possible by balancing the distribution of hole carriers across the active region.

4.2 Methods

Simulator of Light Emitters based on Nitride Semiconductors (SiLENSe) 5.11 package has been used to perform the simulations of band diagrams, carrier concentration and electron-luminescence spectra^{11,12}. The simulations are conducted using a one-dimensional drift-diffusion model based on the self-consistent solution of the Poisson equations for the electrostatic potential and the Fermi-Dirac statistics for carrier concentration in active regions. Although semi-polar InGaN LEDs exhibit reduced polarization induced electrical fields, simulations have taken into account the polarization effect in addition to radiative recombination and non-radiative recombination as a result of defects. The emission spectra from the active region are simulated by solving the self-consistent Poisson and Schrödinger equations for electron and hole wave functions for each quantum well. The complex structure of the valence band of III nitride materials is obtained within the 8×8 Kane Hamiltonian.

The electron and hole concentrations are generally expressed as

$$n = N_c \cdot F_{1/2} \left(\frac{F_n - E_c + q\varphi}{kT} \right) \quad (4.1)$$

$$p = N_v \cdot F_{1/2} \left(\frac{E_v - F_p - q\varphi}{kT} \right) \quad (4.2)$$

Where φ is the electric potential; F_n and F_p are the electron and hole quasi Fermi level accordingly; k is the Boltzmann constant; T is the temperature; q is the electron charge and N_c and N_v are the effective density of states in a conduction and a valence band.

The electric potential distribution φ in the LED structure is generally expressed by utilizing Poisson equation:

$$\frac{d}{dz} \left(P_z^o - \varepsilon_0 \varepsilon_{33} \frac{d\varphi}{dz} \right) = q [N_D^+ - N_A^- + p - n] \quad (4.3)$$

Where N_D^+ and N_A^- are the concentration of ionized donors and acceptors, respectively; ε_0 is the dielectric permittivity of vacuum; ε_{33} the component of the static dielectric constant tensor.

The continuity equations for electrons and holes in an LED are given below, where \mathbf{J}_n and \mathbf{J}_p are the electron and hole fluxes, respectively.

$$\nabla \cdot \mathbf{J}_n = -R, \quad \mathbf{J}_n = -\frac{\mu_n n}{q} \nabla F_n \quad (4.4)$$

$$\nabla \cdot \mathbf{J}_p = -R, \quad \mathbf{J}_p = \frac{\mu_p p}{q} \nabla F_p \quad (4.5)$$

Where R is the recombination rate of carriers and μ_n and μ_p are electron and hole mobilities, respectively. The current densities of electron and holes can be expressed from the fluxes such as $\mathbf{j}_n = -q\mathbf{J}_n$ and $\mathbf{j}_p = +q\mathbf{J}_p$. The electron and hole fluxes depend on the gradient of their quasi Fermi levels.

The total recombination rate R considers both non-radiative and radiative channels:

$$R = R^{rad} + R^{SRH} + R^{Aug} \quad (4.6)$$

Where R^{rad} is the radiative recombination rate; R^{SHR} is the Shockley-Read-Hall recombination rate and R^{Aug} is the Auger recombination rate.

Emission spectra are simulated by solving the Schrödinger equations for electron and hole wave functions in each quantum well. The Schrödinger equations for electron and holes envelope functions can be expressed as

$$-\frac{\hbar^2}{2m_n^\perp} \frac{d^2\Psi_n}{dz^2} + (E_c - q\phi)\Psi_n = E\Psi_n, \quad \frac{\hbar^2}{2m_s^\perp} \frac{d^2\Psi_s}{dz^2} + (E_s + q\phi)\Psi_s = E\Psi_s \quad (4.7)$$

Where m_n^\perp, m_s^\perp is the effective mass of electron and hole along a growth direction; Ψ_n and Ψ_s are defined as their envelop functions. The following flow chart diagram represents the simulation procedure,

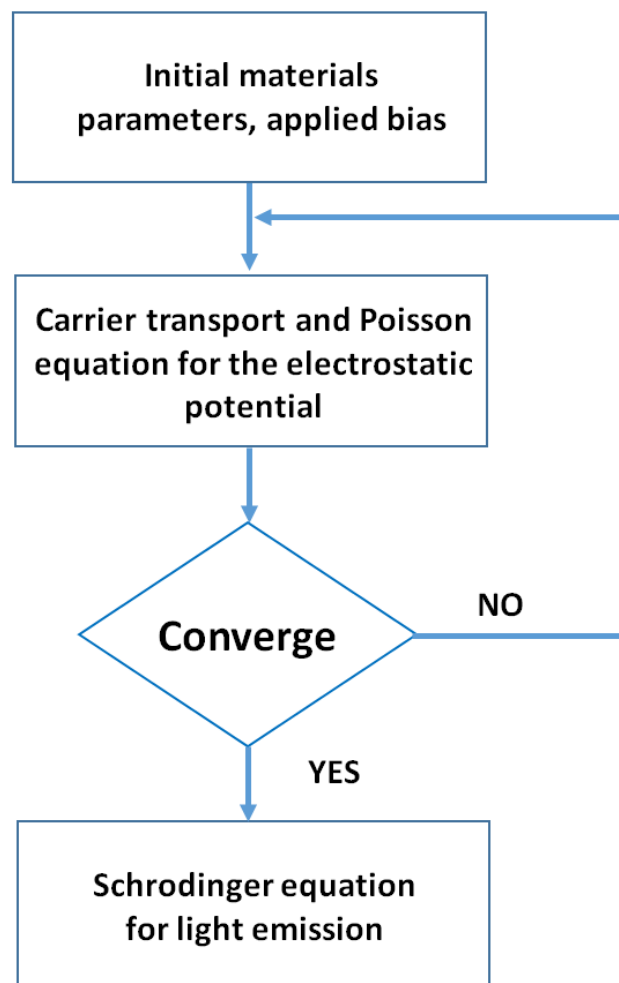


Figure 4.1 Flow chart diagram of the simulation procedures

The materials properties used for the simulation are listed in the following tables.

Parameter	Units		AlN	GaN	InN
Lattice constant	nm	α	0.3111	0.3182	0.3540
Dielectric constant		ϵ_{33}	8.5	8.9	15.3
Piezoelectric tensor	C/m^2	e_{31}	-0.58	-0.33	-0.22
Piezoelectric tensor	C/m^2	e_{33}	1.55	0.65	0.43
Elastic Constant	GP_a	C_{13}	115	105	95
Elastic constant	GP_a	C_{33}	385	395	200
Spontaneous Polarization	C/m^2	P^{sp}	-0.081	-0.029	-0.032
Band gap	eV	E_g	6.2	3.4	0.7

Table 4.1 Basic GaN materials parameters in c-plane¹¹

	AlN		GaN		InN	
	\perp	\parallel	\perp	\parallel	\perp	\parallel
m_n	0.25	0.25	0.2	0.2	0.1	0.1
m_{lh}	1.95	0.25	1.1	0.15	1.35	0.1
m_{hh}	1.95	2.58	1.1	1.65	1.35	1.45
m_{so}	0.23	1.93	0.15	1.1	0.09	1.54

Table 4.2 Effective electron and hole masses in binary nitrides at 300K with m^\perp and m^\parallel are the in-plane and normal to the growth direction effective masses¹¹

4.3 Dual color LED on (11-22) semipolar and c-plane orientation

Initially, band-diagram simulations have been performed on a dual-colour LED (consisting of blue and yellow) with an identical structure grown on a (11-22) GaN surface and a c-plane GaN surface, respectively, in order to study the effect of the crystal orientation on carrier transportation. In both cases, the LED structure simulated consists of two pairs of InGaN MQWs for yellow emission followed by a blue single quantum well (SQW). The thicknesses of the quantum well and the barrier are 4 nm and 9 nm, respectively. Despite the fact that the indium incorporation is naturally limited in c-plane LED, both LEDs are designed to have similar emission wavelength. In both device structures InGaN quantum barriers with low indium content were used in order to reduce the strain across the quantum wells. The donor and acceptor concentrations used for the simulations are $5 \times 10^{18} \text{ cm}^{-3}$ and $5 \times 10^{17} \text{ cm}^{-3}$, respectively, which are fairly standard. Figure 4.2 illustrate the schematic illustration of the LED structure in c-plane and semi-polar respectively.

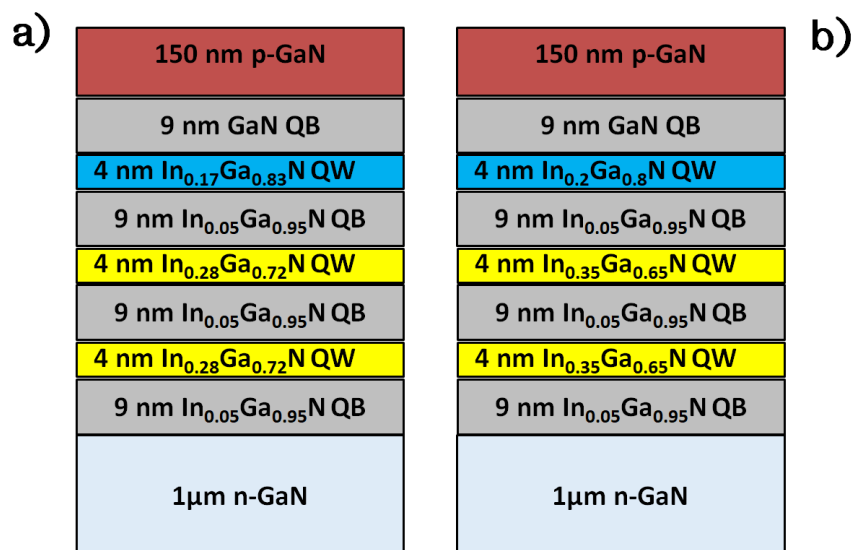


Figure 4.2 Schematics of LED structure in a) c-plane and b) (11-22) orientation

Figure 4.3 shows the simulation results of the two cases. The simulation of band diagrams and the carrier distribution of c-plane and semi-polar (11-22) LEDs have been conducted at injection current density at $180\text{A}/\text{cm}^2$ (equivalent to 200 mA on a standard LED with a size of $330 \times 330 \mu\text{m}^2$, while the injection current density for practical applications cannot be beyond $180\text{A}/\text{cm}^2$). Figure 4.3a and 4.3b show their band diagrams at $180 \text{ A}/\text{cm}^2$, while Figure 4.3c and 4.3d provide their carrier distribution at $180 \text{ A}/\text{cm}^2$. Due to the much higher mobility and lower effective mass of electrons than those of holes, electrons can overcome the potential barrier and can be distributed across the whole InGaN QW region without any great concerns as shown in Figure 4.3c and 4.3d. Of course, the electron concentration of n-type GaN is generally one or even two orders of magnitude higher than that of p-type GaN. Previous studies have shown that a semi-polar LED exhibits an opposite polarity in comparison with c-plane LEDs¹³. Therefore the polarization induced electric field in InGaN MQWs leads to an additional energy barrier for holes. As expected the crystal orientation plays a significant role in hole transport and then hole concentration distribution.

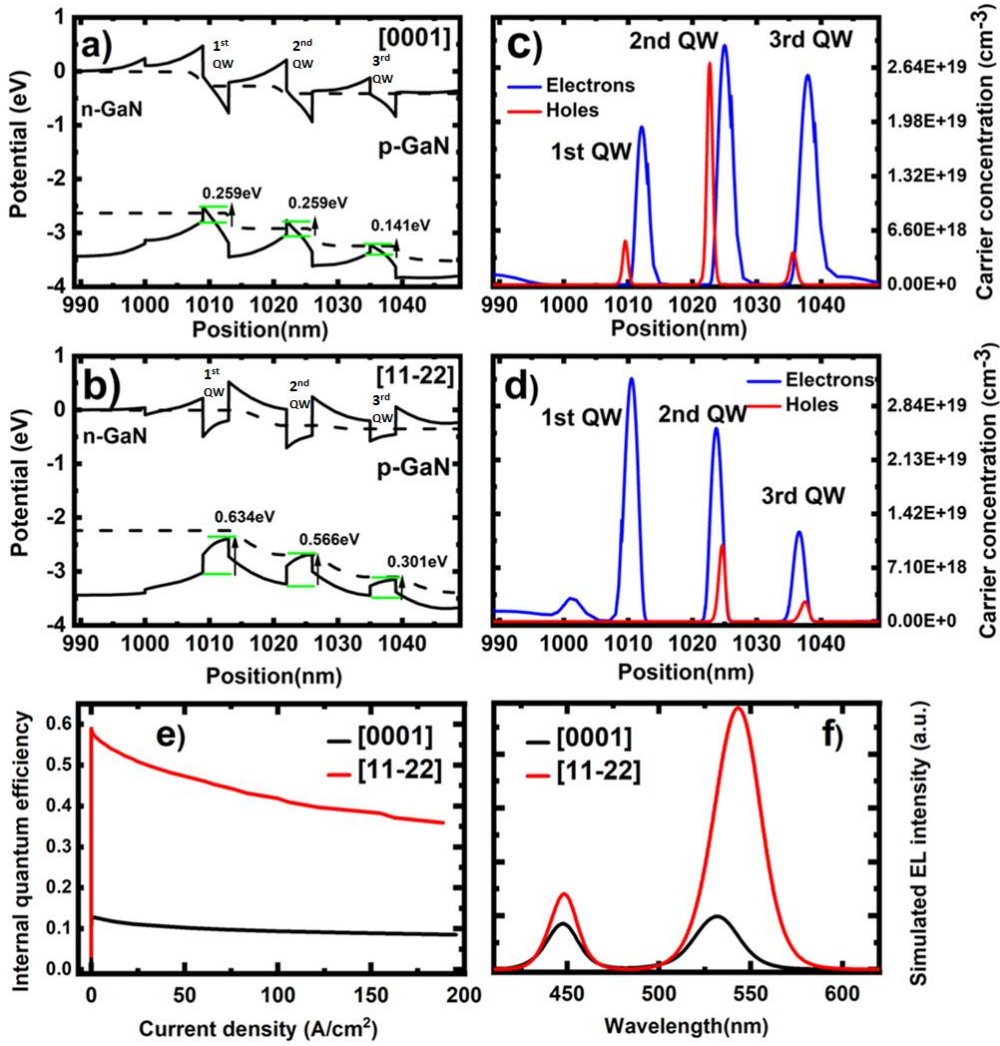


Figure 4.3 Simulated band diagrams of (a) c-plane LED and (b) (11-22) LED; and their corresponding carrier concentration in the InGaN quantum well region of (c) c-plane LED at 180 A/cm², 9.6 V and (d) (11-22) LED at 180 A/cm² 9.3V, (e) IQE of c-plane LED and (11-22) LED f) simulated EL intensity of c-plane and (11-22) LEDs

Figure 4.3a and 4.3b show an enhanced barrier potential for holes in the semi-polar (11-22) LED in comparison with the c-plane counterpart. In detail, the potential barrier for holes between the 1st grown InGaN QW and the 3rd grown InGaN QW is significantly enhanced compared with the c-plane counterpart as a result of reversed polarization induced electrical field, suppressing the injection of holes into the 1st

grown QW thus reducing the holes captured in the 1st InGaN QW. Therefore, the hole concentration in the 1st grown QW of the semi-polar LED is much less than that of its c-plane counterpart as shown in Figure 4.3c and 4.3d.

Figure 4.3c and 4.3d also show that the hole concentration in the 3rd grown QW for both cases is comparable, but is much lower than that in the 2nd grown QW. This case is even worse for the c-plane counterpart as a result of strong QCSE. The large polarization exhibited in the c-plane counterpart inevitably leads to the spatial separation of the electron-hole wavefunction and thus quantum efficiency is reduced. Figure 4.3e depicts the calculated internal quantum efficiency of both c-plane and semipolar LED as a function of current density. C-plane LED exhibits much lower IQE than semipolar (~5x less) as expected, leading to a lower EL intensity as emitted from the active region, depicted in Figure 4.3f.

4.4 GaN spacer and design of new structure

In order to take advantage of utilizing semi-polar LEDs and also enhance the confinement for the holes in the 3rd grown InGaN QW, a new structure has been proposed. A thin GaN spacer is introduced, namely, a thin GaN barrier is introduced prior to the blue SQW. Figure 4.4a shows a schematic of the semi-polar LED with a GaN spacer, 4.4b shows the calculated distribution of hole concentration across the 2nd and the 3rd grown QWs. With increasing GaN spacer thickness, the carrier concentration in the 3rd grown QW increases significantly, while the hole concentration in the 2nd grown QW decreases quickly. Considering the overall hole concentration in both the 2nd and 3rd grown QWs, the optimized thickness of the GaN spacer has been determined to be 2 nm. Figure 4.4c shows the simulated electro-

luminescence (EL) spectra as a function of GaN spacer thickness. In terms of the relative EL intensity of the emission from the 2nd grown QW (yellow) and the 3rd grown QW (blue), the optimized LED is the one with a 2 nm GaN spacer.

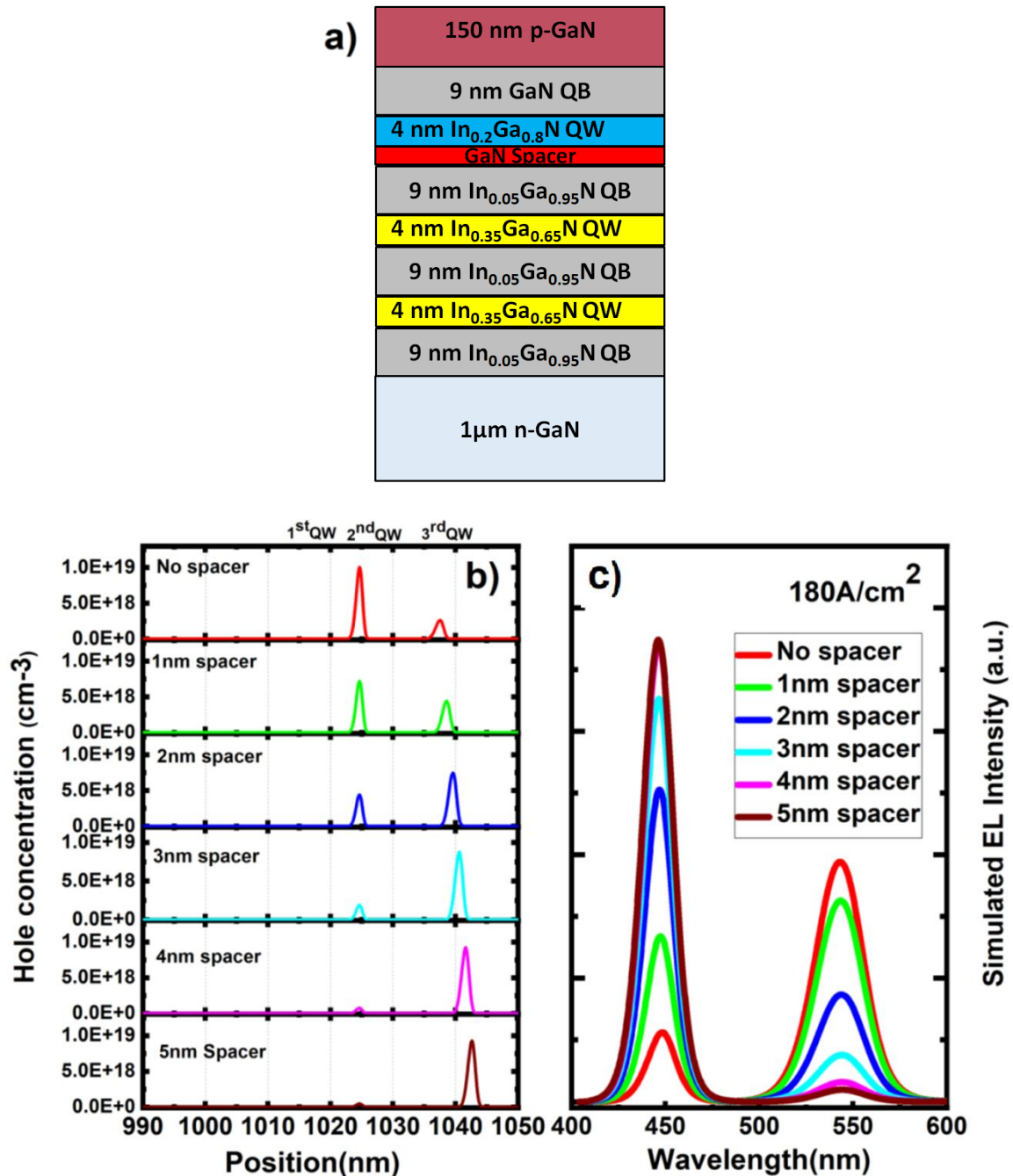


Figure 4.4 Calculated distribution of hole concentration across the InGaN quantum well region as a function of GaN spacer thickness; (b) Simulated electro-luminescence (EL) spectra as a function of GaN spacer thickness

4.5 Growth order of dual-color (11-22) semipolar LEDs

Two different kinds of LED structures, labeled as Sample A and Sample B, have been designed where in both cases the LEDs consist of an InGaN SQW for blue emission and two pairs of InGaN MQWs for yellow emission. However, the growth order of the blue SQW and the yellow MQWs is different. For Sample A, the blue SQW is grown first, followed by the yellow MQWs, while for Sample B the yellow MQWs are grown first and then the blue SQW afterwards.

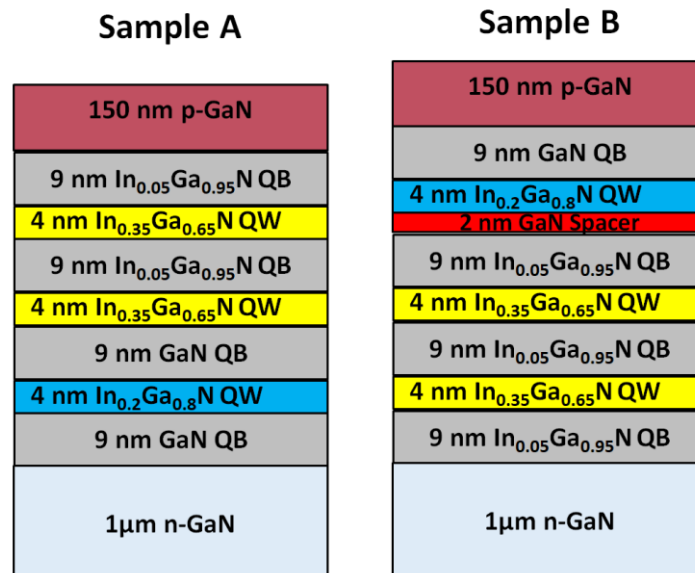


Figure 4.5 Schematics of Sample A and Sample B

Figure 4.5 illustrates schematically the structures of Sample A and Sample B. Both LEDs consist of a 1 μm n-type GaN layer, then an active region comprising a blue InGaN SQW with low indium content and 2 pairs of yellow InGaN MQWs with high indium content, and finally a 150 nm p-type GaN layer. Figure 4.5 also provides the detailed parameters including indium composition and the thicknesses of quantum wells and barriers. For Sample B, an extra GaN spacer with a thickness of 2 nm is

introduced prior to the growth of the blue SQW, in order to enhance the confinement for the 3rd grown InGaN QW as discussed above.

Band diagrams and hole distribution have been performed on Sample A and B as a function of injection current density of up to 180 A/cm². Figure 4.6a and 4.6b show the simulated band diagrams at 180 A/cm², while Figure 4.6c and 4.6d correspond their simulated hole concentration distribution and EL intensities respectively.

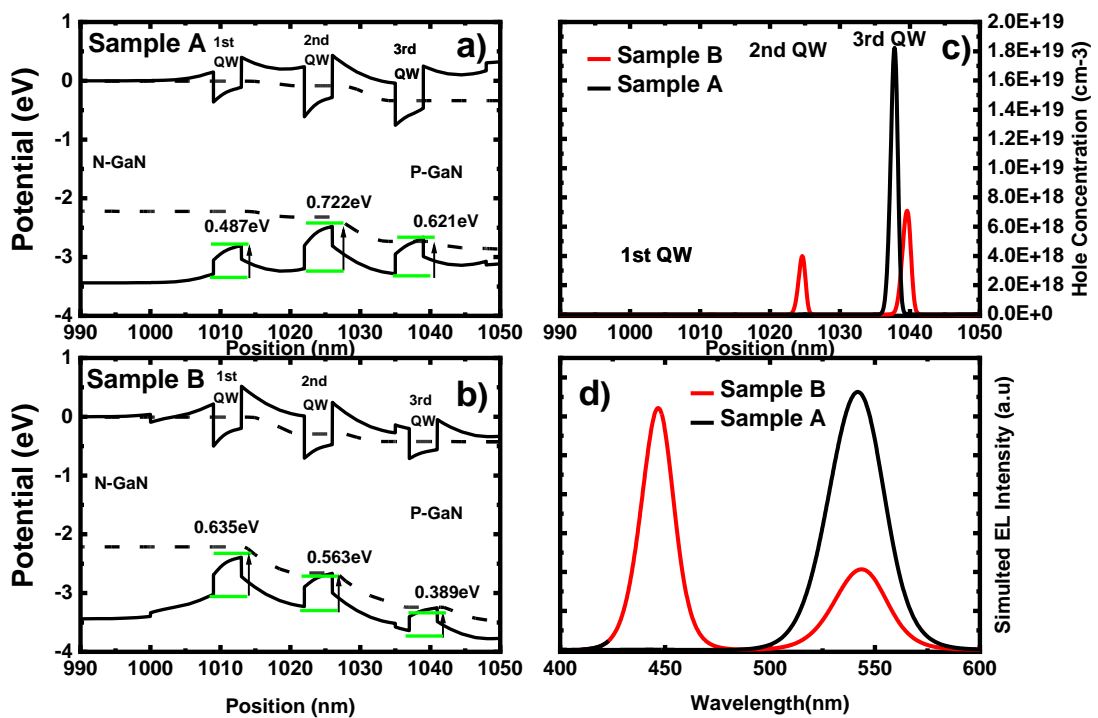


Figure 4.6 Simulated band diagrams for (a) Sample A and (b) Sample B, (c) simulated hole concentration in the InGaN quantum well region of Sample A and Sample B (d) Simulated EL intensities of Sample A and Sample B at 180 A/cm², 9.1 V and 180 A/cm² 9.5 V respectively

If a blue SQW is grown first followed by the yellow InGaN QWs (i.e., Sample A) as shown in Figure 4.6a, the 3rd grown QW exhibits an energy difference of 0.621eV between the quantum well and quantum barrier for holes due to high indium

composition in the yellow QWs. As a result, it is difficult for holes to escape from the 3rd grown InGaN QW and thus remain trapped in the 3rd grown InGaN QW (i.e., yellow emission). Therefore, the hole concentration in the 2nd grown QW is extremely low as shown in Figure 4.6c. In contrast, for Sample B, where the yellow quantum wells are grown first followed by the blue SQW with a 2nm GaN spacer as discussed above, the energy barrier for the 3rd grown QW has significantly dropped by 0.232eV compared with Sample A as a result of the low indium composition in the 3rd grown QW (i.e., for blue). Due to the reduction in energy barrier for holes, it becomes possible for holes to escape from the 3rd grown QW to the 2nd grown QW, and thus the hole concentration in the 2nd grown QW increases substantially as shown in Figure 4.6c. Therefore, in this case, dual colour emission can be possibly achieved with peak wavelengths located at 450nm and 545nm.

4.6 Design of tri-chromatic (11-22) semipolar LED

A dual-colour LEDs has been achieved by utilizing the Sample B structure, where InGaN yellow QWs have to be firstly grown, followed by the growth of a blue single InGaN quantum well. A thin GaN spacer of 2nm has been introduced prior to the blue SQW to effectively confine holes in the 3rd QW. Nevertheless, the potential barrier for the 2nd InGaN QW hinders the transportation of holes to the 1st grown QW, leading to very low hole concentration in the 1st InGaN QW. In this section, two major factors, such as indium content and barrier thickness, will be examined, aiming to achieving hole capture in the 1st QW and to increase the hole concentration in the 1st QW and finally to achieve a tri-chromatic emission. By varying the indium composition of the QW, the emission wavelength can be tuned. Subsequently the potential barrier of the

QW will be changed and thus affecting the transportation of holes. By taking as a reference structure of Sample B, a systematic study has been conducted in order to examine the effect of the indium composition of the QWs and the barrier thicknesses on the hole transport across the active region. Due to the higher mobility and lower mass, electrons can transport easily across the active region as mentioned above. Therefore, the emission contributed from each QW primarily depends on hole transport.

The initial consideration was to reduce the indium composition of the 3rd QW in order to reduce the potential barrier for the 3rd QW and simultaneously shift the short wavelength emission to higher energy. Figure 4.7a and 4.7b illustrates the band diagrams at $180\text{A}/\text{cm}^2$ for Sample B and Sample C with reduced indium content of the 3rd QW. Figure 4.7c shows the hole distribution across the QWs. By reducing the indium composition to 18% the hole concentration in the 2nd quantum well increases from $4 \times 10^{18}/\text{cm}^3$ to $5.9 \times 10^{18}/\text{cm}^3$ while for the 3rd QW holes concentration decreases from $7.09 \times 10^{18}/\text{cm}^3$ to $3.9 \times 10^{18}/\text{cm}^3$. The hole concentration of the 1st QW was lowered by 3 order of magnitude in the range of $10^{15}/\text{cm}^3$. With the 2nd QW exhibiting the highest hole accumulation, the emission from the second QW is enhanced and become comparable with the emission from the shorter QW as depicted in Figure 4.7d while the emission from the blue QW is blue-shifted by 13 nm, exhibiting a center wavelength at 437nm.

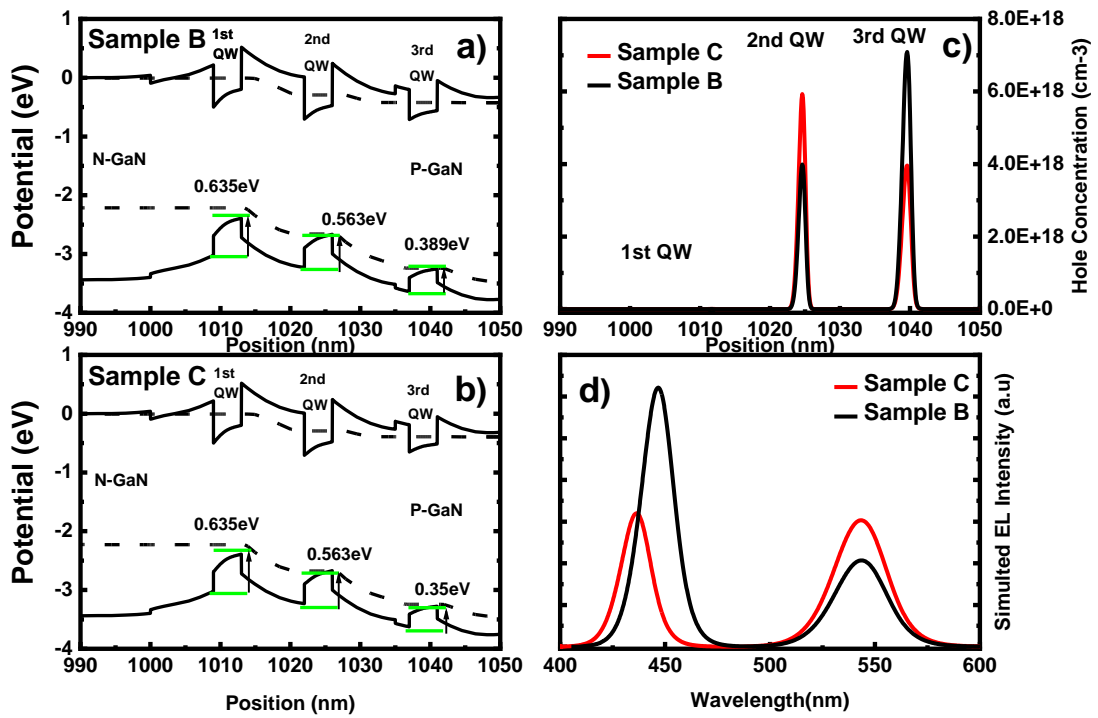


Figure 4.7 Simulated band diagrams for (a) Sample B and (b) Sample C, (c) simulated hole concentration in the InGaN quantum well region of Sample B and Sample C (d) Simulated EL intensities of Sample B and Sample C at 180 A/cm^2 , 9.5 V and 180 A/cm^2 , 9.4 V respectively

In order to move towards longer wavelength emission, the indium composition for the 1st and 2nd QW has been set to 36%, labeled as Sample D, resulting in a 5nm redshift of the yellow emission centered at 550nm. Figure 4.8 depict the simulation outcomes of the band diagram, hole concentration and EL emission for Sample C and Sample D, respectively. The potential barrier for the holes in the 2nd QW shows a 7 meV increase, leading to a small increase in hole concentration in the 2nd QW and thus a slight reduction in the number of holes captured by the 3rd QW. Specifically, the hole concentration in the 2nd QW is increased by $7.5 \times 10^{17} / \text{cm}^3$ while the hole concentration in the 3rd QW is reduced by $5 \times 10^{17} / \text{cm}^3$. This further enhances the

yellow emission. The contribution from the 1st QW is still negligible since the hole concentration is very low.

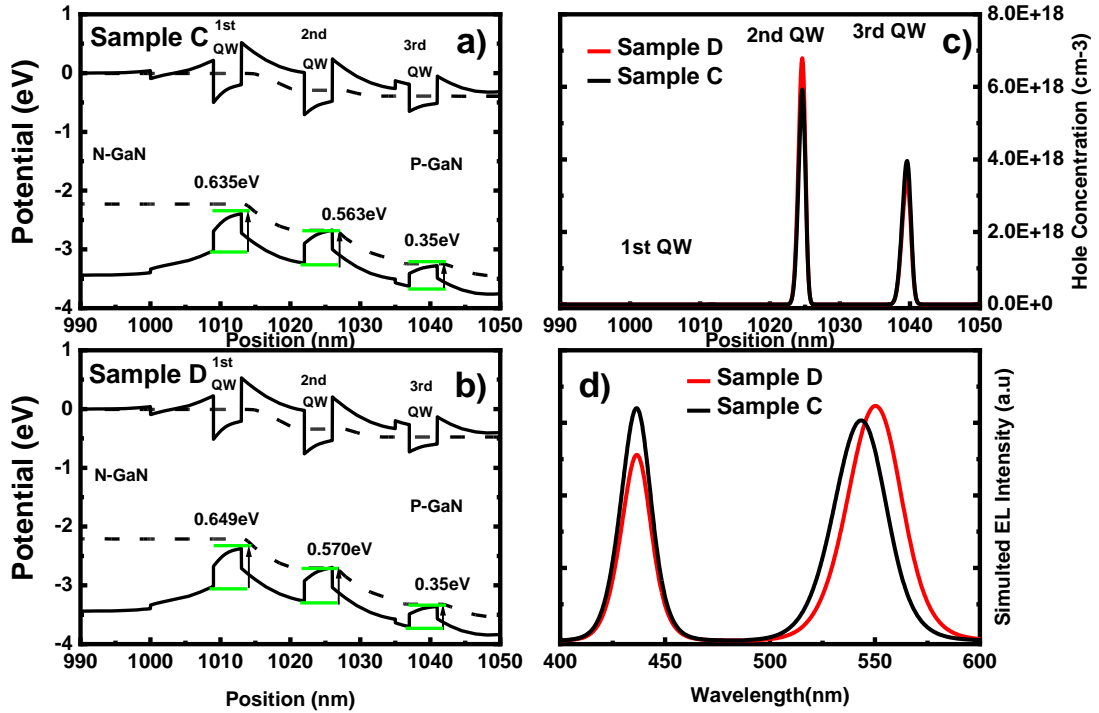


Figure 4.8 Simulated band diagrams for (a) Sample C and (b) Sample D, (c) simulated hole concentration in the InGaN quantum well region of Sample C and Sample D (d) Simulated EL intensities of Sample C and Sample D at 180 A/cm², 9.4V and 180 A/cm², 9.8V respectively

The next step was to examine the effect of the thickness of the barrier between the two yellows QWs. Figure 4.9 depicts the band diagram as a function of the barrier thicknesses at an injection current density of 180A/cm². Figure 4.10a illustrates the hole concentrations in the 1st, 2nd, and 3rd quantum wells as a function of the barrier thickness at 180A/cm². Figure 4.10b illustrates a zoom-in for the hole concentration in the 1st QW. It can be noted that the hole concentration in the 1st QW increases as the

barrier thickness decreases. In particular, when the barrier thickness is 9nm the hole concentration in the 1st QW is $8.03 \times 10^{15} / \text{cm}^3$. When the barrier thickness is further reduced to 4 nm, the hole accumulation is increased by two order of magnitude, reaching $6.96 \times 10^{17} / \text{cm}^3$.

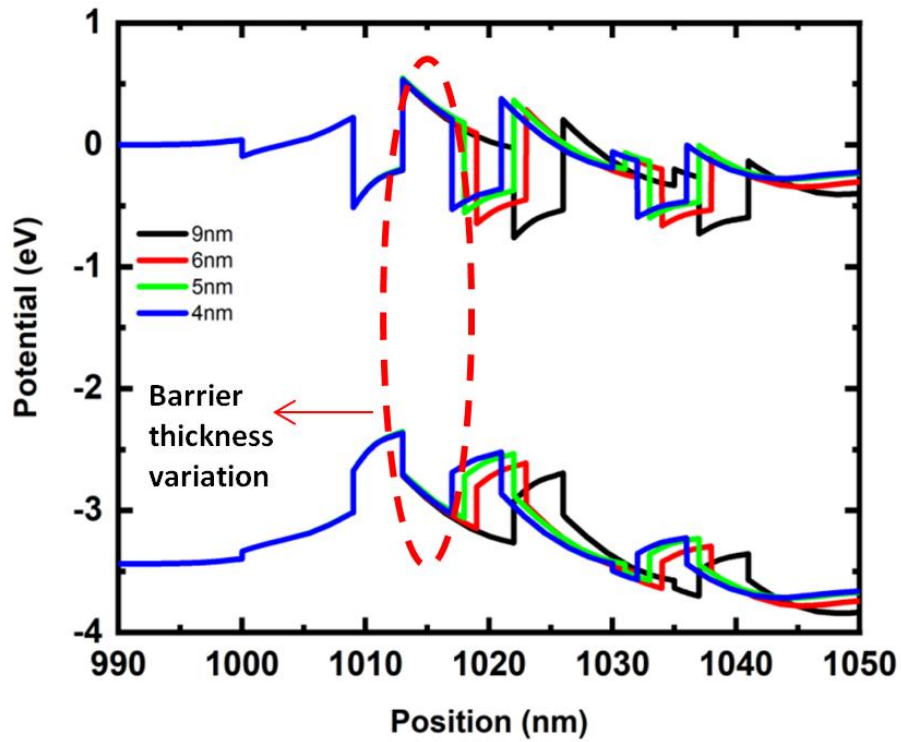


Figure 4.9 Band diagram as a function of the barrier thicknesses

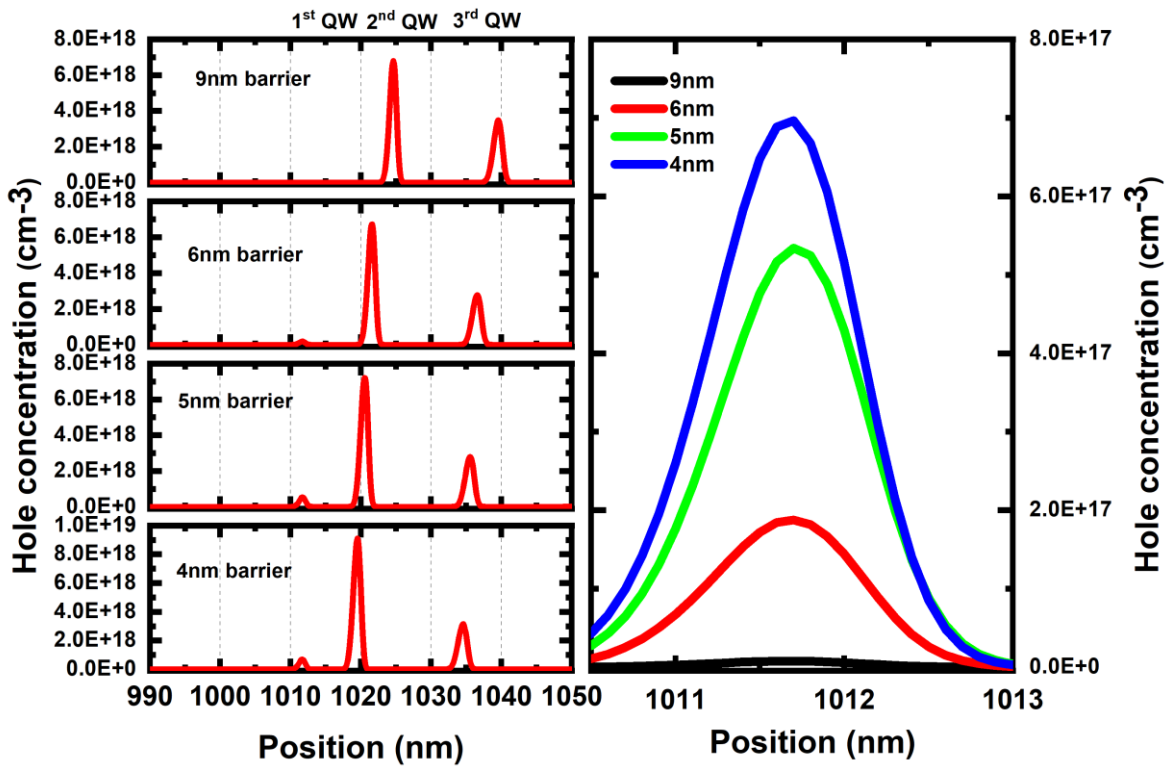


Figure 4.10 Calculated distribution of hole concentration across the InGaN quantum well region as a function of barrier thickness located between the long wavelength QWs and (b) magnified image of hole concentration of the 1st grown QW

Since a significantly high density of holes in the 1st QWs can be achieved by using a 4nm barrier thickness, the next step is to maintain this 4 nm barrier thickness but to increase the indium composition for the 1st QW.

The indium content of the 1st QW is set to 40%, and is labeled as Sample E. Figure 4.11a depicts the band diagram of Sample E at 180A/cm², while Figure 4.11c shows the corresponding hole distribution, and Figure 4.11d the corresponding simulated EL. It is worth noting that Figure 4.11d shows an extra shoulder at the longer wavelength region for Sample E. However, the hole concentration is still not uniform, and the majority of holes are captured by the deep 2nd QW corresponding dominant yellow

emission. In order to separate the emission at 550 nm and the shoulder at 580nm and also simultaneously reduce the emission coming from the 2nd QW, the indium content of the 2nd QW is reduced to 32%, labeled as Sample F. The band diagram, hole concentration distribution and simulated EL spectrum have been provided in Figure 4.11a, 4.11b, 4.11c and 4.11d as well, showing that Sample F exhibits a 3 distinct peaks located at 437nm, 523nm and 582nm with a fairly even distribution of the hole concentrations in the 1st 2nd and 3rd QW of $3.5 \times 10^{18}/\text{cm}^3$, $2.3 \times 10^{18}/\text{cm}^3$ and $4.1 \times 10^{18}/\text{cm}^3$, respectively.

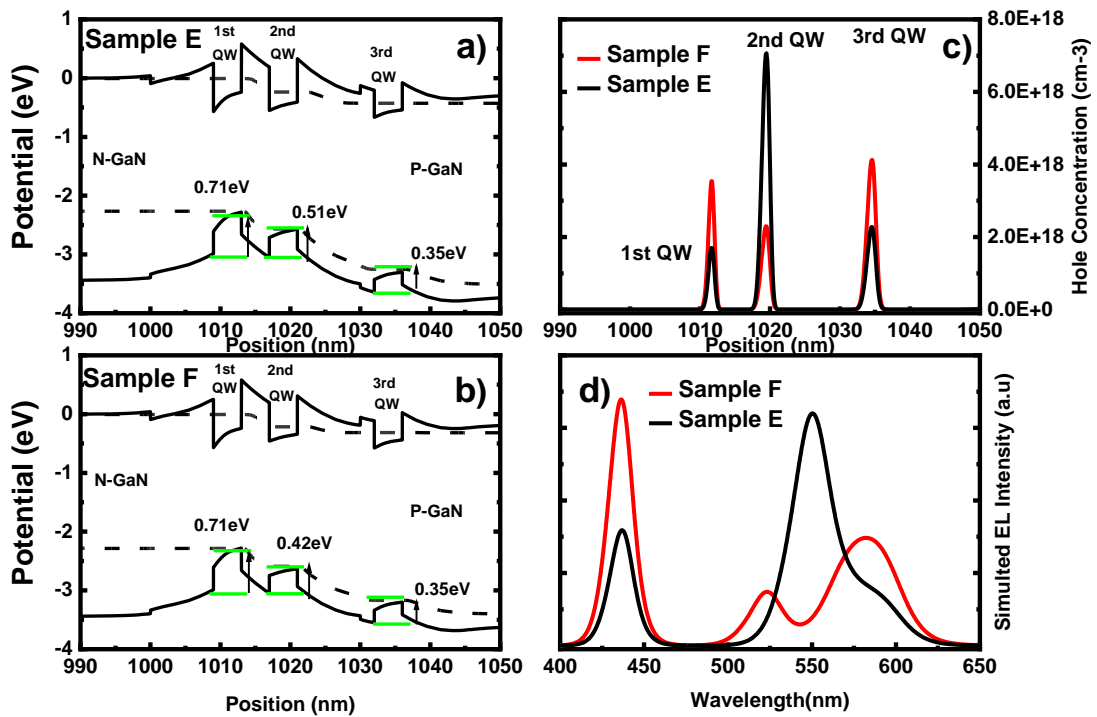


Figure 4.11 Simulated band diagrams for (a) Sample E and (b) Sample F, (c) simulated hole concentration in the InGaN quantum well region of Sample E and Sample F, (d) Simulated EL intensities of Sample E and Sample F at $180 \text{ A}/\text{cm}^2$, 9.3V and $180 \text{ A}/\text{cm}^2$, 9.7V respectively

Figure 4.12 shows the CIE chromaticity coordinates for Sample E and Sample F both of which exhibit three colour emissions. Sample E has (0,32, 0,48) chromaticity coordinates and 13.8 CRI whereas Sample F exhibit better spectral distribution with chromaticity coordinates of (0,32, 0,28) and CRI of 47.4.

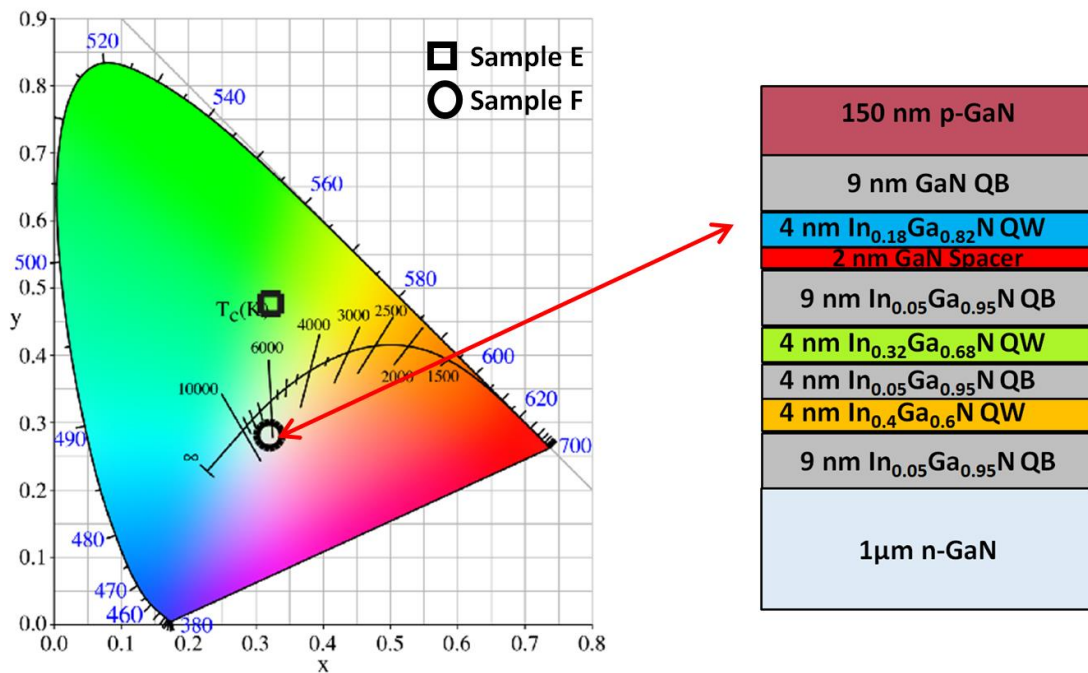


Figure 4.12 (a) CIE chromaticity coordinates for Sample E and Sample F and (b) schematic illustration of Sample F

4.7 Summary

In summary, a systematic study has been performed on a dual colour LED on a semipolar substrate and its c-plane counterpart in order to examine the effects of crystal orientation on carrier transport, in particular, hole transport issues. Two different kind of structures labeled as Sample A and sample B have been designed, demonstrating that the growth order of the InGaN quantum wells with different

emission wavelength plays a vital role in achieving a dual-colour emission. An extra thin GaN spacer (for Sample B) is also crucial. Furthermore, in order to achieve a tri-chromatic emission LED, further studies considering the indium content in the quantum wells and the barrier thickness have been investigated, leading to an even distribution of the holes concentration in the three quantum wells, and thus achieving three color emissions in a single chip.

References

1. Huang, C. F., Lu, C. F., Tang, T. Y., Huang, J. J. & Yang, C. C., Phosphor-free white-light light-emitting diode of weakly carrier-density-dependent spectrum with prestrained growth of InGaN/GaN quantum wells. *Appl. Phys. Lett.* **90**, (2007).
2. Qi, Y. D., Liang, H., Tang, W., Lu, Z. D. & Lau, K. M., Dual wavelength InGaN/GaN multi-quantum well LEDs grown by metalorganic vapor phase epitaxy. in *Journal of Crystal Growth* **272**, 333–340 (North-Holland, 2004).
3. Li, Y. L., Gessmann, T., Schubert, E. F. & Sheu, J. K., Carrier dynamics in nitride-based light-emitting p-n junction diodes with two active regions emitting at different wavelengths. *J. Appl. Phys.* **94**, 2167–2172 (2003).
4. Damilano, B., Grandjean, N., Pernot, C. & Massies, J., Monolithic white light emitting diodes based on InGaN/GaN multiple-quantum wells. *Japanese Journal of Applied Physics, Part 2: Letters* **40**, L918 (2001).
5. Chen, C. H. *et al.*, Nitride-based cascade near white light-emitting diodes. *IEEE Photonics Technol. Lett.* **14**, 908–910 (2002).
6. El-Masry, N. A., Piner, E. L., Liu, S. X. & Bedair, S. M., Phase separation in InGaN grown by metalorganic chemical vapor deposition. *Appl. Phys. Lett.* **72**, 40–42 (1998).
7. Tokuda, T., Wakahara, A., Noda, S. & Sasaki, A., Growth characteristics of GaInN on (0 0 0 1)sapphire by plasma-excited organometallic vapor phase epitaxy. *J. Cryst. Growth* **187**, 178–184 (1998).
8. Zhao, Y. *et al.*, Indium incorporation and emission properties of nonpolar and semipolar InGaN quantum wells. *Appl. Phys. Lett.* **100**, 201108 (2012).

9. Strittmatter, A. *et al.*, Semi-polar nitride surfaces and heterostructures. *Phys. status solidi* **248**, 561–573 (2011).
10. Sizov, D. S. *et al.*, Carrier transport in InGaN MQWs of aquamarine- and green-laser diodes. *IEEE J. Sel. Top. Quantum Electron.* **17**, 1390–1401 (2011).
11. Bulashevich, K. A., Mymrin, V. F., Karpov, S. Y., Zhmakin, I. A. & Zhmakin, A. I., Simulation of visible and ultra-violet group-III nitride light emitting diodes. *J. Comput. Phys.* **213**, 214–238 (2006).
12. Mymrin, V. F. *et al.*, Modelling study of MQW LED operation. *Phys. status solidi* **2**, 2928–2931 (2005).
13. Kawaguchi, Y. *et al.*, Influence of polarity on carrier transport in semipolar (20-21) and (20-2-1) multiple-quantum-well light-emitting diodes. *Appl. Phys. Lett.* **100**, 231110 (2012).

Chapter 5

Fabrication of monolithically integrated white light LEDs on (11-22) semi-polar GaN templates

Monolithically integrated white light LEDs have been grown on (11-22) semi-polar GaN template by using two different approaches. The first approach relies on vertically stacked QWs in an active region. Two kinds of LEDs namely Sample A and Sample B have been grown according to the simulation outcomes performed in Chapter 4. Experimental and simulation results are in a good agreement, confirming that the growth order of the blue and yellow QWs and the growth of an extra thin GaN spacer prior to the blue QW are crucial for achieving dual-colour emission. Finally, dual-colour LEDs have been experimentally demonstrated. The second approach is based on down-conversion method, where the device structure comprises an electrically injected blue LED and an extra yellow MQW structure grown on the top acting as a down conversion layer, demonstrating the idea is working although further substantial work needs to be carried out in the future.

5.1 Introduction

So far, the “blue LED + yellow phosphor” approach is maintaining its strong lead for the fabrication of white LEDs^{1,2}. The performance of such white LEDs has almost approached its limit, but is still far from the requirements described in the US road map for developing SSL³. Furthermore, the phosphor-converted approach suffers from numerous drawbacks, such as down-conversion losses, optical losses due to backscattering, heat related effects and the degradation of yellow phosphor as a result of its long-term exposure^{4,5,6}. In addition, an increasing demand on Li-Fi applications requires a white LED with an ultra-fast response. Current blue LEDs on c-plane substrates suffer from a long carrier recombination lifetime as a result of QCSE, typically on a scale of a few to 10 nanoseconds for blue emission and ~100 nanoseconds for green emission⁷. Phosphors generally exhibit even a longer response time, typically on a microsecond scale. In contrast, semi-polar, particularly the (11–22) InGaN quantum wells exhibit a much shorter carrier recombination lifetime, typically hundreds of picoseconds for blue emission⁸.

In order to address these great challenges, a number of approaches have been proposed. One of the most direct approach of a monolithic scheme can be realized by the usage of InGaN/GaN quantum wells with different emission wavelengths located in the active region of an LED structure^{9,10,11,12,13}. Nevertheless, this particular approach relies on vertically stacked InGaN/GaN MQWs within the active region and exhibits non-uniform carrier transport issues. One of the major issues which causes the non-uniform injection of electrical carriers into the quantum wells can be attributed to the low migration speed of holes which is approximately an order of

magnitude lower, compared with the mobility of electrons¹⁴. Moreover the uneven carrier transport issue is more pronounced in LEDs grown on c-plane orientation where high piezoelectric fields exhibit as presented in Chapter 4. Many approaches have been conducted to overcome this issue of the uneven carrier distribution,

Park et al. utilizes a selective area approach for the formation of laterally distributed QWs on c-plane sapphire. The non-uniform injection of electrical carriers which exhibits in vertically allocated QWs can be overcome by the parallel carrier injection of laterally distributed QWs¹⁵. However this approach requires complicated and several step of fabrication and growth and secondly the LED was grown on c-plane sapphire which poses a number of fundamental issues which decrease the optical efficiency as aforementioned.

A down-conversion method was also developed in order to overcome the carrier transport issues. Damilano et al. reported a device which an electrically injected blue LED is grown on top of green-yellow emitting QWs. The green-yellow QWs are optically pumped and act as a light converter¹⁶. The sample was grown on c-plane sapphire and consisted of 20 periods green-yellow emitting InGaN /GaN QWs grown by MOCVD. In order to avoid high temperature which is required for growing blue QWs by MOCVD, the blue LED structure was grown by using molecular beam epitaxy MBE, which allows the growth of blue QWs at lower temperatures. Results have shown that the final colour of LED depended on both blue QW wavelength and the green-yellow absorption.

However, the above approaches were grown on c-plane sapphire which exhibit many fundamental issues to overcome as mentioned before. The severe issues of polar

orientation c-plane (0001) would be mitigated or eliminated by the growth of III-nitrides hetero-structure device on semipolar or nonpolar direction where the electric field is partially or totally reduced.

Kowsz et al. reported a down conversion approach which utilizes a free-standing double-side-polished (DSP) (20-2-1)/(20-21) GaN substrate where an electrically injected blue LED is grown on (20-2-1) face of the DSP GaN substrate and optically pumped yellow QWs grown on the (20-21) face¹⁷. The device exhibited two peaks located at 440nm and 560nm. A drawback of this particular (20-21) semipolar plane orientation is the inefficiency for high indium incorporation. In order to overcome this issue, they have recently grown a new structure which utilized a p-i-n configuration which was used to create an electric field to shift the emission wavelength of one of the optically pumped QWs to longer wavelength. As in their previous attempt, electrically injected blue light LED was grown on the (20-2-1) face of free-standing DSP GaN and a light converter with longer wavelengths on the (20-21) face¹⁸. The main drawbacks of this approach are due to the complicated structure and the utilization of free-standing substrates which are limited to small sizes and exhibit high cost.

The (11-22) semi-polar surface not only reduces piezoelectric fields but also significantly favours indium incorporation into GaN, which is crucial for the growth of longer wavelength InGaN QWs with high indium content required for white LEDs¹⁹. Nevertheless one of the great challenges is the growth of high crystal quality of semipolar GaN on sapphire substrate. Although (11-22) semipolar GaN can be directly grown on m-plane sapphire, it typically exhibits high density of dislocations and high density of Basal Stacking faults (BSF). Recently, our group has demonstrated semi-

polar (11-22) InGaN LEDs with a wide spectral region of up to amber on our overgrown semi-polar GaN templates with significantly improved crystal quality, demonstrating high performance semi-polar LEDs²⁰.

In this work, monolithically integrated white light LEDs on semipolar 11-22 overgrown GaN, were obtained by two different methods. The first method follows one of the most direct routes for the fabrication of monolithic white LEDs which utilize InGaN MQWs with different emission wavelengths. This particular approach requires effective bandgap engineering in order to resolve carrier transport issues which such approach suffers. In principle, this approach not only is cost-effective but also matches the current growth and fabrication techniques for III-nitride optoelectronics. Based on simulations, performed in Chapter 4, two kinds of dual-colour LEDs with vertically stacked QWs were grown on our high quality semipolar (11-22) GaN templates to validate our idea. Simulations have shown that the growth order of the long wavelength and short wavelength is paramount of importance for the realization of a dual-colour LED. Furthermore the dual-colour LED can be obtained by growing a thin GaN spacer prior to the growth of the blue QW, which effectively balance the hole concentration of the blue and yellow quantum wells.

The second approach comprises a blue LED and an epitaxially grown light converter. An InGaN/InGaN blue LED is electrically injected generating blue photons, where a portion of them is absorbed by the green-yellow emitting QWs placed on the top. It is expected that the realization of white light would depend on the blue pumping wavelength and the absorption of the light converter. One of the advantages of down conversion approach is the fact that the high indium content QWs are optically pumped providing a better carrier distribution than in the case of electrically

injection. Under optical excitation, the carriers are distributed more evenly in each QW, resulting a lower carrier density in each QW. Moreover, the idea of growing the high indium InGaN QWs on the top of the p-n junction diode prevents the light converter to be exposed to high temperature during the growth of the blue QWs.

5.2 Monolithically integrated white light LED on (11-22) semipolar GaN template for white light emission by band engineering

Based on simulation performed in Chapter 4, two different kinds of LED structures, labeled as Sample A and Sample B, have been grown on our high quality semi-polar overgrown GaN, where in both cases the LEDs consist of an InGaN single quantum well (SQW) for blue emission and two pairs of InGaN MQWs for yellow emission. However, the growth order of the blue SQW and the yellow MQWs is different. For Sample A, the blue SQW is grown first, followed by the yellow MQWs, while for Sample B the yellow MQWs are grown first and then the blue SQW. In both cases, the growth conditions remained identical.

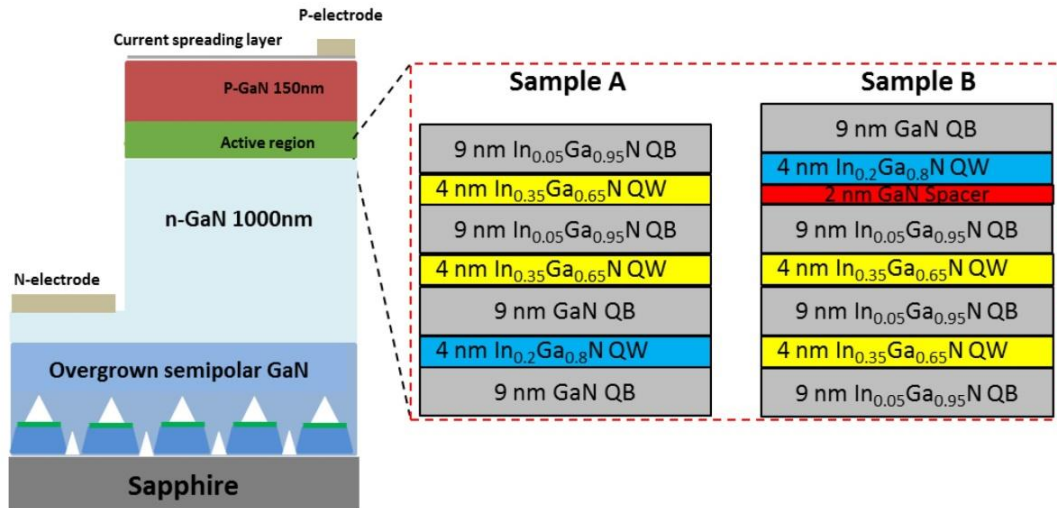


Figure 5.1 Schematics of Sample A and Sample B

Figure 5.1 illustrates schematically the structures of Sample A and Sample B. Both LEDs consist of a $1\mu\text{m}$ n-type GaN layer, then an active region comprising a blue InGaN SQW with low indium content and 2 pairs of yellow InGaN MQWs with high indium content, and finally a 150nm p-type GaN layer. Figure 5.1 also provides the detailed parameters including indium composition and the thicknesses of quantum wells and barriers as used in simulations in Chapter 4. For Sample B, an extra GaN spacer with a thickness of 2 nm is introduced prior to the growth of the blue SQW, in order to enhance the confinement for the 3rd grown InGaN QW. Sample A and Sample B were grown on our overgrown semi-polar (11–22) GaN with high crystal quality, where regularly arrayed (11–22) GaN micro-rods with a diameter of $4\mu\text{m}$ used as a template for overgrowth are fabricated by means of using a standard photolithography mask patterning technique and then dry etching processes.

5.3 Methods

High quality (11–22) semi-polar GaN templates on sapphire are used for the MOVPE growth of multi-colour LED structures, where the dislocation density and the basal stacking fault density of the (11–22) semi-polar GaN templates are typically $2.0 \times 10^8 \text{ cm}^{-2}$ and $2.8 \times 10^4 \text{ cm}^{-1}$, respectively. After the templates are subjected to an initial annealing process under hydrogen ambient at a high temperature, a 400 nm undoped GaN layer is grown, which is followed by a 1 μm n-type GaN layer, then an active region comprising a blue InGaN SQW with low indium content and 2 pairs of yellow InGaN MQWs with high indium content, and finally a 150nm p-type GaN layer.

Before the fabrication of LED, samples were subjected to post annealing treatment by using RTA in order to activate the p-type layer. Post annealing temperature in N_2 ambient was kept at 675°C for 20 minutes. A standard lithography technique and dry-etching processes have been used to fabricate LED chips with a standard size of $330 \times 330 \mu\text{m}^2$. A 7nm/7nm Ni/Au alloy was deposited and then annealed by rapid thermal annealing as transparent p-type contact. The n-type contact was formed on n-type GaN by depositing a Ti/Al/Ti/Au alloy. Ti/Au was deposited as a pad electrode on both p-type and n-type contact.

5.4 Results and discussion

5.4.1 Photoluminescence measurements

Photoluminescence measurements were conducted on the as grown samples by using a 375nm laser diode as an excitation source at room temperature. A Horiba SPEX 500M monochromator was used to disperse the emission and detected by an air-cooled charge-couple device (CCD).

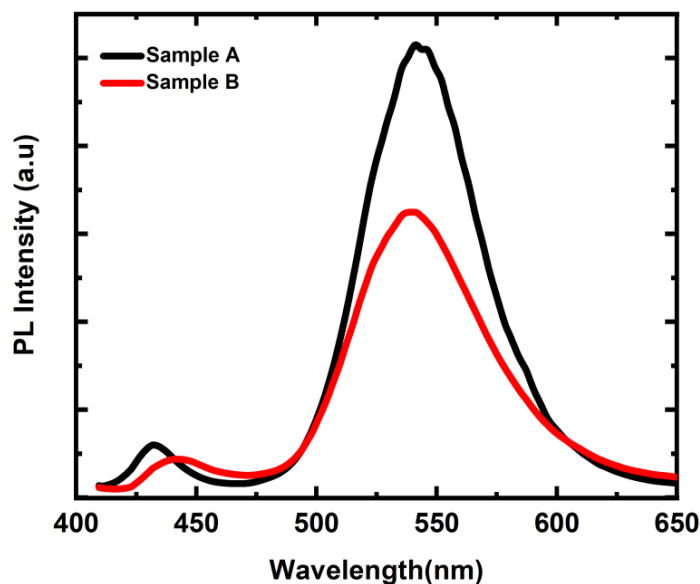


Figure 5.2 Photoluminescence spectra of the as grown Sample A and Sample B

Figure 5.2 shows the emission spectra of both as-grown structures of Sample A and Sample B indicating two clear emission peaks, in the blue and yellow region. A dominant yellow emission at center wavelength of 540nm exhibits in both as grown samples indicating a strong emission from the 2 pairs of yellow quantum wells. Although the growth conditions of both sample are identical, Sample B exhibit a slight red shift on blue peak (~7nm). In particular, Sample A exhibit a blue peak center at

434nm whereas Sample B exhibits a blue peak center at 441nm. This might attribute to the different strain between of blue QW with and without the GaN spacer.

5.4.2 Electroluminescence measurements

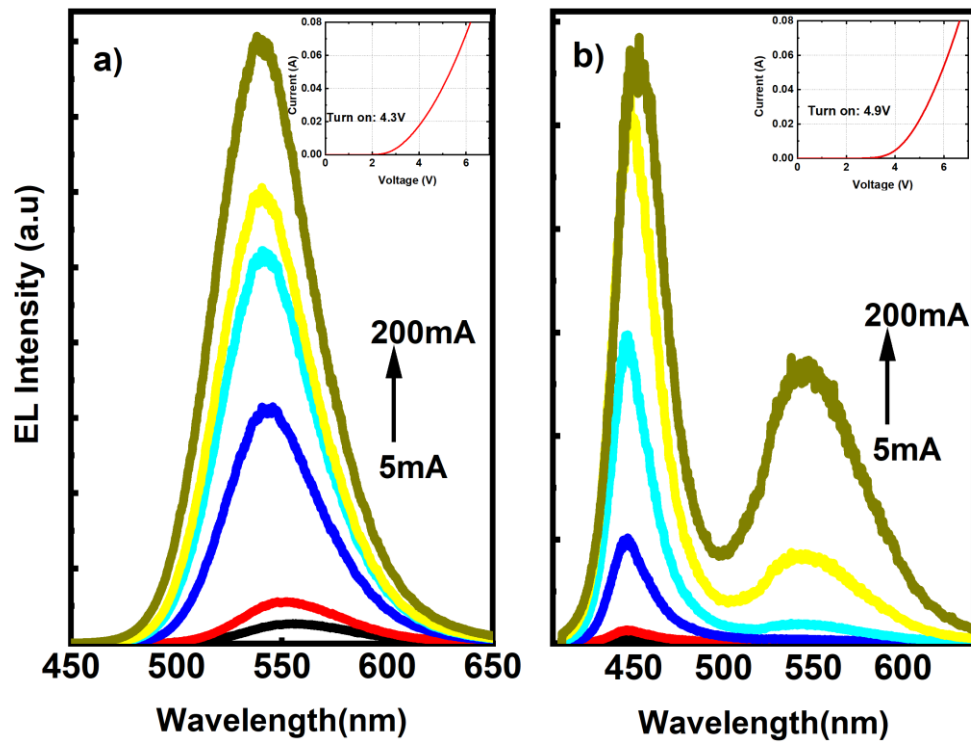


Figure 5.3 EL spectra measured at different injection currents for (a) Sample A and (b) Sample B. The insets show the IV plots of Sample A and Sample B

Electroluminescence (EL) measurements were carried out at injection currents of up to 200mA. Figure 5.3a and 5.3b shows the EL spectrum, of Sample A and Sample B whereas the inset figures show typical IV plots for both devices respectively. The forward voltages at injection current of 20 mA are 4.3V and 4.8V for Sample A and Sample B respectively while Sample A exhibits 32.1 Ω series resistance and Sample B exhibits 30 Ω series resistance. Sample A exhibits a single peak emission under all

driving currents whereas the dual emission can be solely achieved with Sample B structure where the blue QW is grown after the growth of the yellow QWs. In addition Sample B presents a gradual change in the two emission bands as the current increases from 5mA to 200mA. A dominant blue emission exhibits under the injection current range up to 50mA. As the current further increases up to 200mA the intensity of the yellow peak is gradually increasing, indicating that a greatest number of carriers are capture by the longer wavelength QWs. A comparison between of the simulated EL which was performed in Chapter 4 and the experimental EL at 200mA injection current is depicted in Figure 5.4.

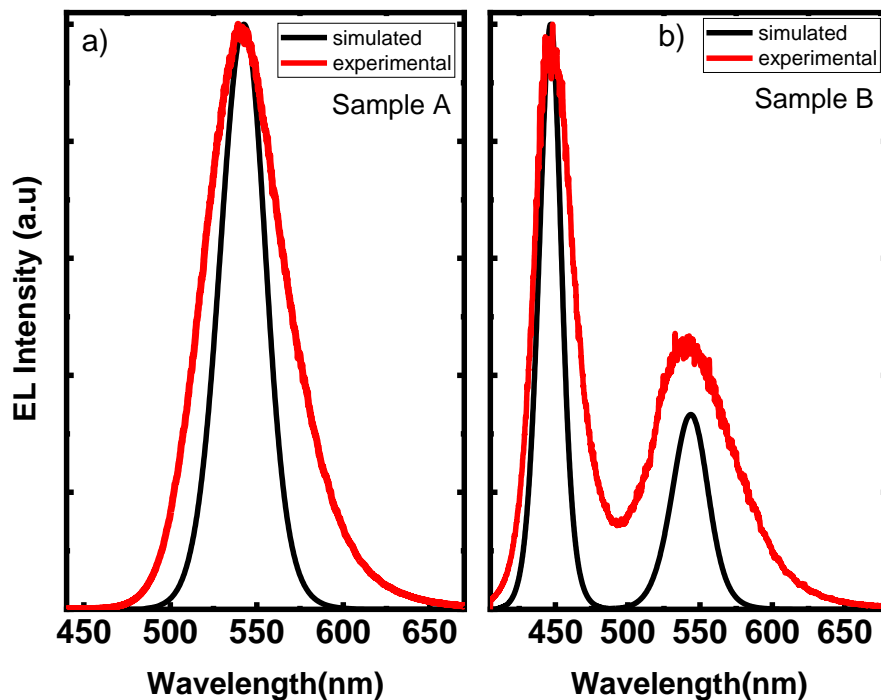


Figure 5.4 Simulated and experimental EL for (a) Sample A and (b) Sample B at 200mA.

Figure 5.4a and 5.4b illustrate the simulated and experimental EL spectra of Sample A and Sample B at 200mA. The simulated and experimental EL spectra are in very good

agreement, indicating that the hole transport is vital of importance for the LED performance. For instance, the simulated and experimental EL spectra for Sample A demonstrates a single peak center at 545nm, indicating that emission occurs from the deep QW adjacent to p-GaN, whereas Sample B exhibits a dual emission peak, center at 450nm and 545nm, indicating that holes manage to overcome the barrier of the shallow QW adjacent to the p-GaN as predicted in the simulation results in Chapter 4.

The broadening of the experimental spectra can be attributed to alloy broadening effect from the fluctuation of the indium composition. During growth, the indium incorporation in a QW structure may lead to indium segregation causing the broadening of the spectrum²¹.

Figure 5.5a and b show a series of EL images under the current injection range of 5mA to 200mA, demonstrating the single and dual colour emission of Sample A and Sample B respectively. Figure 5.5c illustrates the Commission Internationale de l'Eclairage (CIE) x,y chromaticity diagram which indicates the chromaticity coordinates of Sample B as a function of current. Moreover, a shift towards yellow side can be observed as the current increases, indicating the enhancement of the emission from the deep QWs. Particularly the chromaticity coordinates at 5mA are (0.16,0.11) whereas at 200mA moves to (0.23,0.27).

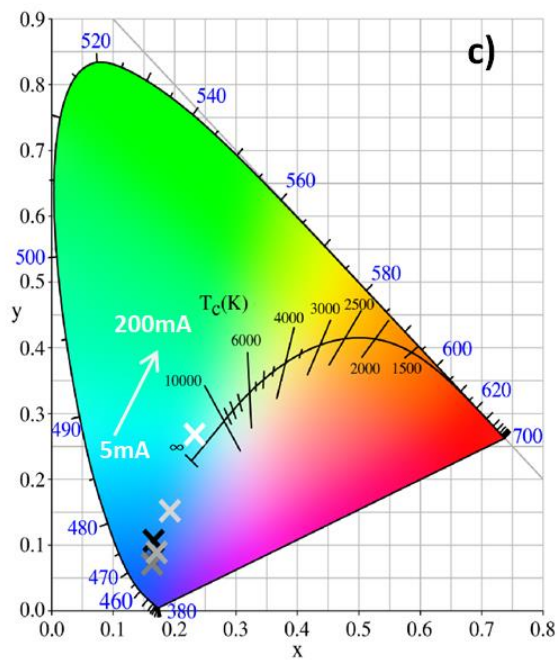
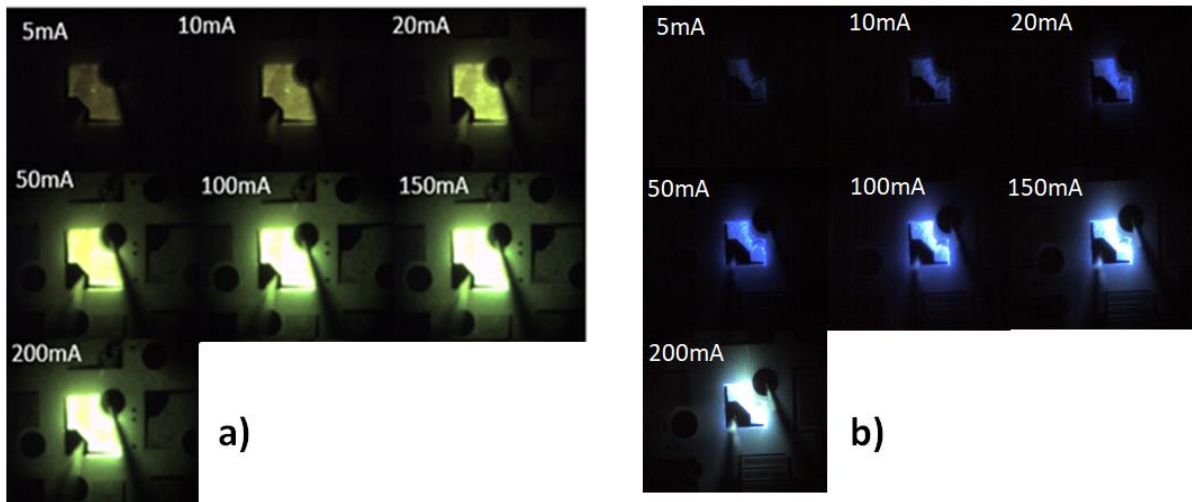


Figure 5.5 EL images at injection currents from 5mA to 200mA of (a) Sample A and (b) Sample B and (c) CIE x,y coordinates for Sample B as a function of current

5.5 Monolithically integrated white light LED on (11-22) semipolar GaN template for white light emission using down-converter approach

The second approach comprises a monolithically integrated white light LED by using an electrically injected semipolar (11-22) blue LED and an extra yellow InGaN MQWs as a down conversion layer epitaxially grown on the top of the blue LED, forming white emission. An InGaN/InGaN based LED is electrically injected, generating blue emission, where a portion of the emission is absorbed by the yellow InGaN MQWs on the top of the LED. In this approach the long wavelength QWs are grown after the growth of the blue LED in order to avoid high temperature during the growth of the growth of the blue LED. The reason is due to high temperature which may deteriorate the quality of the high indium content QWs. Previous studies have shown that the realization of white light would depend on the blue pumping wavelength and the absorption of the light converter^{16,17}. The absorption edge of (11-22) semipolar InGaN QWs emitting at ~534nm was found at around 470nm by photoluminescence excitation measurements performed by Zhang et al²². One of the advantages of down conversion approach is the fact that the high indium content yellow MQWs can be optically pumped without concerning any carrier distribution issue as discussed in Chapter 4. Under optical excitation, dual colour emissions have been observed. Although substantial work needs to be further carried out in terms of further design and further optimization in epitaxial growth, the idea has been proved.

5.6 Methods

The monolithic white LED structure was grown on an overgrowth semipolar (11-22) GaN template. The LED is consisted of 400nm un-doped GaN, a 1 μ m n-type GaN:Si layer, a InGaN/InGaN (4nm/9nm) SQW for blue emission, 150 nm p-type GaN:Mg and 3 InGaN/InGaN MQWs for yellow emission. Due to the specially design structure aiming at monolithic white LED, the fabrication steps should be modified. The initial step was the creation of a current path towards the blue p-n junction diode. A top-down selective etching was implemented by using micro-hole mask with \sim 4 μ m diameter for creating a micro-rod array pattern on the top of p-GaN layer. The etching procedure was employed by using ICP. The etching time was around \sim 40 seconds for achieving a shallow etching depth of approximately 60-80nm exposing the p-type layer. For this fabrication no passivation was used for the sidewalls of the micro-rods. Following the same fabrication for the standard LED, as discussed in Chapter 3, the dual-colour LED has been achieved. The following figure illustrates the fabrication steps of the LED.

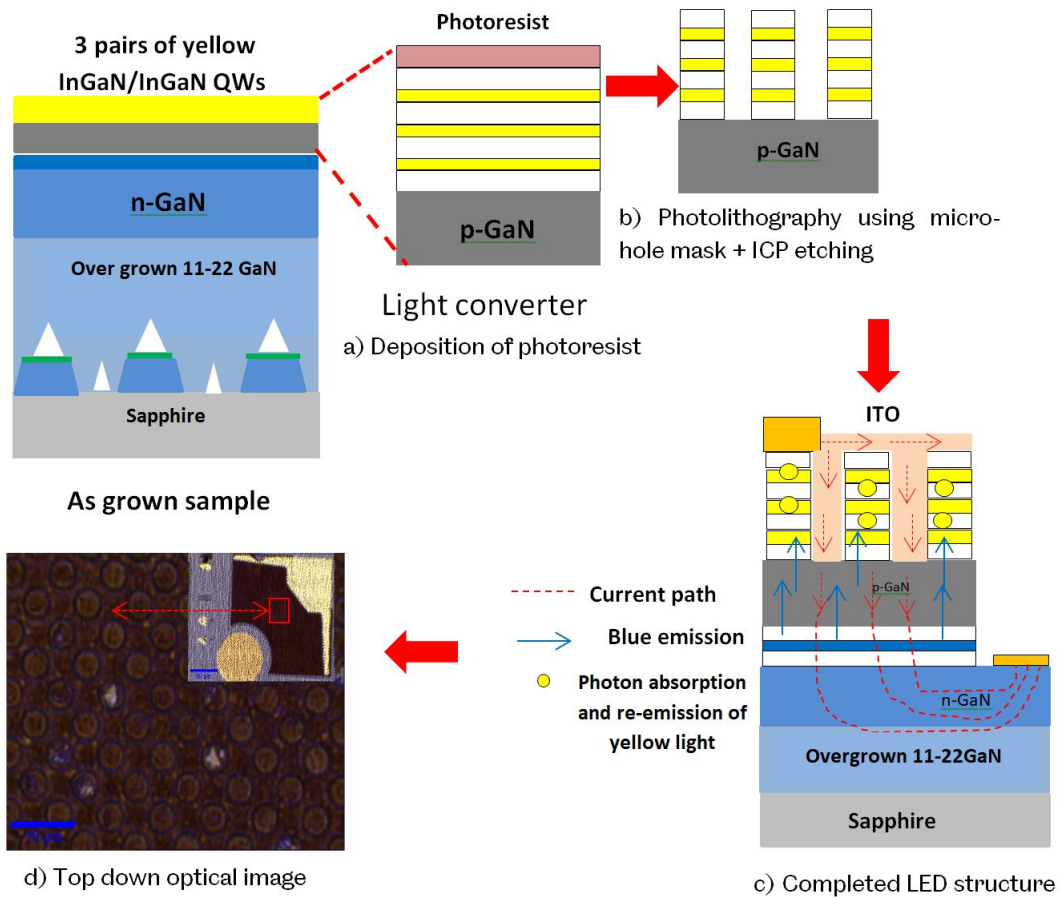


Figure 5.6 Schematic illustration of fabricating monolithically integrated LED with micro-rods array

5.7 Results and discussion:

5.7.1 P-type activation

After the step of the formation of micro-rods array the sample was subjected to post-annealing treatment to dissociate the hydrogen from the material and allow the magnesium to act as a p-type dopant. Post annealing temperature (in N₂ ambient) was kept at 675°C as before in order to avoid degradation of the high indium content layers. The duration time of annealing was 20 minutes. Figure 5.7 depicts IV characteristics of the LED. The LED exhibits high turn on voltage of 9.6V at 20mA injection current which can be attributed to inability to activate the regions under the microrods area because those region are covered with the light converter structure.

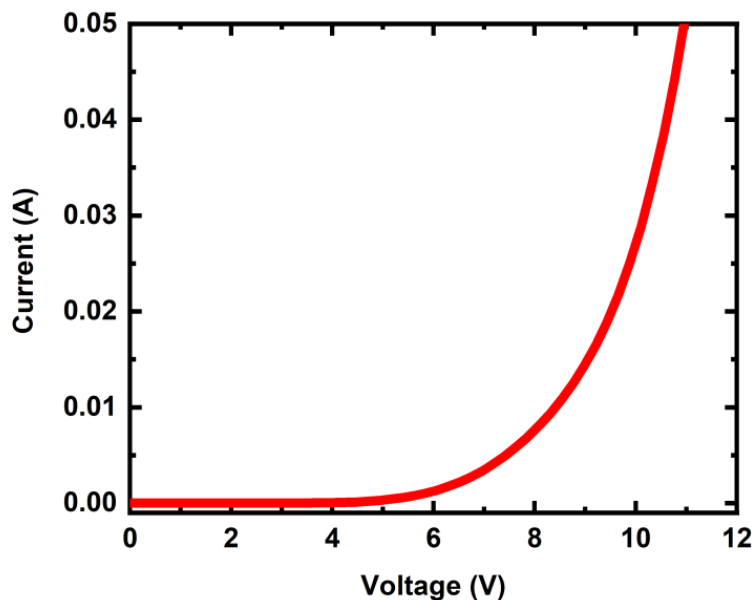


Figure 5. 7 I-V characteristics of the monolithically white light LED

5.7.2 Photoluminescence measurements

Photoluminescence measurements were initially conducted at room temperature on the as grown sample in order to confirm the emission wavelengths of the blue LED and the yellow MQWs. The sample exhibits strong emission at 534 nm coming from the three longer wavelength MQWs which act as a down conversion layer and a blue emission at 476nm, respectively.

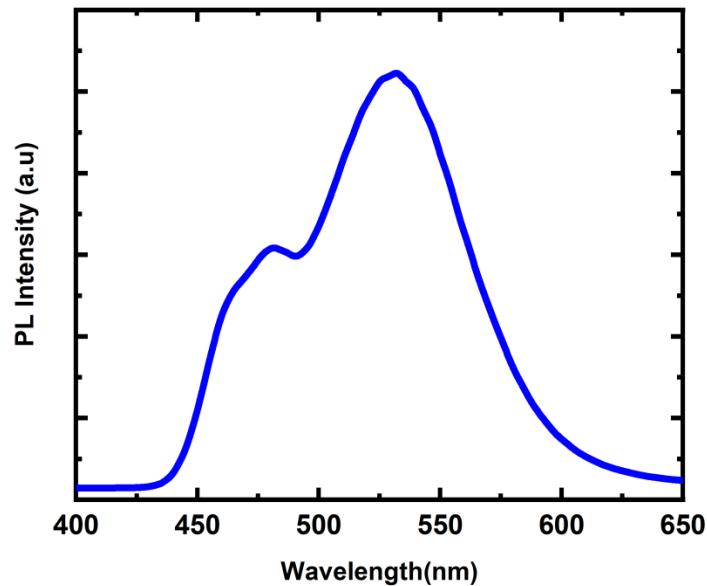


Figure 5.8 PL spectra of the as grown sample

5.7.3 Electroluminescence measurements

Electroluminescence measurements were performed on the fabricated LED under continuous wave conditions at room temperature. The LED was subjected to forward injection current at low current regime of 0.5mA to 1mA and higher current regime of 10mA up to 60mA. Figure 5.9 illustrates the electroluminescence as a function of injection current for the fabricated LED. At low excitation currents, the LED exhibits

dual-colour emissions center at 470 and 547nm respectively whereas at higher currents, the LED spectrum exhibits only the blue component with peak emission center at 471 nm and no indication of the long wavelength component for all injected current. The single peak in the blue region can be attributed to two possible reasons.

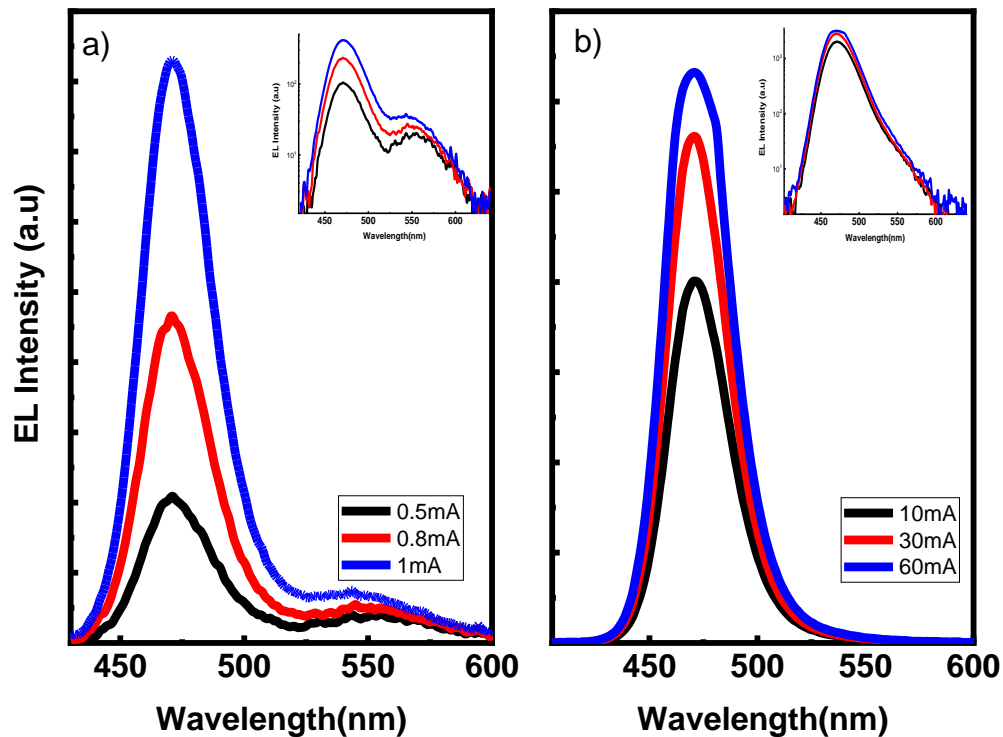


Figure 5.9 EL spectra under low and high injection currents the inset shows the spectra in log-plot

Since the long wavelength MQWs are optically pumped by the blue SQW, the intensity of the yellow MQWs strongly relies on their absorption at the peak emission wavelength of the blue SQW. It can be assumed that the yellow absorption profile may not agree with the blue emission at the high current regime where longer wavelength QWs exhibit a more pronounced blue shift. Thus, the light converter MQWs may absorb light in the rising edge of the blue emission spectrum indicating

that the absorption edge of the light converter MQWs lies on energy higher than the emission of the blue SQW. Another possible reason of the appearance of a single peak at high current may attribute to the low carrier density in the long wavelength MQWs,

Since the thickness of each QW of the light converter is small (4nm), the absorption from each QW is subsequently small, resulting to low carrier density in each QW. By increasing the thickness of the longer wavelength MQWs will result in a higher carrier density in each QW but it will significantly affect the emission wavelength. Thus, a potential solution for optimizing the LED structure requires increasing the number of QWs of the light converter whereas the blue and yellow emissions need to be further tuned in order to match the absorption profile of the light converter with the emission of the short wavelength QW.

5.8 Summary

In summary, dual-colour LEDs using two different approaches have been fabricated on (11-22) overgrown GaN. The first method refers one of the most direct methods of achieving white light emission which includes vertically oriented QWs emitting at different wavelength located in the active region. The particular structures with vertically oriented QWs were initially designed according to simulations performed in Chapter 4. Experimental results have successfully agreed with simulation outcomes. Specifically, it has been proven that the growth order of the long and short QWs is of paramount importance, while a thin GaN spacer needs to be grown prior to blue QW to effectively confined holes in the short wavelength QW. The second method is based on down conversion method which carrier transport issue is not a major issue

in the long wavelength QWs. The LED comprises a blue LED and yellow MQWs grown on top which act as a down conversion layer. Results showed that yellow and blue emissions wavelengths have to be further tuned in order to match the absorption profile of the longest wavelength QWs with the emission of the shortest wavelength QW. Furthermore, a greater number of the long wavelength QWs have to be grown in order to effectively absorb blue photons at higher current regime.

References

1. Hu, R., Luo, X., Feng, H. & Liu, S., Effect of phosphor settling on the optical performance of phosphor-converted white light-emitting diode. *J. Lumin.* **132**, 1252–1256 (2012).
2. Narukawa, Y., Ichikawa, M., Sanga, D., Sano, M. & Mukai, T., White light emitting diodes with super-high luminous efficacy. *J. Phys. D. Appl. Phys.* **43**, 354002 (2010).
3. Krames, M. R. *et al.*, Status and future of high-power light-emitting diodes for solid-state lighting. *IEEE/OSA J. Disp. Technol.* **3**, 160–175 (2007).
4. Tamura, T., Setomoto, T. & Taguchi, T., Illumination characteristics of lighting array using 10 candela-class white LEDs under AC 100 V operation. *J. Lumin.* **87**, 1180–1182 (2000).
5. Hwang, J.-H. *et al.*, Study on the effect of the relative position of the phosphor layer in the LED package on the high power LED lifetime. *Phys. status solidi* **7**, 2157–2161 (2010).
6. Huang, M. & Yang, L., Heat generation by the phosphor layer of high-power white LED emitters. *IEEE Photonics Technol. Lett.* **25**, 1317–1320 (2013).
7. Wang, T., Topical Review: Development of overgrown semi-polar GaN for high efficiency green/yellow emission. *Semicond. Sci. Technol.* **31**, 093003 (2016).
8. Ueda, M. *et al.*, Epitaxial growth and optical properties of semipolar (1122) GaN and InGaN/GaN quantum wells on GaN bulk substrates. *Appl. Phys. Lett.* **89**, 211907 (2006).

9. Damilano, B., Grandjean, N., Pernot, C. & Massies, J., Monolithic white light emitting diodes based on InGaN/GaN multiple-quantum wells. *Japanese Journal of Applied Physics, Part 2: Letters* **40**, L918 (2001).
10. Yamada, M., Narukawa, Y. & Mukai, T., Phosphor free high-luminous-efficiency white light-emitting diodes composed of InGaN multi-quantum well. *Japanese J. Appl. Physics, Part 2 Lett.* **41**, L246 (2002).
11. Huang, C. F., Lu, C. F., Tang, T. Y., Huang, J. J. & Yang, C. C., Phosphor-free white-light light-emitting diode of weakly carrier-density-dependent spectrum with prestrained growth of InGaN/GaN quantum wells. *Appl. Phys. Lett.* **90**, 151122 (2007).
12. Chen, C. H. *et al.*, Nitride-based cascade near white light-emitting diodes. *IEEE Photonics Technol. Lett.* **14**, 908–910 (2002).
13. Qi, Y. D., Liang, H., Tang, W., Lu, Z. D. & Lau, K. M., Dual wavelength InGaN/GaN multi-quantum well LEDs grown by metalorganic vapor phase epitaxy. in *Journal of Crystal Growth* **272**, 333–340 (North-Holland, 2004).
14. Lu, C. F. *et al.*, Phosphor-free monolithic white-light LED. *IEEE J. Sel. Top. Quantum Electron.* **15**, 1210–1217 (2009).
15. Park, I. K. *et al.*, Phosphor-free white light-emitting diode with laterally distributed multiple quantum wells. *Appl. Phys. Lett.* **92**, 091110 (2008).
16. Damilano, B. *et al.*, Blue-green and white color tuning of monolithic light emitting diodes. *J. Appl. Phys.* **108**, 073115 (2010).
17. Kowsz, S. J. *et al.*, Demonstration of phosphor-free polarized white light emission from monolithically integrated semipolar InGaN quantum wells. *Appl. Phys. Lett.* **107**, 101104 (2015).

18. Kowsz, S. J. *et al.*, Using band engineering to tailor the emission spectra of trichromatic semipolar InGaN light-emitting diodes for phosphor-free polarized white light emission. *J. Appl. Phys.* **120**, 033102 (2016).
19. Zhao, Y. *et al.*, Indium incorporation and emission properties of nonpolar and semipolar InGaN quantum wells. *Appl. Phys. Lett.* **100**, 201108 (2012).
20. Bai, J. *et al.*, (11-22) semipolar InGaN emitters from green to amber on overgrown GaN on micro-rod templates. *Appl. Phys. Lett.* **107**, 261103 (2015).
21. Martin, R. W. *et al.*, Light emission ranging from blue to red from a series of InGaN/GaN single quantum wells. *J. Phys. D. Appl. Phys.* **35**, 604–608 (2002).
22. Zhang, Y. *et al.*, Stokes shift in semi-polar (112̄2) InGaN/GaN multiple quantum wells. *Appl. Phys. Lett.* **108**, 031108 (2016).

Chapter 6

Optical polarization properties of (11-22) semi-polar InGaN LEDs with a wide spectral range

Semi-polar LEDs offer a unique feature of polarized light which c-plane counterparts' lack. This is due to the split of the two top-most valance sub-bands which lead to optical anisotropy and thus polarized light emission. A polarized light source plays an important role in many applications such as backlighting for screen displays. It is very important to understand the emission polarization mechanism for semipolar InGaN LEDs with different wavelengths operating under different injection current. In this chapter electroluminescence polarization measurements have been performed on a series of semi-polar InGaN light emitting diodes (LEDs) grown on semi-polar (11-22) templates. The emission wavelengths of these LEDs cover a wide spectral region from 443 to 555 nm. A systematic study has been carried out in order to investigate the influence of both indium content and injection current on polarization properties.

6.1 Introduction

III-nitride growth along a semi-polar or non-polar orientation is an effective approach in overcoming the aforementioned challenges in Chapter 1. Among a number of semi-polar orientations, the (11-22) direction has gained considerable attention in developing long wavelength LEDs due to an enhanced indium incorporation efficiency and reduced QCSE in the InGaN grown on the (11-22) GaN surface^{1,2,3}. Furthermore, semi-polar or non-polar LEDs offer a unique feature that their polar c-plane counterparts lack, which is an intrinsic optical polarized emission. This is owed to their low crystal symmetry, where the inhomogeneous biaxial strain of a semi- or non-polar plane results in the splitting of the uppermost valence bands leading to optical anisotropy and thus polarized emission. A polarized light source plays a vital role in many applications, such as backlighting. The current approach to LED backlighting utilizes a polarization filter to reject unpolarized light. Different techniques for polarizing backlighting system have been employed for improving optical losses; such as backlight recycling where the light that does not pass through a polarizer filter is recycled by reflection. These techniques still exhibit ~30 % optical power loss^{4,5}. Therefore, it is necessary to develop a cost-effective approach for the usage of semi-polar or non-polar LEDs which exhibit intrinsic polarization light.

However, two main challenges in developing high-performance semi-polar LEDs need to be overcome. The first is to obtain high-quality semi-polar GaN on industry compatible substrates, such as sapphire. Recently, our team have demonstrated semi-polar InGaN LEDs overgrown on our (11-22) semi-polar GaN templates with significantly improved crystalline quality, leading to high performance semi-polar

InGaN LEDs across a wide spectral range, up to amber^{6,7,8}. Secondly, it is crucial to fully understand the polarization mechanisms of different wavelength semi-polar (11-22) InGaN LEDs operating under a range of different injection currents. Although there have been a number of reports in this field^{9,10,11}, so far these mechanisms are still not well-understood, consequently leading to controversial debates.

It has previously been observed that InGaN/GaN LEDs grown on semi-polar (11-22) bulk substrates operating in the blue, green and amber spectral region do not exhibit any enhancement in polarization degree with increasing indium composition¹², while a monotonic increase in the absolute value of polarization degree has conversely been reported in semi-polar (11-22) InGaN/GaN LEDs with similar rising indium content¹³. The observable polarization switching phenomena has been attributed to that two distinct top valence subbands approach each other with increasing indium content, eventually leading to a crossover of these at ~30 % indium content¹⁴. Optical polarization degree exhibits a positive sign before the switching point and negative sign after the switching point. However, there still exist some debates surrounding the formation of this mechanism. On the one hand, polarization switching could be caused by large InN deformation potentials, while other studies have concluded that it is due to partial strain relaxation or inhomogeneous strain effects across the (11-22) InGaN quantum wells^{15,16}. It has also been reported that a change in polarization degree has been observed when a relaxed underlying InGaN buffer layer is employed prior to the growth of an emitting InGaN quantum well structure, where underlying InGaN buffer layers with different thickness and indium content have been considered^{17,18}. Furthermore, a combination of the self-consistent Poisson and 6×6 $k \cdot p$ Schrödinger equations has been used to predict the influence of polarization

properties as a function of injection current in (11-22) semi-polar LEDs¹⁹. However, there are no experimental data to support these predictions.

In this work, a systematic study has been conducted on a series of semi-polar InGaN LEDs with a wide range of indium content (covering emission wavelengths from 443 to 555 nm) grown on (11-22) semi-polar GaN templates with a high crystalline quality. Emission polarization has been investigated as a function of both indium content and injection current.

6.2 Methods

6.2.1 Epitaxial growth

All the semi-polar LEDs were grown on high quality (11-22) semi-polar GaN templates on m-plane sapphire by a low-pressure metal-organic vapour phase epitaxy (MOVPE) system. The semi-polar (11-22) GaN templates were obtained by using our well-established overgrowth approach on micro-rod arrays, where the micro-rod diameter is typically 4 μm ^{6,7,8}. For the micro-rod array fabrication, a SiO₂ layer with a thickness of 500 nm was initially deposited on a standard single semi-polar (11-22) GaN layer with a thickness of ~400 nm grown on m-plane sapphire. Subsequently a standard photolithography patterning technique and then dry-etching processes were employed to etch the SiO₂ film into regularly arrayed micro-rods with a diameter of 4 μm , which serve as a secondary mask to etch GaN underneath, forming regularly arrayed GaN micro-rods. Finally, the regularly arrayed semi-polar GaN micro-rods were reloaded into the MOVPE chamber for overgrowth. The overgrown semi-polar (11-22) GaN layer with a thickness of ~4 μm exhibits a typical dislocation

density of $2 \times 10^8 \text{ cm}^{-2}$ and a typical basal stacking fault density of $4 \times 10^4 \text{ cm}^{-1}$ ^{6,7,8}. Figure 6.1a depicts a TEM image which demonstrates the significant reduction of defects in the overgrown GaN in comparison with the GaN micro-rods. The significant reduction of defects is attributed to the SiO₂ blocking and coalescence process during the overgrowth. Figure 6.1b illustrates a typical plane-view TEM of our (11-22) LED structure demonstrating the dislocation distribution across the surface. More details regarding the crystal quality can be found elsewhere, which include x-ray measurements and transmission electron microscopy (TEM) measurements, please refer to Refs.⁶⁻⁸.

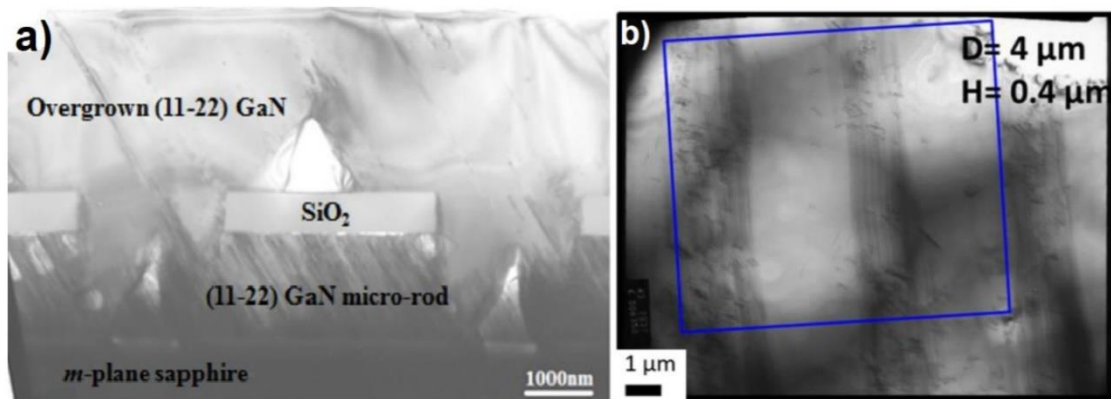


Figure 6.1 Typical cross-sectional TEM image of our (11-22) LED overgrown on a micro-rod arrayed template (a) and Typical plane-view TEM image of our (11-22) LED structure, showing that the dislocation density is $2.0 \times 10^8 / \text{cm}^2$ ^{6,7,8}.

All the LED structures were further grown on the semi-polar overgrown templates, beginning with a 1 μm Si-doped n-type GaN layer, then a 4 nm single InGaN quantum well sandwiched between two 9 nm thick un-doped GaN barriers and a final 150 nm p-type GaN capping layer. The only difference in the growth of these LEDs is due to the growth temperature for the InGaN SQW in order to tune indium content,

allowing for the emission wavelengths ranging from 443 to 555 nm (indium content from 0.15 to 0.3 for each case).

6.2.2 Device Fabrication

By means of a standard photolithography technique and subsequent dry-etching processes, LEDs with a standard mesa size of $330 \times 330 \mu\text{m}^2$ have been fabricated. 100 nm ITO was used as transparent p-type contact, while an n-type Ti/Al/Ti/Au alloy contact was deposited on to n-type GaN. Finally, Ti/Au alloy bond-pad are deposited by thermal evaporation to form both p-type and n-type contact electrodes. Figure 6.2 illustrates a schematic of the semi-polar InGaN LEDs.

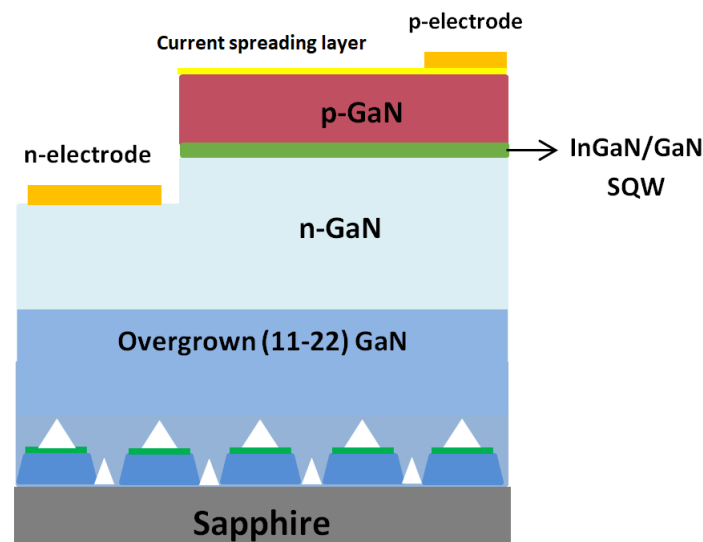


Figure 6.2 Schematic of semi-polar (11-22) InGaN LEDs

6.3 Results and Discussion

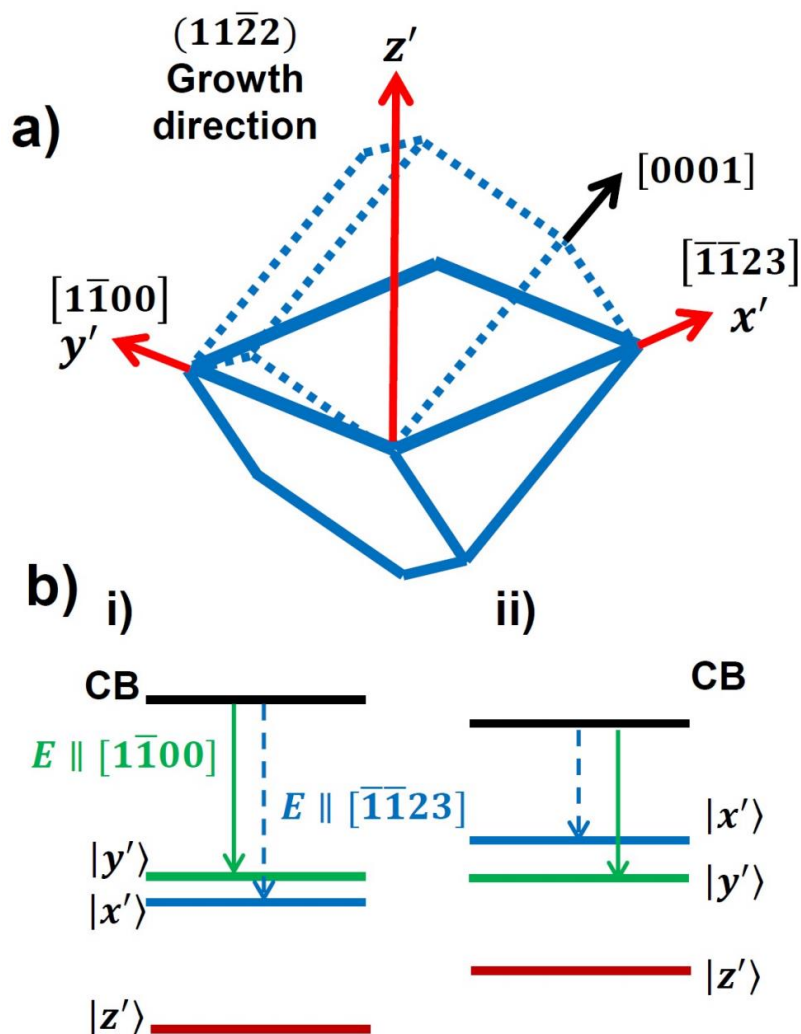


Figure 6.3 Schematics of (a) semi-polar (11-22) GaN crystal plane and (b) band diagram before and after polarization switching.

Figure 6.3a schematically illustrates a primed coordinate system showing that the x' - y' plane represents the (11-22) GaN plane, where the two existing orthogonal directions are labelled by x' and y' . x' represents the $[-1-123]$ direction that is parallel to the projection of the c-axis ($\parallel c'$), where y' shows $[1-100]$ direction perpendicular to this c-axis ($\perp c$), and z' represents the growth direction. Owing to

the anisotropic strain, the valence subbands of the (11-22) GaN split into $|y'\rangle$ and $|x'\rangle$, where $|y'\rangle$ and $|x'\rangle$, are the first and the second valence subbands, associated with the respective emission from dipoles along the $[1-100]$ and $[-1-123]$ directions. However, with increasing indium content, these two otherwise separated valence subbands approach each other and eventually exchange positions. As a result, the highest valence subband becomes $|x'\rangle$ with a dipole which is parallel to $[-1-123]$, while the second valence subband becomes $|y'\rangle$ with a dipole parallel to $[1-100]$. Figure 6.3b provides a schematic illustration depicting the change before (i) and after (ii) polarization switching.

A polarization degree, denoted ρ , is defined by the ratio of the integrated polarized emission intensities along one direction relative to another direction as expressed below:

$$\rho = \frac{I_{[1\bar{1}00]} - I_{[\bar{1}\bar{1}23]}}{I_{[1\bar{1}00]} + I_{[\bar{1}\bar{1}23]}} \quad (6.1)$$

A positive polarization ratio ($\rho > 0$) means that the dominant emission component is polarized along the $[1-100]$ direction, while a negative polarization ($\rho < 0$) demonstrates that the dominant polarization component is along the $[-1-123]$ direction.

Electroluminescence (EL) measurements have been carried out at room temperature in a continuous wave (cw) mode. Polarization dependent EL measurements have been conducted by using an electroluminescent system described in Chapter 3. There is a rotating linear polarizer placed between an objective lens and spectrometer, which allows polarization dependent EL

measurements to be conducted between the two orthogonal directions, namely [1-100] and [-1-123]. The 0° and 90° of the polarizer position correspond to the electric fields aligned along [1-100] and [-1-123] directions, respectively. In order to remove the system's polarization response a non-polarised light source such as a halogen lamp was used, allowing the measurement of the overall polarization degree of the system. As a confirmation, c-plane LED polarization measurements were performed. The measured system's polarization response was then removed from the c-plane LED, resulting in a non-polarized emission as it is expected for the specific orientation.

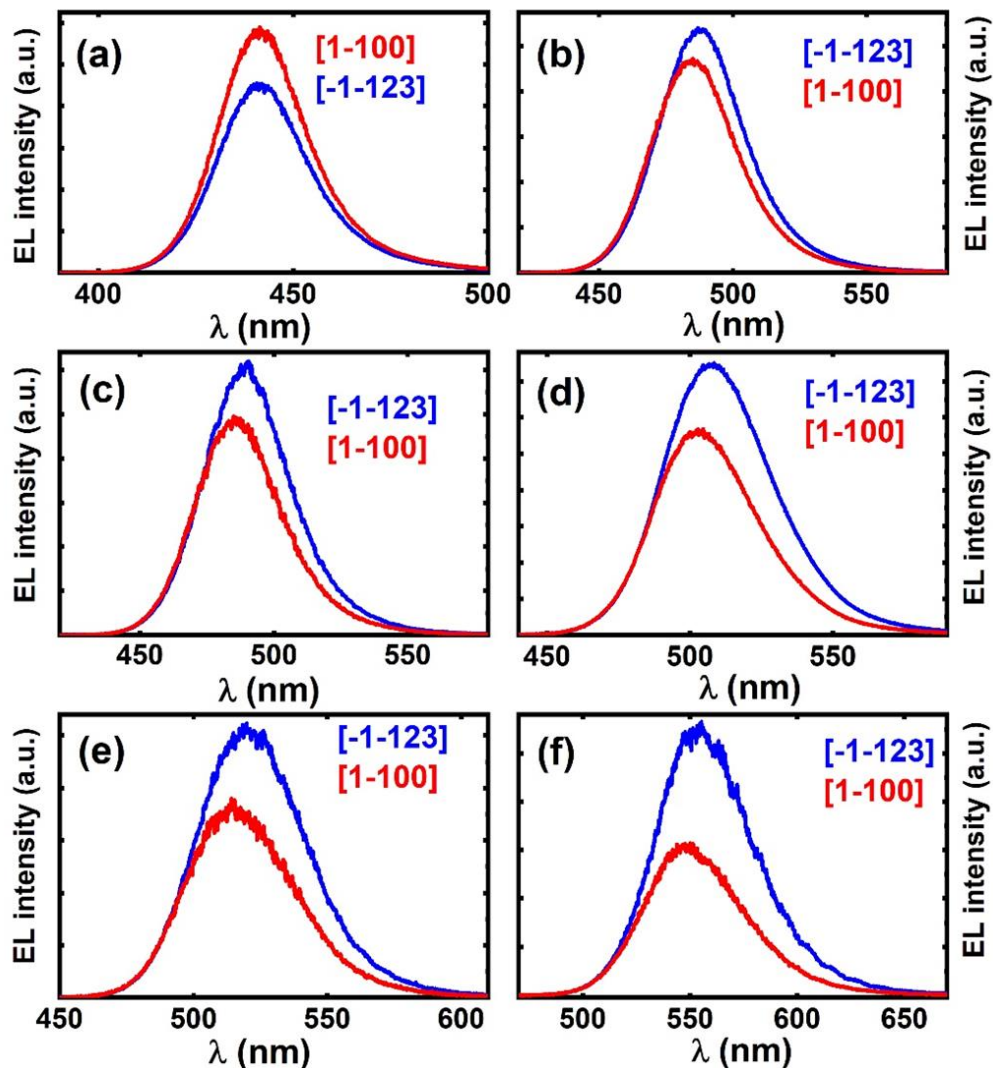


Figure 6.4 Polarized EL spectra measured at 20 mA injection current for the semi-polar (11-22) LEDs with increasing indium content and peak emission wavelength. In each case, the EL spectrum labeled in red was measured at a polarizer angle of 0° corresponding to the electric field aligned along [1-100], while the EL spectrum in blue was measured at a polarizer angle of 90° corresponding to the electric field aligned along [-1-123].

Figure 6.4 shows the EL spectra of each semi-polar InGaN LEDs with a peak emission wavelength ranging from blue (443 nm) to yellow (555 nm), which are measured with the polarizer aligned at 0° and 90° under 20mA injection current. In each case, the EL spectrum colored with a red-line was measured with the polarizer at a 0° angle, corresponding to the electric field along [1-100] direction, while the EL spectrum labelled with a blue-line was measured at a 90° polarizer angle, indicating the electric field aligned to the [-1-123] direction. This demonstrates that the polarized EL spectra depend on the peak emission wavelength and therefore indium content.

Figure 6.5a shows the polarization degrees of all the semi-polar LEDs as a function of peak emission wavelength, where the polarization degree has been extracted from Figure 6.4 using Equation 6.1.

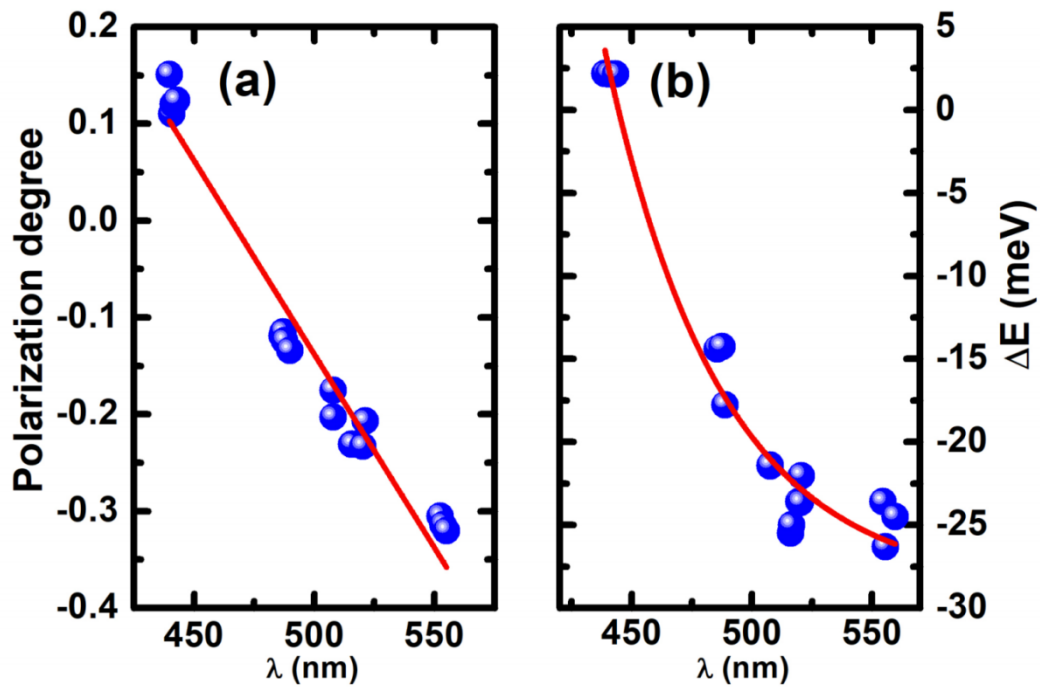


Figure 6.5 (a) Polarization degree as a function of peak emission wavelength; and (b) Energy separation ΔE of the two polarized emissions as a function of peak emission wavelength. Solid lines are a guide to the eye

Figure 6.5a shows a polarization degree ranging from 0.15 for the shortest wavelength emitter (443 nm LED) to -0.33 for the longest wavelength LED (555 nm LED). The polarization degree of the 443 nm blue LED, exhibits a positive sign ($\rho > 0$), meaning that the intensity of the emission with the electric field polarized along the [1-100] direction is higher than that of the emission with the electric field polarized along the [-1-123] direction. Figure 6.5a also demonstrates that the polarization degree approaches zero at ~ 470 nm. For the longer wavelength LEDs above ~ 470 nm the polarization degree therefore switches to a negative sign ($\rho < 0$) which signifies that the intensity of the polarized emission along the [-1-123] direction is now higher than that of the polarized emission along the [1-100] direction. This is entirely consistent with previous studies^{14,20,21}. As the emission moves towards longer

wavelength, the polarization degree becomes larger in the negative direction owing to the larger energy separation of the two topmost $|x'\rangle$ and $|y'\rangle$ valence subbands.

Figure 6.5b depicts the energy separation between the two polarized emissions (along $[-1-123]$ and $[1-100]$ directions) for each LED as a function of peak emission wavelength. The energy separation labelled as Δ_E can be defined as:

$$\Delta_E = E_{P_{[-1-123]}} - E_{P_{[1-100]}} \quad (6.2)$$

where $E_{P_{[1-100]}}$ and $E_{P_{[-1-123]}}$ correspond to the peak energies of their emission with the electric field polarized along the $[1-100]$ and $[-1-123]$ directions, respectively.

Figure 6.5b shows that the Δ_E between the two polarized emissions of the 443 nm blue LED is positive. As the emission wavelength increases, the Δ_E becomes negative and continues to further reduce with wavelength meaning that the absolute value of Δ_E further increases. A comparison between Figure 6.5a and 6.5b depicts that a negative polarization degree ($\rho < 0$) is always connected with a negative valued energy separation ($\Delta_E < 0$), which is in agreement with another report¹⁴. This is due to the transitional probability between the topmost valence subband and the conduction band being higher than that between the second topmost valence subband and the conduction band.

Figure 6.6a depicts the polarization degrees of all the LEDs measured as a function of injection current from 5 to 100 mA, while Figure 6.6b shows the Δ_E between the two polarized emissions (along the $[-1-123]$ and the $[1-100]$ directions) also as a function of injection current in the same range.

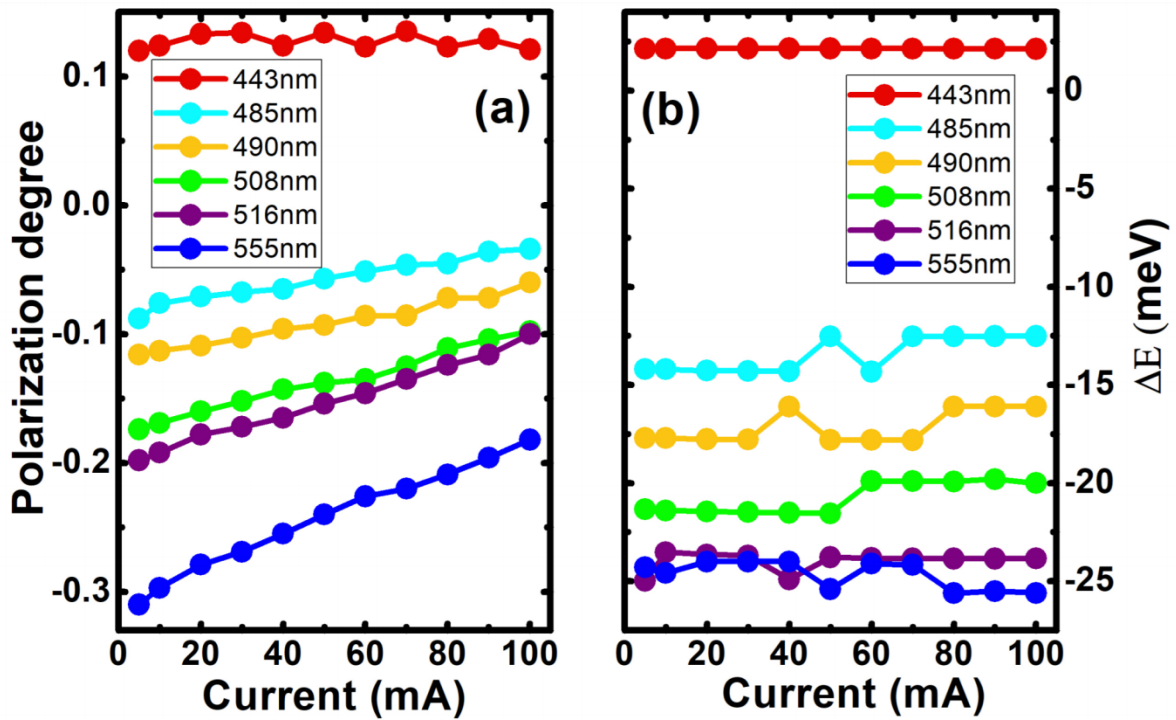


Figure 6.6 (a) Polarization degree as a function of injection current; and (b) Energy separation Δ_E as a function of injection current of each of the semi-polar LEDs.

It is noted that the 443 nm LED exhibits a different relationship to polarization degree (ρ) and Δ_E with injection current in comparison to the longer emission wavelength LEDs. The longer wavelength LEDs with a negative polarization degree ($\rho < 0$) demonstrate that an absolute value of polarization degree ($|\rho|$) decreases with increasing injection current, while both the polarization degree and the Δ_E of the 443 nm blue LED remain almost constant regardless of injection current. Furthermore, for each of the longer wavelength LEDs, the change in polarisation degree decreases with increasing injection current in each case. In addition, this change in polarisation degree also increases with increasing indium content (emission wavelength). In greater detail, the change in polarization degree from 5 to 100 mA is approximately 0.06, 0.1 and 0.14 for each of the 485, 508 and 555 nm LEDs, respectively. Figure 6.7

shows the change in polarization degree as a function of emission wavelength, exhibiting that it increases with increasing emission wavelength.

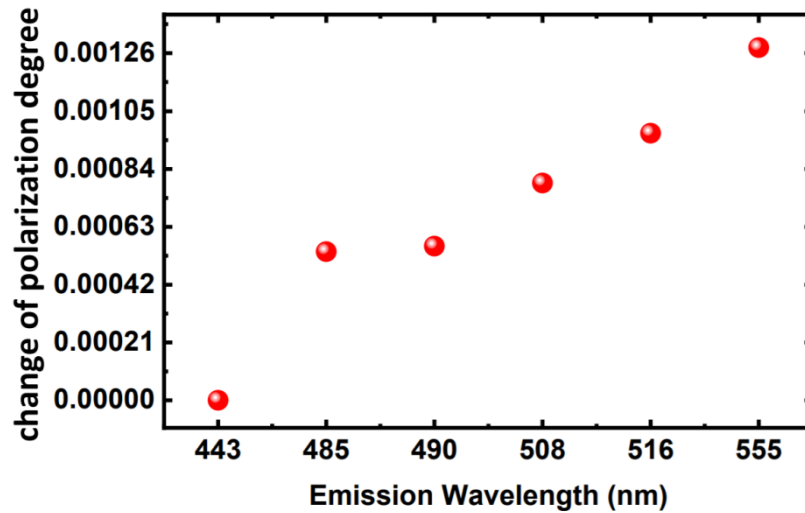


Figure 6.7 Change of polarization as a function of emission wavelength

The reduction in the absolute value of polarization degree with increasing injection current can be attributed to band filling effects. In the longer wavelength LEDs, the topmost valence subband is $|x'\rangle$ with a resulting dominant emission component polarized along the $[-1-123]$ direction, while an emission associated with the second valence subband $|y'\rangle$ is polarized along the $[1-100]$ direction. At low injection current, holes mainly occupy the first valence subband $|x'\rangle$. With increasing injection current holes then begin to fill the second valence subband $|y'\rangle$ states, once the more favorable states of first subband are fully occupied. Consequently, the $|y'\rangle$ valence subband related emission increases with increasing injection current, and therefore the overall polarization degree decreases.

However, the blue 443 nm LED demonstrates a polarization degree that remains nearly constant with increasing injection current, which is similar to an existing

report²². This effect is attributed to the significantly higher density of states (DOS) associated with the $|y'\rangle$ subband (polarized emission along [1-100]) than is associated with the $|x'\rangle$ subband (polarized emission along [-1-123])²⁰. Consequently, the $|y'\rangle$ subband can accommodate a significantly high density of holes, leading to a lower probability for holes to occupy the $|x'\rangle$ subband before polarization switching. This naturally means that the polarization degree remains unchanged with increasing injection current.

In principle, the Δ_E is determined mainly by the difference in energy state between the $|y'\rangle$ and $|x'\rangle$ subbands, and thus is not sensitive to injection current. Consequently, as shown in Figure 6.6b, the Δ_E remains almost unchanged with increasing injection current.

6.4 Summary

In conclusion, a systematic study of the influence of both indium content and injection current on polarization properties has been performed on a series of semi-polar LEDs with a wide spectral range between 443 to 555 nm all grown on (11-22) semi-polar GaN templates with high crystal quality. Detailed polarization dependent EL measurements demonstrate that the polarization degree strongly depends on the LED emission wavelength, which varies from a positive polarization degree of 0.15 at the shortest wavelength (443 nm) to a negative polarization degree of -0.33 for the longest wavelength LED. A linear fitting indicates that a polarization switching takes place at around 470 nm. Furthermore, the longer wavelength LEDs with a negative polarization degree exhibit a consistent relationship between the polarization degree

and injection current, while the 443 nm blue LED (before polarization switching) exhibits an insensitivity in polarization degree to injection current.

References

1. Strittmatter, A. et al., Semi-polar nitride surfaces and heterostructures, *Phys. Status Solidi (b)* **248**, 561–573 (2011).
2. Zhao, Y. et al., Indium incorporation and emission properties of nonpolar and semipolar InGaN quantum wells, *Appl. Phys. Lett.* **100**, 201108 (2012).
3. Wang, T., Topical Review: Development of overgrown semi-polar GaN for high efficiency green/yellow emission. *Semicond. Sci. Technol.* **31**, 093003 (2016).
4. Li, Y., Wu, S. T. & Wu, T. X., Design Optimization of Reflective Polarizers for LCD Backlight Recycling. *IEEE/OSA J. Disp. Technol.* **5**, 335–340 (2009).
5. Pang, Z. & Li, L., Novel High Efficiency Polarizing Backlighting System with a Polarizing Beam Splitter. *SID Symp. Dig. Tech. Pap.* **30**, 916 (1999).
6. Zhang, Y. et al., Microstructure investigation of semi-polar (11-22) GaN overgrown on differently designed micro-rod array templates, *Appl. Phys. Lett.* **109**, 241906 (2016).
7. Zhang, Y. et al., Defect reduction in overgrown semi-polar (11-22) GaN on a regularly arrayed micro-rod array template, *AIP Advances* **6**, 025201 (2016).
8. Bai, J. et al., (11-22) semipolar InGaN emitters from green to amber on overgrown GaN on micro-rod templates, *Appl. Phys. Lett.* **107**, 261103 (2015).
9. Yamaguchi, A. A. & Kojima, K., A simple theoretical approach to analyze polarization properties in semipolar and nonpolar InGaN quantum wells, *Appl. Phys. Lett.* **98**, 10–13 (2011).
10. Kojima, K., Kamon, H., Funato, M. & Kawakami, Y., Theoretical investigations on anisotropic optical properties in semipolar and nonpolar InGaN quantum wells, *Phys. Status Solidi (c)* **5**, 3038–3041 (2008).

11. Schade, L. et al., On the optical polarization properties of semipolar InGaN quantum wells, *Appl. Phys. Lett.* **99**, 97–100 (2011).
12. Funato, M., et al. Blue, green, and amber InGaN/GaN light-emitting diodes on semipolar {1122} GaN bulk substrates, *Jpn. J. Appl. Phys.* **450**, L659 (2006).
13. Fellows, N., et al. Increased polarization ratio on semipolar (1122) InGaN/GaN light-emitting diodes with increasing indium composition, *Jpn. J. Appl. Phys.* **47**, 7854 (2008).
14. Ueda, M. et al., Polarization switching phenomena in semipolar $\text{In}_x\text{Ga}_{1-x}\text{N}/\text{GaN}$ quantum well active layers, *Phys. Rev. B* **78**, 233303 (2008).
15. Yan, Q., Rinke, P., Scheffler, M. & Van De Walle, C. G., Role of strain in polarization switching in semipolar InGaN/GaN quantum wells, *Appl. Phys. Lett.* **97**, 10–13 (2010).
16. Roberts, C., Yan, Q., Miao, M. S. & Van De Walle, C. G., Confinement effects on valence-subband character and polarization anisotropy in (1122) semipolar InGaN/GaN quantum wells, *J. Appl. Phys.* **111**, 073113 (2012).
17. Park, S.-H. et al., Polarization characteristics of semipolar (1122) InGaN/GaN quantum well structures grown on relaxed InGaN buffer layers and comparison with experiment, *Opt. Express* **22**, 14850 (2014).
18. Okada, N., Okamura, Y., Uchida, K. & Tadatomo, K., Controlling optical polarization of {11-22} semipolar multiple quantum wells using relaxed underlying InGaN buffer layers, *Opt. Mater.* **58**, 243–247 (2016).
19. Huang, H. H. & Wu, Y. R., Light emission polarization properties of semipolar InGaN/GaN quantum well, *J. Appl. Phys.* **107**, 053112 (2010).

20. Masui, H. et al., Correlation between optical polarization and luminescence morphology of (1122)-oriented InGaN/GaN quantum-well structures, *Appl. Phys. Express* **2**, 2–4 (2009).
21. Sakai, S. & Yamaguchi, A. A., Theoretical analysis of optical polarization properties in semipolar and nonpolar InGaN quantum wells for precise determination of valence-band parameters in InGaN alloy material, *Phys. Status Solidi (b)* **252**, 885–889 (2015).
22. Kim, D. S. et al., Highly stable blue-emission in semipolar (11-22) InGaN/GaN multi-quantum well light-emitting diode, *Appl. Phys. Lett.* **103**, 021111 (2013).

Chapter 7

Conclusions and future work

7.1 Summary of results

7.1.1 Carrier transport in multi-colour (11-22) semi-polar LEDs

By means of performing one-dimensional drift-diffusion simulations carrier transport phenomena were examined in semi-polar LEDs with multi-colour emission. In order to examine the effects of crystal orientation on carrier transport, two initial LED structures with identical emissions have been compared in polar (0001) orientation and semi-polar (11-22) orientation. By taking advantage of utilizing semi-polar LEDs, a structure named Sample B was designed to emit dual colour-emission where a thin GaN spacer has been introduced prior to the growth of the blue QW. The growth order of the QWs was also examined, demonstrating that a dual colour emission can be achieved by growing first the longer wavelength QWs and then the shortest QW. Finally, factors such as indium composition of the QWs and barrier thickness were examined in terms of balancing the hole distribution across the active region. A tri-chromatic LED has been achieved by effectively tuning the barrier thicknesses and indium composition of the QWs.

7.1.2 Fabrication of monolithically integrated white light LEDs on (11-22) semi-polar GaN templates

Monolithically integrated white light LEDs have been fabricated on (11-22) semipolar GaN templates by using two different approaches. In order to validate our considerations from the simulation outcomes, Sample A and Sample B were grown on our high quality semi-polar overgrown templates. Experimental results have agreed well with simulations outcomes, demonstrating that the growth order of QWs and the growth of a thin GaN spacer are of vital importance for achieving a dual-colour LED.

The second approach utilizes a down-conversion method, where yellow MQWs, are grown on the top of a blue LED consisting of SQW in order to serve as light converter. In such configuration carrier transport effects are no concern because carriers are optically excited in the yellow MQWs. Results showed a dual emission peak at low current excitation and a single emission peak at higher excitation current, thus further optimization is required.

7.1.3 Optical polarization properties of (11-22) semi-polar InGaN LEDs with a wide spectral range

Electroluminescence polarization measurements have been conducted on a series of (11-22) semi-polar InGaN LEDs with a wide range of indium content covering emission wavelengths from 443 to 555 nm. It can be concluded that the optical polarization properties are strongly depended on both the LED emission wavelength (indium content) and the injection current.

7.2 Future work

Based on simulations performed in Chapter 4 dual-colour emission LEDs were initially grown on our high quality semipolar overgrown templates validating our initial assumptions. By optimizing both indium content and barrier thicknesses a new structure with three distinct peaks has been designed, demonstrating even distribution of holes across the entire active region. Further work is required, including the growth of this new structure for achieving a three colour emission and further optimization for achieving high quality white LED with high CRI.

Furthermore, the monolithically integrated white LED with down conversion presented in Chapter 5 needs further optimization in terms of improving turn on voltage and also achieving a dual-colour emission with relative intensities for white colour emission at higher injection current. The current approach exhibits high turn on voltage due to inability of activating some portions of the p-GaN layer, in particular the areas under the micro-rods. Thus a different formation of electrical path needs to be implemented. The formation of the current path should utilize either stripes or rods with lower dimensions, allowing a greater area of p-GaN to be activated. In addition both blue and yellow emissions need to be further tuned in order to match the absorption profile of the light converter with the emission of the blue LED whereas a greater number of yellow QWs need to be grown in order to enhance the absorption of the light converter, Photoluminescence excitation measurements needs to be conducted in order to identify the absorption profile of the light converter so as to be effectively tuned with the emission of the blue QW. For the efficiency of the device, different samples which include only the light converter and

the blue QW and need to be grown. Quantum efficiency measurements will then have to be contacted,

One of the major challenges to overcome is the efficiency droop, which current LEDs suffer at high current excitations. A laser diode provides a potential solution to efficiency droop, as it offers higher efficiencies at high injection current than LEDs¹⁻³. Multi-colour lasers or white light laser have gained much interest in recent years^{1,2,4-6}. For longer wavelength LDs and subsequently for white light emission (11-22) semipolar is one of the most promising solutions as aforementioned. For a vertically stacked MQWs carrier transport is one of the main-challenges to overcome. In a laser diode with vertically stacked QWs, where high current injection is needed the situation becomes more complicated. A white light laser diode grown on (20-2-1) has been reported⁷. This particular orientation does not favor indium incorporation content and is not ideal for longer wavelength. Therefore a systematic study on carrier transport in multi-colour laser diode structure grown on (11-22) semi-polar needs be conducted. Another challenge of white light laser diode is to achieve high colour rendering index CRI. This required to effectively balancing the spectral distribution and ratios of a multicolor emission. Furthermore another challenge on a laser diode structure is the high threshold current which needs to be taken into account when designing the active region of a laser diode.

References

1. Denault, K. A., Cantore, M., Nakamura, S., Denbaars, S. P. & Seshadri, R. Efficient and stable laser-driven white lighting. *AIP Adv.* **3**, 72107 (2013).
2. Wierer, J. J., Tsao, J. Y. & Sizov, D. S. The potential of III-nitride laser diodes for solid-state lighting. *Phys. status solidi* **11**, 674–677 (2014).
3. Wierer, J. J., Tsao, J. Y. & Sizov, D. S. Comparison between blue lasers and light-emitting diodes for future solid-state lighting. *Laser Photon. Rev.* **7**, 963–993 (2013).
4. Fan, F., Turkdogan, S., Liu, Z., Shelhammer, D. & Ning, C. Z. A monolithic white laser. *Nat. Nanotechnol.* **10**, 796–803 (2015).
5. Ryu, H.-Y. & Kim, D.-H. High-brightness Phosphor-conversion White Light Source Using InGaN Blue Laser Diode. *J. Opt. Soc. Korea* **14**, 415–419 (2010).
6. Xu, Y. *et al.* White light emission from ultraviolet laser diode. *Laser Phys.* **19**, 403–406 (2009).
7. Lee, C. *et al.* Semipolar GaN-based laser diodes for Gbit/s white lighting communication: devices to systems. in Gallium Nitride Materials and Devices XIII (eds. Chyi, J.-I., Morkoç, H. & Fujioka, H.) 10532, 84 (SPIE-Intl Soc Optical Eng, 2018).